

---

# Masses of Small Bodies:

Mass estimation of small solar system bodies  
using Radio Science data from close flybys

---

I N A U G U R A L – D I S S E R T A T I O N  
ZUR  
ERLANGUNG DES DOKTORGRADES  
DER MATHEMATISCH–NATURWISSENSCHAFTLICHEN FAKULTÄT  
DER UNIVERSITÄT ZU KÖLN

VORGELEGT VON  
THOMAS PAUL ANDERT

AUS LICHTENFELS

KÖLN, JANUAR 2010

Berichterstatter: P. D. Dr. M. Pätzold  
Prof. Dr. J. Saur  
Prof. Dr. B. Häusler

Tag der mündlichen Prüfung: 12.01.2010

---

## Abstract

The Radio Science technique enables to estimate the mass and other gravitational parameters of a solar system body from spacecraft observations very precisely. It uses the radio link between ground station and spacecraft. The frequency shift of the radio signal is proportional to the relative velocity change between spacecraft and ground station. If a spacecraft performs a close flyby at a solar system body, the velocity of the spacecraft is changed by the gravitational attraction of the body. If all other contributions on the radio signal are known, the remaining frequency change is solely due to the gravitational attraction. A least square fit can be performed on the frequency residuals to derive from it gravitational parameters.

Within this thesis models were developed and merged into a software package with which it is possible to determine the orbit of a spacecraft precisely and to predict accurately the frequency to be observed at a ground station. Models for extracting the frequency shift caused by the propagation of the radio signal through the ionosphere and troposphere of the Earth were incorporated. The accuracy of the predicted frequency, i.e. the difference between measurement and predict, is in the same order as the total Doppler velocity error in X-band from the thermal noise of the ground station and the transponder phase noise.

Filtering techniques were established improving the signal to noise ratio at least by a factor of three. A numerical stable least square fitting procedure was introduced to fit the frequency change due to the gravitational attraction of a body onto the measured frequency residuals.

Measurements from the close flyby of the Rosetta spacecraft at the asteroid Steins were analyzed with the developed method. Due to the large flyby distance no mass estimate was possible. A feasibility study was carried out for the upcoming flyby of Rosetta in July 2010 at the asteroid Lutetia. It is possible to estimate from this flyby the mass of Lutetia with an error of 1 %.

Moreover, the developed method was applied to measurements of the Mars Express Radio Science Experiment (MaRS) onboard Mars Express (MEX) from two close flybys at the Mars moon Phobos in March 2006 and July 2008. The mass of Phobos was estimated from these flybys. The solution provides the most accurate value currently available for the mass of Phobos from close flybys. Information about the interior were derived from the precise mass estimate. Phobos has a high porosity which is discussed with respect to its origin. It seems to be unlikely that Phobos is a captured asteroid as suggested from first spectral measurements. It seems to be more likely that Phobos is the remnant of the collision between a body originating from the asteroid belt and a body remaining from the formation process of Mars.

Mars Express will perform another flyby in March 2010 with a closest distance of 62 km. A feasibility study was performed from which it was derived that the  $C_{2,0}$  term of the gravity field of Phobos can be estimated with an error of 1 % with the developed method.

## Kurzzusammenfassung

Das Radio Science Verfahren ermöglicht aus Raumsondenmessungen die sehr genaue Bestimmung der Gravitationsparameter von Körpern des Sonnensystems. Dazu wird das Radio Signal zwischen Raumsonde und Bodenstation verwendet. Die Frequenzänderung des Radio Signals ist proportional zur relativen Geschwindigkeitsänderung zwischen Raumsonde und Bodenstation. Fliegt eine Raumsonde nahe an einem Körper vorbei, so wird ihre Geschwindigkeit durch das Schwerefeld verändert. Sind alle Einflüsse bezüglich der Frequenz des Radio Signals außer dem Schwerefeld des Körpers bekannt, so ist die verbleibende Frequenzänderung allein auf das Schwerefeld zurückzuführen. Mit einer Least Square Anpassung können die Gravitationsparameter bestimmt werden.

In dieser Arbeit wurden Modelle entworfen und innerhalb eines Software-Pakets zusammengefasst, mit dem der Orbit einer Raumsonde und die Frequenz, die an der Bodenstation zu erwarten wäre, sehr genau vorhergesagt werden kann. Außerdem wurden Modelle verwendet, um die Frequenzänderungen, die entstehen, wenn das Signal die Erdatmosphäre durchläuft, aus den Messdaten zu entfernen. Die Genauigkeit der Frequenzvorhersage, die in der Arbeit erreicht wurde, liegt dabei im Bereich des Doppler-Geschwindigkeitsfehlers im X-Band auf Grund des thermischen Rauschens der Bodenstation und dem Transponderphasenrauschens des Radio Science Verfahrens.

Das Signal-zu-Rausch-Verhältnis der Messung wurde durch verschiedene Filtertechniken mindestens um den Faktor 3 verbessert. Ein numerisch stabiles Verfahren zur Least Square Anpassung wurde verwendet, um die modellierte Frequenzänderung auf Grund des Schwerefeldes an die gemessene Frequenzänderung anzupassen.

Die Messungen des nahen Vorbeiflugs von Rosetta am Asteroiden Steins wurde mit der entwickelten Methode analysiert. Auf Grund der großen Vorbeiflugs-Entfernung war keine Massenbestimmung möglich. Es wurde eine Machbarkeitsstudie für den Vorbeiflug von Rosetta im Juni 2010 am Asteroiden Lutetia durchgeführt. Es ist möglich mit der entwickelten Methode die Masse von Lutetia auf 1 % genau zu bestimmen.

Die in dieser Arbeit entwickelte Methode wurde bei Messungen des Mars Express Radio Science Experiments auf Mars Express zweier naher Vorbeiflüge am Marsmond Phobos angewandt. Die Masse von Phobos wurde aus den Messungen der Vorbeiflüge mit einer Genauigkeit bestimmt, die bis jetzt bei nahen Vorbeiflügen noch nicht erreicht wurde. Mit der Massenbestimmung konnten weitere Informationen über den inneren Aufbau von Phobos abgeleitet werden. Die dabei bestimmte hohe Porosität von Phobos wurde im Zusammenhang mit seiner Herkunft diskutiert. Es ist unwahrscheinlich, dass Phobos ein eingefangener Asteroid ist, wie es auf Grund der ersten spektralen Messungen vorgeschlagen wurde. Möglicherweise ist Phobos der Überrest eines Zusammenstoßes zwischen einem Körper, der aus dem Asteroiden-Gürtel stammt, und eines Körpers, der bei der Entstehung des Mars gebildet wurde.

Mars Express wird im März 2010 in einer Entfernung von 62 km an Phobos vorbeifliegen. Es wurde eine Machbarkeitsstudie für den Vorbeiflug durchgeführt. Daraus folgt, dass mithilfe der entwickelten Methode der  $C_{2,0}$  Term des Schwerefeldes von Phobos mit einer Genauigkeit von 1 % bestimmt werden kann.

---

# Contents

---

<b>1</b>	<b>Introduction, Motivation and Goal</b>	<b>1</b>
1.1	Analyzing flybys from Radio Science data . . . . .	5
1.2	Missions . . . . .	9
1.2.1	Mars Express . . . . .	9
1.2.2	Rosetta . . . . .	11
<b>2</b>	<b>Theory</b>	<b>13</b>
2.1	Time and reference frames . . . . .	13
2.1.1	Time . . . . .	13
2.1.1.1	Coordinated Universal Time . . . . .	14
2.1.1.2	Ephemeris Time . . . . .	15
2.1.2	Coordinate systems . . . . .	15
2.1.3	Transformation from celestial to terrestrial coordinates . . . . .	17
2.2	Integration of the equation of motion . . . . .	19
2.3	Gravitational forces acting on a spacecraft . . . . .	21
2.3.1	The two-body equation . . . . .	21
2.3.2	The n-body equation . . . . .	23
2.3.3	Sphere of influence . . . . .	24
2.3.4	The gravity potential of a body . . . . .	26

2.3.4.1	Expansion of the gravity potential in spherical harmonics	27
2.3.4.2	Gravitational coefficients . . . . .	28
2.3.4.3	Normalization . . . . .	31
2.3.4.4	Time varying gravitational coefficients . . . . .	31
2.3.5	Numerical computation of the gravitational acceleration of an irregular shaped body . . . . .	32
2.4	Non-gravitational forces acting on a spacecraft . . . . .	37
2.4.1	Solar radiation pressure . . . . .	37
2.4.2	Shadow function . . . . .	39
2.4.3	Atmospheric drag . . . . .	40
2.4.4	Albedo and infrared radiation . . . . .	40
2.4.5	Thrust forces . . . . .	41
2.5	Force model . . . . .	43
2.5.1	Mars Express . . . . .	43
2.5.2	Rosetta . . . . .	47
2.5.3	Precision of the force model . . . . .	48
2.6	The relativistic Doppler effect . . . . .	49
2.6.1	Relativistic summation . . . . .	50
2.6.2	Precise ground station position . . . . .	51
2.6.2.1	Tectonic plate motion . . . . .	51
2.6.2.2	Site displacement due to solid Earth tides . . . . .	52
2.6.2.3	Other effects . . . . .	53
2.7	Data calibration . . . . .	55
2.7.1	Introduction . . . . .	55
2.7.2	Modeling tropospheric delays . . . . .	56
2.7.2.1	Zenith delay . . . . .	56
2.7.2.2	Mapping functions . . . . .	57
2.7.2.3	Comparison . . . . .	57
2.7.3	Ionospheric correction . . . . .	59
2.7.3.1	Correction provided by TSAC . . . . .	60
2.7.3.2	The Klobuchar model . . . . .	60

2.7.3.3	Comparison . . . . .	61
2.7.4	Frequency shift caused by the atmosphere of the Earth . . . . .	62
2.8	Orbit determination and parameter estimation . . . . .	63
2.8.1	Weighted least squares estimation . . . . .	63
2.8.2	Singular value decomposition . . . . .	65
2.8.3	Damping factor . . . . .	65
2.8.4	Error estimation . . . . .	66
2.9	Noise reduction filter . . . . .	67
2.9.1	Noise sources . . . . .	67
2.9.2	Digital filters . . . . .	68
2.9.3	Appropriate filter . . . . .	71
<b>3</b>	<b>Doppler accuracy and curve fitting</b>	<b>73</b>
<b>4</b>	<b>Physical properties of the target bodies</b>	<b>75</b>
4.1	The asteroid 2867 Steins . . . . .	75
4.2	The asteroid 21 Lutetia . . . . .	76
4.3	The Martian moon Phobos . . . . .	77
4.3.1	Shape, topography and volume . . . . .	77
4.3.2	Mass . . . . .	78
4.3.3	The Orbit of Phobos . . . . .	80
4.3.4	Spectral properties . . . . .	81
4.3.5	Origin . . . . .	85
4.3.5.1	Capturing . . . . .	85
4.3.5.2	Accretion in orbit . . . . .	86
<b>5</b>	<b>Results</b>	<b>87</b>
5.1	Phobos . . . . .	87
5.1.1	Results from close flybys . . . . .	87
5.1.1.1	The flyby on 23 March 2006 . . . . .	88
5.1.1.2	The flyby on 17 July 2008 . . . . .	91
5.1.2	Interpretation of the results . . . . .	94

5.1.3	Future flybys in 2010 . . . . .	99
5.2	Steins . . . . .	103
5.3	Lutetia . . . . .	105
<b>6</b>	<b>Discussion and summary</b>	<b>111</b>
<b>A</b>	<b>Appendix</b>	<b>115</b>
A.1	Used parameter . . . . .	115
A.1.1	Masses of solar system bodies . . . . .	115
A.1.2	MEX . . . . .	116
A.1.3	ROS . . . . .	116
A.1.4	Used SPICE-kernels . . . . .	117
A.1.4.1	General kernels . . . . .	117
A.1.4.2	MEX specific kernels . . . . .	118
A.1.4.3	ROS specific kernels . . . . .	118
A.2	Tectonic plate motion . . . . .	119
A.3	Coefficient tableau of integration method . . . . .	119
A.4	Acceleration from unnormalized gravity coefficients . . . . .	120
A.4.1	Recursions . . . . .	120
A.4.2	Acceleration . . . . .	120
A.5	Media correction . . . . .	122
A.5.1	Ionospheric media correction terms . . . . .	122
A.5.2	Ionospheric correction using the differential Doppler . . . . .	123
	<b>Bibliography</b>	<b>125</b>
	<b>Erklärung</b>	<b>134</b>
	<b>Acknowledgements</b>	<b>135</b>

---

## List of Figures

---

1.1	Flow chart of the developed software tool . . . . .	3
1.2	One-way and two-way radio link . . . . .	5
1.3	Comparison of the resulting velocity change at different flyby velocities	7
1.4	Velocity change for different angles $\alpha$ . . . . .	8
1.5	The Mars Express spacecraft . . . . .	9
1.6	The Rosetta spacecraft . . . . .	11
2.1	Difference between time systems . . . . .	14
2.2	The MEX spacecraft reference systems . . . . .	16
2.3	Variations of the Earth Orientation Parameters (EOPs) . . . . .	18
2.4	Geometry for two bodies in an inertial reference frame . . . . .	22
2.5	The n-body problem . . . . .	24
2.6	Sphere of influence . . . . .	25
2.7	Contribution of a small mass element to the gravity potential of a body	26
2.8	Spherical harmonics . . . . .	30
2.9	Resulting forces of incident solar radiation . . . . .	38
2.10	Position and velocity accuracy for MEX . . . . .	44
2.11	Force model of MEX . . . . .	45
2.12	Position and velocity precision for ROS . . . . .	46
2.13	Force model of Rosetta (ROS) . . . . .	48

2.14	Parameter for the computation of the relativistic Doppler effect . . . . .	50
2.15	Comparison tropospheric correction models . . . . .	58
2.16	Comparison of ionospheric correction models . . . . .	61
2.17	The frequency correction for the atmosphere of the Earth . . . . .	62
2.18	Comparison of filter with different parameter . . . . .	70
3.1	Difference between predicted and measured frequency . . . . .	74
3.2	First guess frequency residuals . . . . .	74
4.1	The asteroid Steins . . . . .	76
4.2	Grooves on the surface of Phobos . . . . .	77
4.3	The Stickney crater and other surface features of Phobos . . . . .	78
4.4	Comparison of Phobos ephemerides . . . . .	81
4.5	The two spectral units of Phobos . . . . .	81
4.6	The bluer unit of Phobos . . . . .	82
5.1	Usual geometry for flybys of MEX at Phobos . . . . .	87
5.2	Kaiser filter cut off frequency for the Phobos flyby in 2006 . . . . .	88
5.3	Moving average sample time for the Phobos flyby in 2006 . . . . .	88
5.4	Frequency residuals from the Phobos flyby in 2006 . . . . .	90
5.5	Frequency residuals from the Phobos flyby in 2008 . . . . .	90
5.6	Kaiser filter cut off frequency for the Phobos flyby in 2008 . . . . .	91
5.7	Moving average sample time for the Phobos flyby in 2008 . . . . .	91
5.8	Comparison of past mass estimates with new results . . . . .	93
5.9	Comparison of Phobos bulk density . . . . .	95
5.10	Phobos porosity . . . . .	96
5.11	Comparison of the macroporosity of asteroids . . . . .	97
5.12	Ground station visibility during the Phobos flyby in March 2010 . . . . .	99
5.13	Estimated frequency change at the flyby in March 2010 . . . . .	100
5.14	Filtered frequency change of $C_{2,0}$ . . . . .	100
5.15	Predicted frequency change caused by the gravitational attraction of as- teroid Steins . . . . .	104
5.16	Frequency residuals at Steins flyby . . . . .	104

---

5.17	Ground station visibility during the Lutetia flyby . . . . .	105
5.18	Frequency change due to the gravitational attraction of asteroid Lutetia	106
5.19	Frequency change with noise . . . . .	106
5.20	Different measurement scenarios of the Lutetia flyby . . . . .	108
5.21	Kaiser filter cut-off frequency for Lutetia flyby . . . . .	108
5.22	Moving average sample time for Lutetia flyby . . . . .	109
5.23	Different measurement scenarios of the Lutetia flyby around Closest Approach (CA) . . . . .	110
A.1	Execution scheme for recurrence coefficients computation. . . . .	121



---

## List of Tables

---

2.1	Summary of site displacement effects . . . . .	54
2.2	Doppler velocity error . . . . .	68
4.1	Summary of the physical parameters of the asteroid Lutetia . . . . .	76
4.2	Previous mass estimates of Phobos . . . . .	79
4.3	Bulk density and grain density of meteorite analogues . . . . .	83
4.4	Summary of results from spectral measurements of Phobos . . . . .	84
5.1	Lutetia flyby scenarios . . . . .	109
A.1	Masses of Solar System Bodies . . . . .	115
A.2	Optical properties of MEX . . . . .	116
A.3	Optical properties of ROS . . . . .	116
A.4	Tectonic plate motion parameter . . . . .	119
A.5	The coefficient tableau of the RK5(4) integration method . . . . .	119



---

# Acronyms

---

**AU** Astronomical Unit

**CA** Closest Approach

**CEP** Celestial Ephemeris Pole

**CNES** Centre National d'Etudes Spatiales

**CRISM** Compact Reconnaissance Imaging Spectrometer for Mars

**DSN** Deep Space Network

**EOPs** Earth Orientation Parameters

**ESA** European Space Agency

**ESOC** European Space Operation Center

**ET** Ephemeris Time

**GINs** Geodesie par Integrations Numeriques Simultanees

**GAST** Greenwich Apparent Sidereal Time

**GMST** Greenwich Mean Sidereal Time

**GPS** Global Positioning System Time

**HGA** High Gain Antenna

**IMP** Imager for Mars Pathfinder

**IRTF** NASA Infrared Telescope Facility on Mauna Kea, Hawai

**ITRF** International Terrestrial Reference Frame

**JPL** Jet Propulsion Laboratory

**LOD** Length of Day

**LOS** Line of Sight

**M9** Mariner 9

**MaRS** Mars Express Radio Science Experiment

**MGS** Mars Global Surveyor

**ODY** Mars Odyssey

**MRO** Mars Reconnaissance Orbiter

**MEX** Mars Express

**NAIF** The Navigation and Ancillary Information Facility

**OMEGA** Visible and Infrared Mineralogical Mapping Spectrometer on Mars Express

**PBU** Phobos bluer unit

**PRU** Phobos redder unit

**ROS** Rosetta

**SVD** Singular Value Decomposition

**SPICE** Information system to assist scientists in planning and interpreting scientific observations from space-based instruments (see *NAIF* [2009])

**SRC** Super Resolution Channel

**TAI** International Atomic Time

**TCB** Barycentric Coordinate Time

**TCG** Geocentric Coordinate Time

**TDB** Barycentric Dynamic Time

**TSAC** Tracking System Analytic Calibration

**TDT** Terrestrial Dynamic Time

**TT** Terrestrial Time

**UT1** Universal Time

**UTC** Coordinated Universal Time

**VL2** Viking Lander 2

**VOI** Viking Orbiter I

**VOII** Viking Orbiter II

**WoL** Wheel off-Loading

---

# Introduction, Motivation and Goal

---

The Mars Express (MEX) spacecraft was successfully launched on 2 June 2003 and injected into orbit around Mars on 25 December 2003. It was maneuvered into a highly elliptical capture orbit from which transited into its operational near polar orbit later in January 2004. The elliptical polar orbit (radius of periapsis  $r_p = 250$ , radius of apoapsis  $r_a = 10142$  km, inclination  $i = 86.35^\circ$ , period  $T = 6.75$  h) of Mars Express allows close flybys at the Mars moon Phobos which have been the first close flybys since Viking and Phobos 2 twenty years ago. Phobos is a scientifically very interesting body. Different scenarios for its origin exist but none of them explains its origin entirely.

This PhD-thesis was motivated by the opportunity of having close flybys at Phobos from which new scientific results of Phobos can be achieved. The Mars Express Radio Science Experiment (MaRS) (*Pätzold et al.* [2004]) obtains tracking data from these flybys. The Radio Science experiment technique enables the precise estimation of the mass and additional gravitational parameters of Phobos. It uses the radio link between ground station and spacecraft. The tracking data contain the frequency of the radio signal observed at the ground station. The observed frequency is proportional to the relative velocity between the spacecraft and the ground station.

The Radio Science measurement principle is based on the detection of a change in frequency of the radio signal. This frequency shift can be caused by the propagation of the radio wave through a medium and/or the change of the relative velocity between the spacecraft and the ground station by an unknown force like the gravitational attraction of a perturbing body (*Häusler* [2002]). For close flybys the latter frequency shift is used for estimating the gravitational parameter of a perturbing body from the trajectory of a spacecraft.

The orbit of MEX around Mars is perturbed by the gravitational attraction of the co-orbiting moon Phobos. The orbit perturbations caused by the gravitational attraction of Phobos on the spacecraft can be measured by:

- long-term observation of the spacecraft orbit at large distances from that moon, or by
- short-term observation of the changes in the spacecraft velocity during close flybys.

Each flyby has its own characteristics. The shape of the Doppler frequency shift curve caused by the gravitational attraction of Phobos on the spacecraft depends on the relative flyby velocity, the angle between the Line of Sight (LOS) and the velocity vector of the spacecraft, the closest distance, and the mass of the perturbing body (*Pätzold et al.* [2001]). In this thesis the analysis of close flybys is focused on fitting gravitational parameters to the individual shape of the frequency curve instead of using large datasets as for long-term observations (see *Konopliv et al.* [2006], *Rosenblatt et al.* [2008]) for computing the mass of the perturbing body. The shape of the curve is obtained from the recorded frequency if all other effects except for the gravitational attraction of the perturbing body are known. Based on this knowledge a predicted frequency is computed and subtracted from the recorded data.

The goal of this thesis is to develop a software tool which allows on the one hand the precise orbit computation from which the predicted frequency can be determined. On the other hand, obtaining gravitational parameters from the measured frequency residuals from short-term observations after calibration and filtering by fitting the predicted frequency shift of the perturbing body on the measured frequency residuals. From the estimated gravitational parameters, additional information about the interior of the perturbing body can be derived. Figure 1.1 summarizes the steps needed to be performed for this goal.

The first part contains the precise estimate of the predicted frequency expected to be received at the ground station. This includes appropriate time and coordinate systems for Radio Science experiments defined in section 2.1. A method for solving the equation of motion is described in section 2.2.

A spacecraft orbiting a central body can be perturbed by many forces. These forces have to be taken into account for a precise orbit determination which is one of the most essential parts in order to extract gravitational parameters from Radio Science data. The gravitational and non-gravitational forces acting on a spacecraft are described in section 2.3 and 2.4, respectively. This includes the acceleration caused by a non-spherical shaped body with nonuniform density distribution for which a novel recursion algorithm for normalized gravity coefficients is developed based on an algorithm from *Cunningham* [1970]. The gravitational attractions from third or more bodies are also defined. Detailed models for the solar radiation pressure depending on the optical parameter of the spacecraft and the direction of the normal of each plane of the spacecraft to the Sun and other perturbing forces are specified in detail.

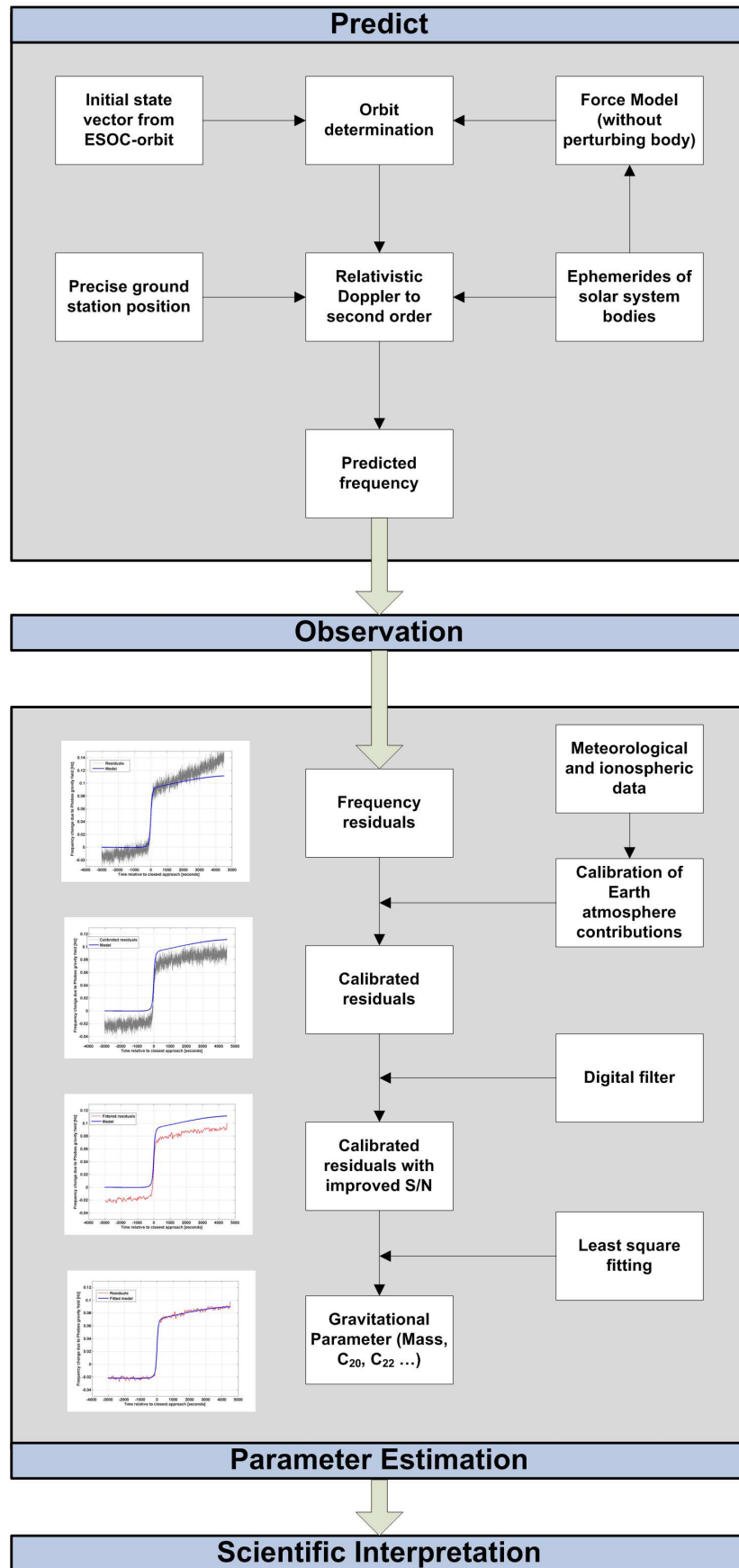


*Figure 1.1:* Flow chart describing the major steps of the developed software tool. The upper part describes the computation of the predicted frequency and the lower part the subtraction of the gravitational parameter including calibration and noise reduction by filtering.

The method in this thesis was primarily developed to analyze flybys at the Mars moon Phobos. The Rosetta spacecraft has performed on its way to the comet 67P/Churyumov-Gerasimenko one flyby at the asteroid 2867 Steins in 2008 and will perform another flyby at the asteroid 21 Lutetia in 2010. Therefore, the method of analyzing close flybys was extended to the flybys of Rosetta.

Force models appropriate for Mars Express and Rosetta are described. Their accuracy is estimated by comparing the state vector from the orbit integration with the state vector from precise orbit determination of other investigators.

Based on the precise orbit determination the predicted frequency which is expected to be received at the ground station is computed from the relativistic Doppler effect. This requires the knowledge of the very accurate position at centimeter level of the transmitting and receiving ground station, i.e. site displacement effects like tectonic plate motion must be taken into account. Numerical methods for modeling this effects and the relativistic Doppler effect are presented in section 2.6.

The radio signal transmitted from the ground station to the spacecraft and the way back passes the troposphere and ionosphere of the Earth. The frequency of the signal is changed due to the propagation through these media. Numerical methods for predicting and removing this effect from the recorded data are described in section 2.7.

After applying all corrections, the frequency shift caused by the gravitational attraction of the perturbing body is obtained from the recorded data by subtracting the predicted frequency (all forces are included except the gravitational attraction of the perturbing body) from the recorded frequency.

In section 2.8 a numerical stable formalism for fitting the gravitational parameter of the body onto the frequency residuals is described. The error of the estimated gravitational parameter is reduced by applying appropriate filter techniques (see section 2.9). Observations from MaRS at which no perturbing body is included were used in section 3 to estimate the accuracy of the predicted frequency expected to be received at the ground station. Moreover, the fitting procedure for close flyby observations is defined in this section. The current knowledge of the physical properties of the Mars moon Phobos, the asteroids Steins and Lutetia is briefly summarized in section 4.

The mass estimate results from the MEX flybys at the Martian moon Phobos in March 2006 and July 2008 are given in section 5. From this estimates conclusions about the interior are drawn and interpretations with respect to its origin are drawn. Furthermore, the results of a feasibility study for an upcoming flyby in March 2010 of MEX at Phobos at a distance of 62 km are shown. The results from the flyby of ROS at Steins in September 2008 and a feasibility study for the future flyby at Lutetia in July 2010 are presented in section 5. Finally, section 6 summaries and discusses the results of this thesis.

## 1.1 Analyzing flybys from Radio Science data

Radio Science techniques are applied to the study of planetary and cometary atmospheres, planetary rings and surfaces, gravity and the solar corona. The radio carrier links of the spacecraft Telemetry, Tracking and Command subsystem between the Orbiter and Earth are used for Radio Science observations. Simultaneous and coherent dual-frequency downlinks at X-band (8.4 GHz) and S-band (2.3 GHz) via the High Gain Antenna permits separation of contributions from the classical Doppler shift and the dispersive media effects caused by the motion of the spacecraft with respect to the Earth and the propagation of the signals through the dispersive media, respectively.

The investigation relies on the observation of the phase, amplitude, polarization and propagation times of radio signals transmitted from the spacecraft and received with antennas on Earth. The radio signals are affected by the medium through which they propagate (atmospheres, ionospheres, interplanetary medium, solar corona), by the gravitational influence of the planet or moon on the spacecraft and, finally, by the performances of the various systems aboard the spacecraft and on Earth. Radio Science investigations fall into three broad categories: propagation of the radio signal through the ionosphere and neutral atmosphere of the occulted planet (occultation measurements), oblique incidence scattering investigations using propagation paths between spacecraft, planetary surface and a ground station on Earth (bistatic radar measurements), and gravity measurements (*Pätzold et al.* [2004], *Häusler* [2002]).

In this thesis only gravity observations are used which are usually performed in the two way mode (Fig. 1.2), i.e. a ground station is transmitting a radio signal (uplink) at X-band which is received by the spacecraft, converted by the spacecraft's transponder to downlink transmission frequency at S-band and X-band, and sent back to the ground station (*Pätzold et al.* [2004]).

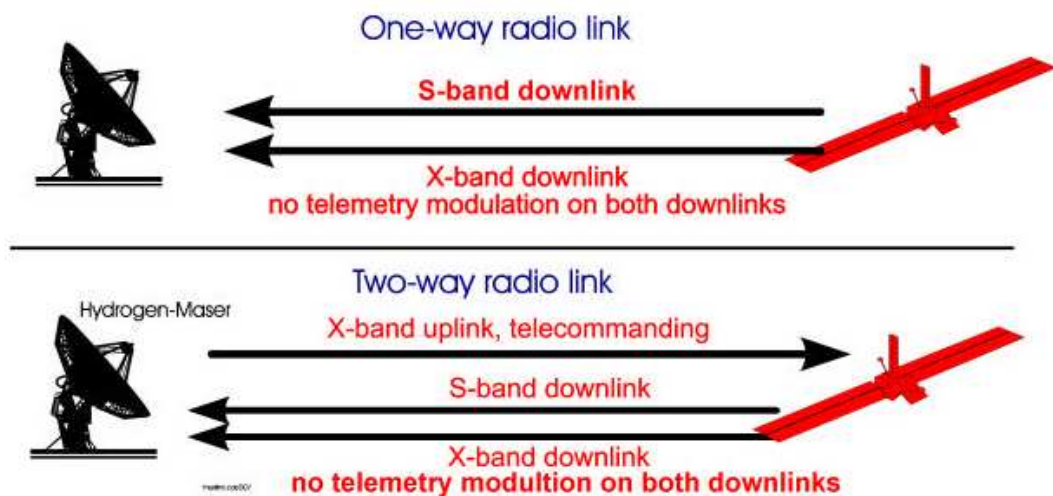


**Figure 1.2:** One-way and two-way radio link configuration (Source: *Pätzold et al.* [2004]).

If the radio path is well clear of occulting material and a spacecraft is approaching a solar system body the gravitational attraction of the body is changing the velocity and trajectory of the spacecraft. When neglecting relativistic effects, the change in velocity is detected in the transmitted radio signal from a frequency shift caused by the classical Doppler effect. This frequency shift can be expressed by

$$\Delta f = \pm f \frac{\Delta \dot{r}}{c}. \quad (1.1)$$

Here,  $\Delta \dot{r}$  is the velocity change of the spacecraft projected into the Line of Sight (LOS),  $c$  the speed of light,  $\Delta f$  the frequency shift and  $f$  the transmitted frequency (*Pätzold et al.* [2001]).

If a spacecraft performs a close flyby at a solar system body, the velocity of the spacecraft is changed by the gravitational attraction of the body. If all other contributions on the radio signal are known the remaining frequency change is solely due to the gravitational attraction. This frequency shift allows to gain information about the gravitational parameter of the perturbing body. The amplitude and shape of this frequency shift curve depends on different parameters:

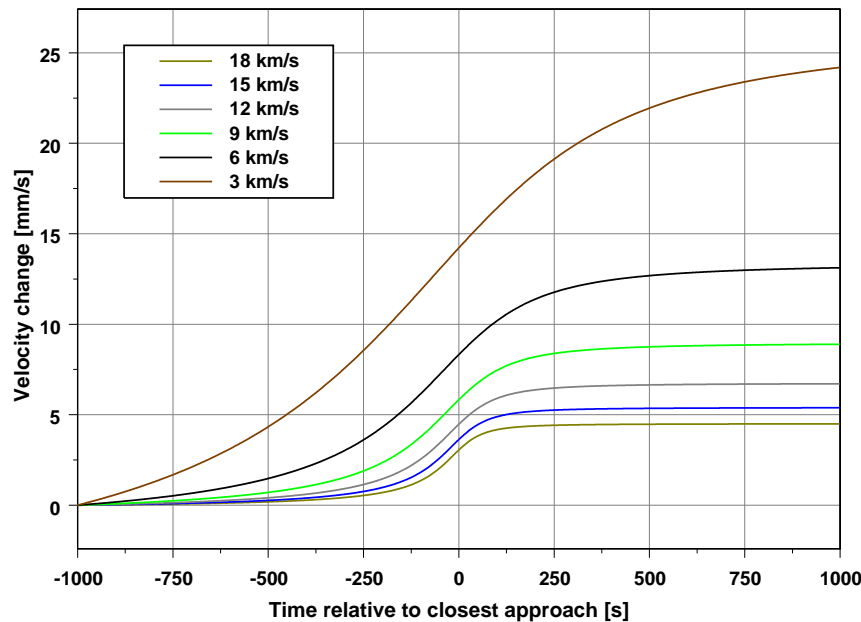
- the mass of the perturbing body (the change in velocity increases with the mass of the body for a given distance),
- the distance between the spacecraft and the perturbing body (the change in velocity increases with closer distance for a given mass, obviously),
- the relative flyby velocity between spacecraft and body (small relative velocities causing larger velocity changes than larger relative velocities, see Figure 1.3), and
- the angle  $\alpha$  between the LOS, i.e. the direction of the line connecting the spacecraft at transmitting time and the ground station at receiving time (in the down-link case), and the direction of the velocity of the spacecraft relative to the perturbing body.

The velocity change caused by the gravitational attraction of the perturbing body is separated into two components  $\mathbf{v}_{\parallel}$  and  $\mathbf{v}_{\perp}$ , along the direction of motion of the spacecraft and perpendicular to it (*Pätzold et al.* [2001]), respectively. The two components are projected into the LOS by

$$\mathbf{v}_{Los} = \mathbf{v}_{\perp} \sin(\alpha) + \mathbf{v}_{\parallel} \cos(\alpha) . \quad (1.2)$$

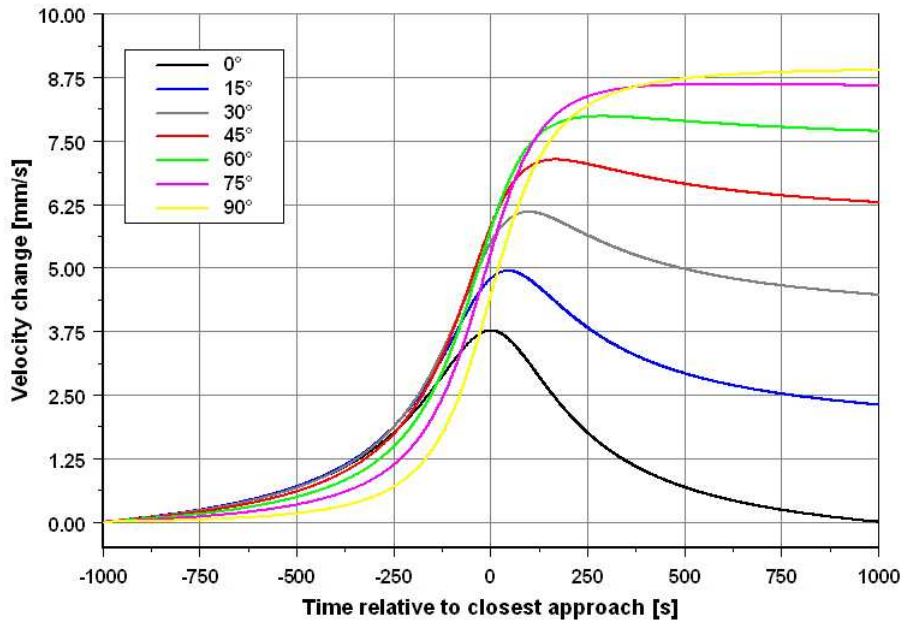
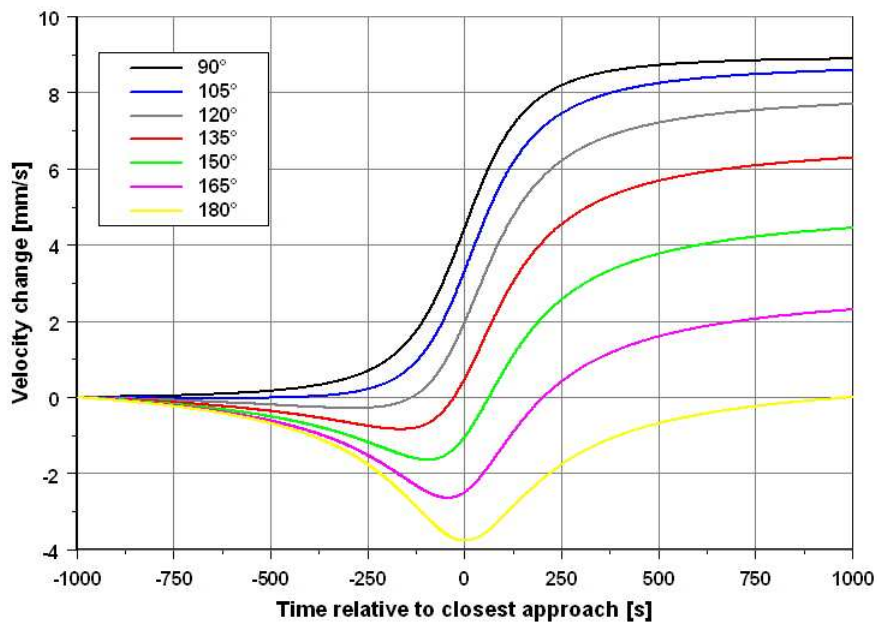
The shape of the resulting frequency change in the recorded data from a close flyby contains not only the information on the gravitational parameter of the perturbing body, but depends also on the characteristics of the flyby. The geometry of the flyby determines these characteristics, i.e. the flyby velocity (Fig. 1.3), the distance between the spacecraft and the perturbing body, and the angle between LOS and direction of

motion (Fig. 1.4(a) and 1.4(b)). The geometry is well known for every flyby. The unknown parameters are the gravitational parameter of the perturbing body. If a predicted frequency is subtracted from the observed data in that way that a curve as shown in Figure 1.4(a) and 1.4(b) remains, this curve can be used to extract gravitational parameter from it by a least square fit. Thus it is possible to estimate from short-term observations including the explicit shape of the frequency shift the gravitational parameter of the perturbing body.



**Figure 1.3:** Comparison of the resulting velocity change at different flyby velocities with constant mass and flyby distance. The velocity is not projected into the Line of Sight (LOS). The resulting velocity change increases with decreasing relative velocity between spacecraft and ground station.

A method is developed in this thesis which focuses on the shape of the resulting frequency changes, i.e. the gravitational parameter are the variables which are fit to the frequency change. It is assumed that the frequency change is solely due to the attraction of the perturbing body. This requires a very precise prediction and assessment of all other forces acting on the spacecraft (see section 3). For Mars Express and Rosetta the total Doppler velocity error caused by thermal noise at the ground station and transponder phase noise is 0.26 mm/s at X-band (Pätzold *et al.* [2004]). Therefore, the precision of the predicted frequency change should be in the order of the total Doppler velocity for a precise estimate of the gravitational parameters of the perturbing body.

(a)  $\alpha = 0^\circ - 90^\circ$ (b)  $\alpha = 90^\circ - 180^\circ$ 

**Figure 1.4:** Velocity changes in the direction of the Line of Sight for different angles  $\alpha$  between the Line of Sight (LOS) and the direction of motion of the spacecraft with the same body mass, flyby distance and relative flyby velocity.

## 1.2 Missions

### 1.2.1 Mars Express

The Mars Express spacecraft (Fig. 1.5) was launched on a Soyuz/Fregat, built by Starsem, the European/Russian launcher consortium on 2 June 2003 with a launch mass of 1120 kg (including 113 kg orbiter payload and 60 kg lander) and arrived in December 2003 Mars. The scientific payload consists of the High Resolution Stereo Camera (HRSC), the Energetic Neutral Atoms Analyzer (ASPERA), the Planetary Fourier Spectrometer (PFS), the Visible and Infrared Mineralogical Mapping Spectrometer (OMEGA), the Sub-Surface Sounding Radar Altimeter (MARSIS), the Ultra-violet and Infrared Atmospheric Spectrometer (SPICAM) and the Mars Express Radio Science Experiment (MaRS) (*ESA [2009a]*).

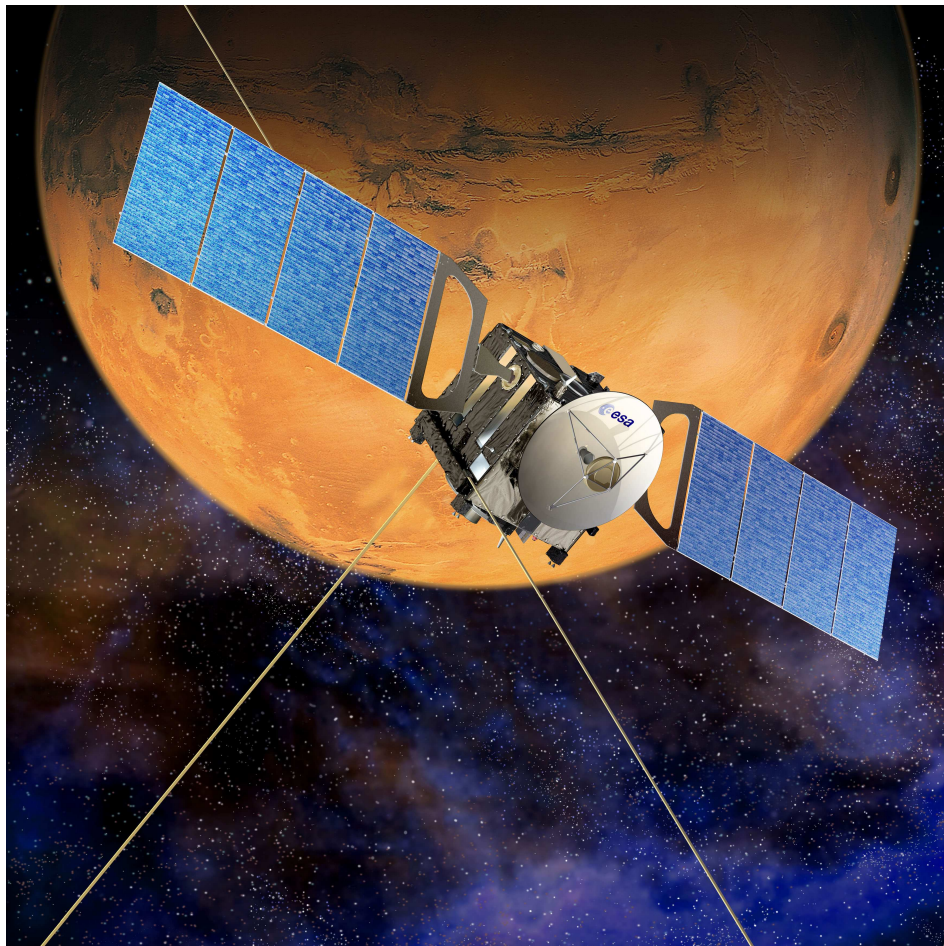


**Figure 1.5:** Artist view of the Mars Express spacecraft in front of Mars (source *ESA [2009a]*).

The Mars Express Orbiter will:

- image the entire surface at high resolution (10 meters/pixel) and selected areas at super resolution (2 meters/pixel);
- produce a map of the mineral composition of the surface at 100 meter resolution;
- map the composition of the atmosphere and determine its global circulation;
- determine the structure of the sub-surface to a depth of a few kilometers;
- determine the effect of the atmosphere on the surface;
- determine the interaction of the atmosphere with the solar wind.

Detailed information about the MEX mission are given by *Chicarro et al.* [2004] and *ESA* [2009a].

The Mars Express Radio Science Experiment (MaRS) will use the radio signals that convey data and instructions between the spacecraft and Earth to probe the planet's ionosphere, atmosphere, surface and even the interior. Information on the interior will be gleaned from the planet's gravity field, which will be calculated from changes in the velocity of the spacecraft relative to Earth. Surface roughness will be deduced from the way in which the radio waves are reflected from the Martian surface (*Pätzold et al.* [2004]).

### 1.2.2 Rosetta

The Rosetta spacecraft (Fig. 1.6) was launched on 2 March 2004 by an Ariane-5G rocket from Kourou, French Guiana. After burn-out of the lower stage, the spacecraft and upper stage remained in Earth parking orbit ( $4000 \times 200$  kilometers) for about two hours. Ariane's upper stage then ignited to boost Rosetta into its interplanetary trajectory, before separating from the spacecraft (ESA [2009b]).

After a ten-year voyage, the final target of the Rosetta mission is comet 67P/Churyumov-Gerasimenko. The journey contains 3 Earth swing-by manoeuvres (4 March 2005, 13 November 2007, 13 November 2009), one Mars swing-by manoeuvre on 25 February 2007, two Asteroid flybys at Steins (5 September 2008) and Lutetia (10 June 2010) before the Comet rendezvous manoeuvres (22 May 2014) and Lander delivery (10 November 2014) will take place. The comet will be escorted around the Sun from November 2014 - December 2015 and end of the nominal mission will be in December 2015.

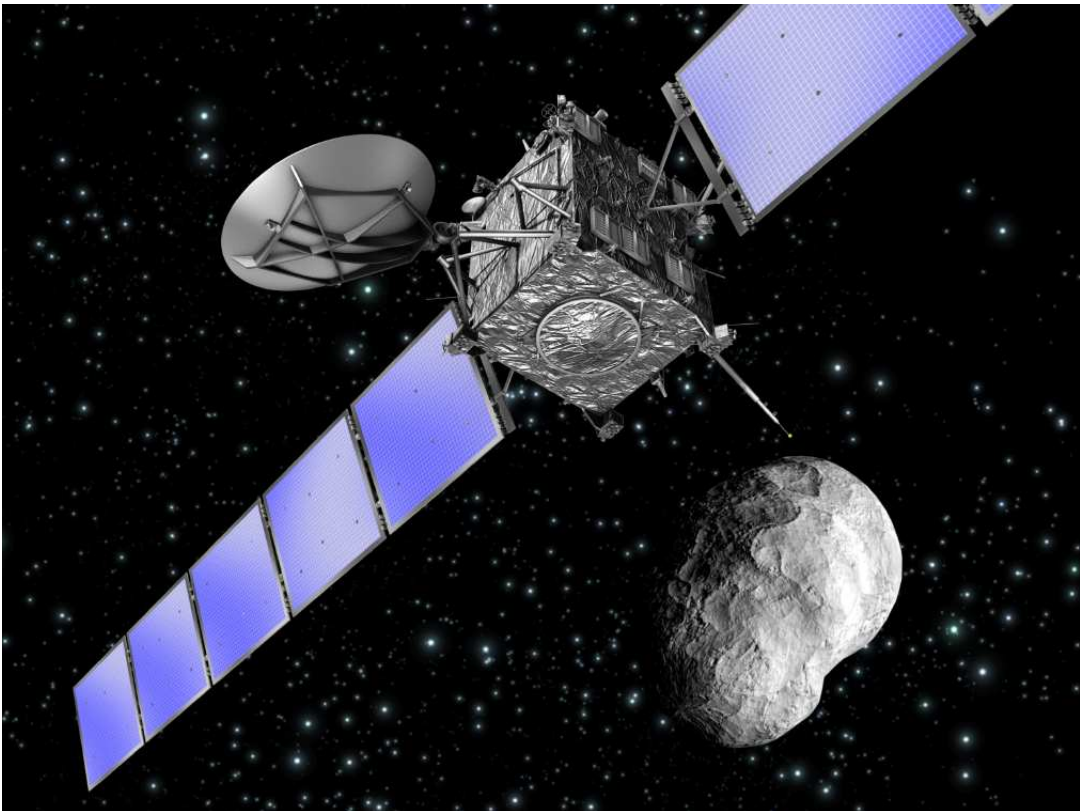


**Figure 1.6:** Artist view of the Rosetta spacecraft as it flies by asteroid Steins (source ESA [2009b]).

The Rosetta orbiter is equipped with eleven scientific instruments: the Ultraviolet Imaging Spectrometer (ALICE), the Comet Nucleus Sounding (CONSERT), the Cometary Secondary Ion Mass Analyser (COSIMA), the Grain Impact Analyser and Dust Accumulator (GIADA), the Micro-Imaging Analysis System (MIDAS), the Microwave Instrument for the Rosetta Orbiter (MIRO), the Rosetta Orbiter Imaging System (OSIRIS), the Rosetta Orbiter Spectrometer for Ion and Neutral Analysis (ROSINA), the Rosetta Plasma Consortium (RPC), the Visible and Infrared Thermal Imaging Spectrometer (VIRTIS) and the Radio Science Investigation (RSI).

---

# Theory

---

## 2.1 Time and reference frames

Analyzing data from Radio Science measurements requires a definition of various time systems and reference frames which are suitable for this specific application. Important is, for example, the reference time when the signal transmitted by the spacecraft is received at the ground station.

The software package SPICE (*NAIF* [2009]) used in this thesis provides various built-in time and reference frames and the corresponding transformations between them. The time and reference frames used for the computations are briefly explained in the following.

More information about time and reference frames can be found in *Häusler et al.* [2003], *Selle* [2005], *Montenbruck and Gill* [2000], *Dehant and Mathews* [2007] and *Valado* [2001].

### 2.1.1 Time

The position of the spacecraft and the receiving ground station has to be known very precisely in different time systems. E.g. the position of a planet is based on the Ephemeris Time (ET) and the data recorded at the ground station are referenced to the Coordinated Universal Time (UTC). There are four time scales: sidereal time, solar (universal time), dynamical time, and atomic time. Sidereal time and solar time are based on the rotation of the Earth and are related together by mathematical transformations. Atomic and Dynamical time are not depending on other time scales.

Universal times UT and UT1 are sub timescales of the mean solar time, ET, Terrestrial Time (TT), Barycentric Dynamic Time (TDB), Terrestrial Dynamic Time (TDT), Barycentric Coordinate Time (TCB) and Geocentric Coordinate Time (TCG) of the dynamical time, and International Atomic Time (TAI) and Global Positioning System Time (GPS) of the atomic time (see Figure 2.1). In this thesis UTC and ET is used.

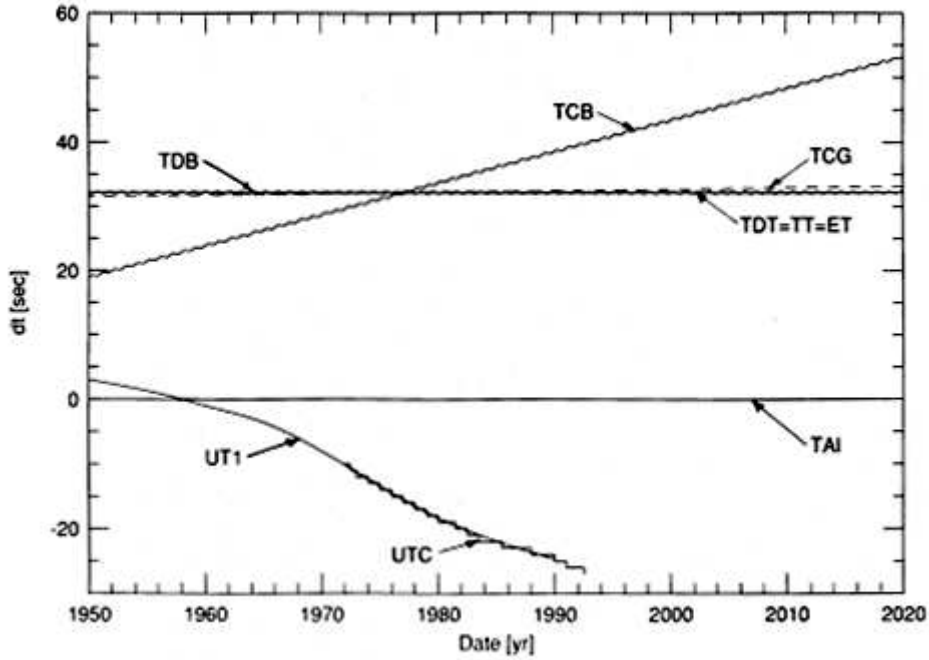


**Figure 2.1:** Difference between Barycentric Coordinate Time (TCB), Barycentric Dynamic Time (TDB), Geocentric Coordinate Time (TCG), Terrestrial Time (TT) or former Terrestrial Dynamic Time (TDT), International Atomic Time (TAI), Universal Time (UT1), Global Positioning System Time (GPS) and Coordinated Universal Time (UTC) between 1950 and 2020. The periodic terms of TCB and TDB are magnified by 100 to make them visible (Source: Seidelmann and Fukushima [1992]).

### 2.1.1.1 Coordinated Universal Time

The Coordinated Universal Time (UTC) has a nonuniform time scale and is obtained from atomic clocks which are running at the same rate as TT or former TDT and TAI. TT and TAI have uniform time scales based on atomic clocks which are located at the surface of Earth. UTC is referenced to TAI which has an uniform time scale but due to the introduction of leap seconds the UTC has a nonuniform time scale. This ensures that the UTC time scale is always within 0.7 seconds of UT1. The UT1 represents the time scale of mean solar time with an average length of solar day of 24 hours with  $UT1 = UT$ . UT1 takes into account the actual rotation of the Earth. Therefore the length of one second of UT1 is not constant due to the apparent motion of the Sun and the rotation of the Earth (see figure 2.1).

### 2.1.1.2 Ephemeris Time

The Ephemeris Time (ET) is the uniform time scale that is represented by the independent variable in the differential equations that describe the motions of the planets, Sun and Moon and is defined as TDB seconds past the Greenwich noon on 1 January 2000 Barycentric Dynamic Time (TDB), below referred to as the J2000 epoch. ET can be expressed in form of TDB or TDT, but in this thesis the TDB representation is used. It is defined as the basic time system for all computations.

The difference between the UTC and TDB representation is computed from

$$t_{TDB} = t_{UTC} + t_{Leap} + 32.184 [s] + \Delta t_{TDB,TT}. \quad (2.1)$$

Here  $t_{Leap}$  are the leap seconds and  $\Delta t_{TDB,TT}$  the difference between TT and TDB.

### 2.1.2 Coordinate systems

A coordinate system is usually defined by its origin, fundamental plane, the preferred direction and additionally the sense, or the positive direction. Different coordinate systems are used in the present thesis. Their definition and utilization are below. The names of the coordinate systems are according to the nomenclature from the SPICE software package.

- Geocentric Celestial Reference Frame J2000:

This frame has the Earth mean equator of the J2000 epoch, which is the epoch of Greenwich noon on 1 January 2000 TDB as its principal plane and has no rotation in space. The first axis of this frame is in the direction of the vernal equinox and the second is in the direction of the increasing obliquity. This is the fundamental inertial coordinate system in which the equation of motion of the spacecraft is solved.

- International Terrestrial Reference Frame ITRF93:

This frame is fixed to the Earth, with the center of mass being defined for the entire Earth, including oceans and atmosphere. It is defined through coordinates assigned to a number of sites for which the various effects of site displacement are taken into account. Consequently, the motion of these sites reflects the rotation of the Earth entirely. ITRF93 has the plane of the true equator as its principal plane and its first axis fixed on the Greenwich meridian. In this frame the precise position of the transmitting and receiving ground stations are calculated (see section 2.6.2).

- Body fixed frame IAU\_MARS of Mars:

This frame is fixed to and does not move with respect to surface features of Mars, but it does move with respect to inertial frames as Mars rotates. The origin is the center of mass of Mars. The principal plane is the plane of Mars's equator

as defined by *Seidelmann et al.* [2001]. This frame is used for computation of the acceleration felt by a spacecraft orbiting Mars from the gravitational field.

- The solar array frames  $MEX\_SA+Y$  and  $MEX\_SA-Y$  of MEX:

The orientation of the solar panels of MEX with respect to the direction to Sun are needed for a precise computation of the acceleration caused by the solar radiation pressure. This can be realized using the following solar array frames of the left and right solar array  $MEX\_SA+Y$  and  $MEX\_SA-Y$ , respectively. It is defined such as (see figure 2.2)

- the origin of the frame is located at the geometric center of the yoke,
- $+Y$  is parallel to the longest side of the solar array, positively oriented from the yoke to the end of the wing,
- $+Z$  is normal to the solar array plane and the solar cells are facing  $+Z$ , and
- $+X$  is defined such that  $(X, Y, Z)$  is right handed.

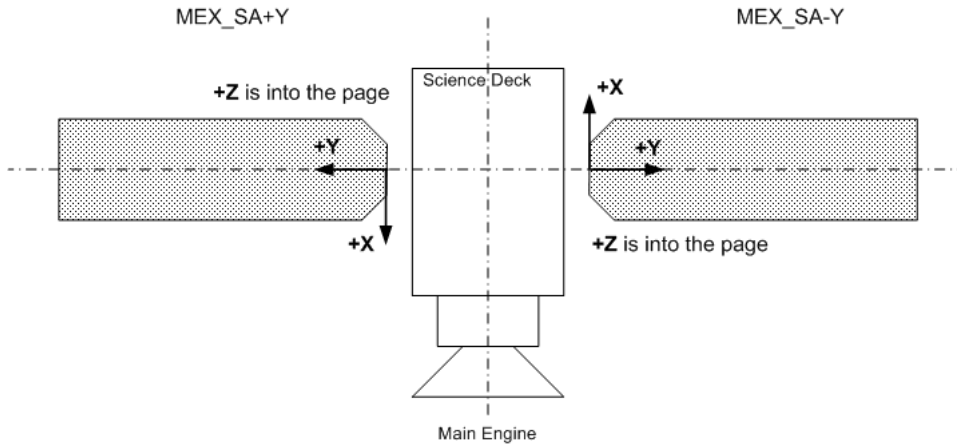


**Figure 2.2:** The MEX spacecraft reference system.

- The solar array frames  $ROS\_SA+Y$  and  $ROS\_SA-Y$  of ROS:

The orientation of the solar panels of ROS can be computed using the solar array frames.  $ROS\_SA+Y$  and  $ROS\_SA-Y$  defined similar to that of MEX (Fig. 2.2):

- the origin of the frame is located at the geometric center of the gimbal,
- $+Y$  axis is parallel to the longest side of the array and array rotation axis, and is positively oriented from the end of the wing toward the gimbal,
- $+Z$  axis is normal to the solar array plane, the solar cells on the  $+Z$  side, and
- $+X$  axis is defined such that  $(X, Y, Z)$  is right handed.

### 2.1.3 Transformation from celestial to terrestrial coordinates

Orbit determination from Doppler data requires both celestial reference frames defining a Newtonian-inertial frame, in which the equation of motion can be solved and terrestrial reference frames in which the position of a ground station is defined. The Earth Orientation Parameters (EOPs) establish a connection between these two frames. The EOPs required for a precise transformation between the celestial reference frame and the terrestrial reference frame are provided by *IERS* [2009] and used in form of SPICE kernels. The necessary equations for the transformations are incorporated into the SPICE software package according to *McCarthy and Petit* [2003]. Therefore only a short description of the above mentioned transformation is given below.

Variations in the orientation in space of an Earth-fixed reference frame are driven by variations in the Earth rotation, i.e., in the angular velocity vector of Earth rotation. The rotation of the solid Earth changes as a result of external torques, internal mass redistributions, and the transfer of angular momentum between the solid Earth and the fluid regions. This manifests in variations in direction of Earth-related axes in space (precession and nutation) as well as relative to a terrestrial reference frame (offset of the direction of the rotation axis with the figure axis, polar motion), and also as variation in the angular speed of rotation which translates into variations in the Length of Day (LOD) (see Figure 2.3). Taking into account these effects, the transformation of a position vector  $\mathbf{r}_{ITRF93}$  in the terrestrial coordinate system ITRF93 into the celestial coordinate system J2000 can be carried out via the following transformation rule

$$\mathbf{r}_{J2000} = \mathbf{\Pi}(t) \mathbf{N}(t) \mathbf{\Phi}(t) \mathbf{P}(t) \mathbf{r}_{ITRF93}. \quad (2.2)$$

Here,  $\mathbf{\Pi}(t)$ ,  $\mathbf{N}(t)$ ,  $\mathbf{\Phi}(t)$  and  $\mathbf{P}(t)$  are the rotation matrices describing the coordinate changes due to precession, nutation, Earth rotation, and polar motion, respectively. In detail

- **Precession  $\mathbf{\Pi}(t)$ :**

The orbital plane of the Earth is perturbed from the masses of solar system bodies, this effect is called the planetary precession. The axis of rotation of the Earth is also influenced by the torque which acts on the equatorial wobble from Sun and moon. This is called the lunisolar precession.

- **Nutation  $\mathbf{N}(t)$ :**

The orientation of the axis of rotation of the Earth is also perturbed by small periodic perturbations that are known as nutation (see Figure 2.3). They are caused by monthly and annual variations of the lunar and solar torques which have been averaged in the consideration of precession.

- **Earth rotation about the Celestial Ephemeris Pole (CEP)  $\mathbf{\Phi}(t)$ :**

The precession and nutation mentioned above is derived using the CEP, which differs slightly from the instantaneous rotation axis. The rotation about the CEP axis itself is described by the Greenwich Mean Sidereal Time (GMST) that

measures the angle between the mean vernal equinox and the Greenwich Meridian. The GMST can be computed from the difference between UT1 and UTC or UT1 and TAI which is published by *IERS* [2009] and is the instantaneous rate of change of UT1 in seconds, i.e. LOD with respect to a uniform time scale (UTC or TAI).

Similar the Greenwich Apparent Sidereal Time (GAST) measures the hour angle of the true equinox. Both values differ by the nutation in right ascension and are related by the equation of the equinoxes. The transformation matrix  $\Phi(t)$  yields the transformation between the true-of-date coordinate system and a system aligned with the Earth equator and Greenwich meridian from the apparent sidereal time.

- **Polar motion  $P(t)$ :**

The Celestial Ephemeris Pole is not fixed with respect to the surface of the Earth and performs a periodic motion around its mean position from which it differs at most 10 m. The polar motion is actually a superposition of mostly two components. Firstly the free precession with a period of about 435 days, the so called Chandler period, and secondly an annual motion that is influenced by seasonal changes of the mass distribution of the Earth caused by water and air flows (Fig. 2.3).

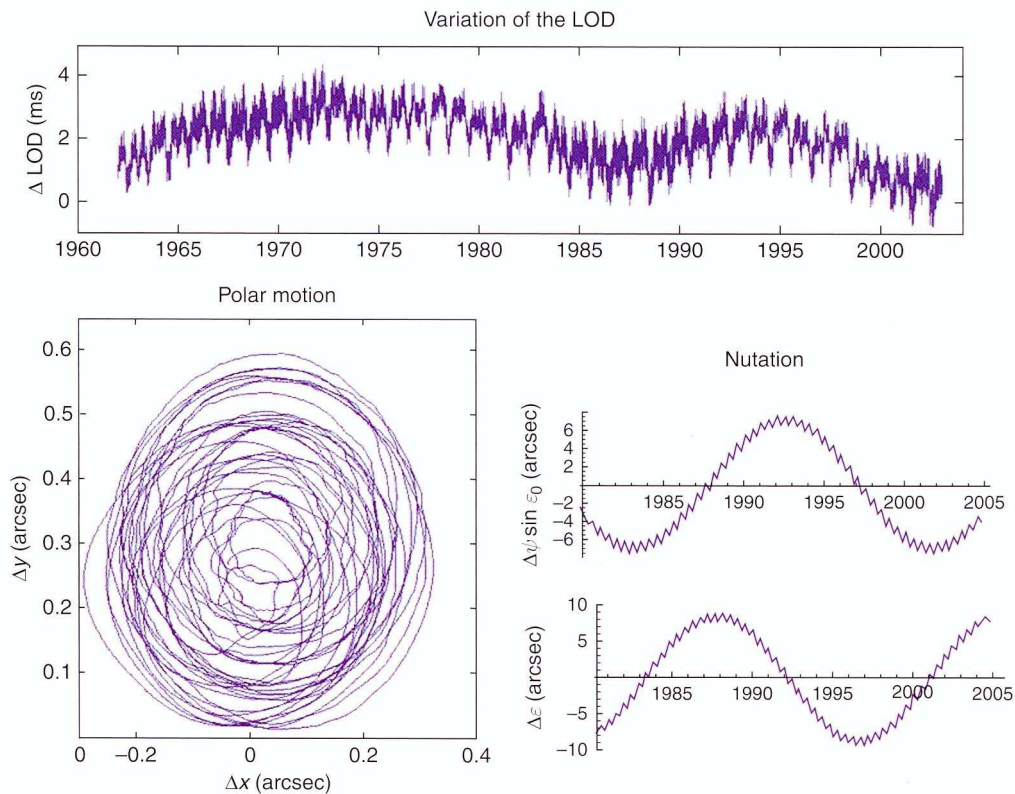


**Figure 2.3:** Variations of the Earth Orientation Parameters (EOPs) (Source: Dehant and Mathews [2007]).

## 2.2 Integration of the equation of motion

The accurate computation of a satellite's orbit accounting for several forces (see section 2.3 and 2.4) can only be obtained by using appropriate numerical methods. A wide range of methods for numerical integration of ordinary differential equations exists. Detailed information is given in *Montenbruck and Gill* [2000], *Vallado* [2001], *Gander* [1985] and *Guthmann* [1994]. In the following the method used in this thesis is described.

The classical Runge-Kutta method, firstly formulated from Carl Runge in 1895 and later from Heun and Kutta improved, is probably the most widely-used method for integration of ordinary differential equations. For the computation of  $\mathbf{x}_{i+1}$  only the previous computed solution  $\mathbf{x}_i$  is needed. This is achieved for a step size  $h_i$  by an approximation with weighted means. The general Runge-Kutta formula can be written in the form

$$\Phi(\mathbf{x}, h) = \sum_{j=1}^s b_j \mathbf{k}_j \quad (2.3)$$

with

$$\mathbf{k}_j = \mathbf{f} \left( \mathbf{x} + h \sum_{l=1}^{j-1} a_{jl} \mathbf{k}_l \right), \quad 1 \leq j \leq s, \quad (2.4)$$

where  $\mathbf{f}$  describes the equation of motion and  $s$  is the stage of the method. Each method is fully described by its coefficients  $a_{jl}$ ,  $b_j$ , which can be written in the following manner

$$\begin{array}{c|cccc} c_1 & 0 & 0 & 0 & 0 \\ c_2 & a_{21} & 0 & 0 & 0 \\ \vdots & \vdots & \ddots & 0 & 0 \\ c_s & a_{s1} & \cdots & a_{s,s-1} & 0 \\ \hline & b_1 & b_2 & \cdots & b_s \end{array}$$

The coefficients are determined such that they satisfy the relations

$$\sum_{i=1}^s b_i = 1 \quad c_j = \sum_{l=1}^{j-1} a_{jl} \quad \text{with} \quad c_1 = 0. \quad (2.5)$$

The accuracy of the method depends on the step size and the computation time on the number of steps to be carried out for computation. Therefore an optimal step size  $h_i$  needs to be found for accurate computations with less computation effort.

In order to estimate the error at every step two approximations with the step size  $h$  and  $\frac{h}{2}$  can be computed and the error according to *Guthmann* [1994] estimated via

$$\delta_i = \frac{\left\| \mathbf{x}_{i+1}^{(1)} - \mathbf{x}_{i+1}^{(2)} \right\|_{\infty}}{h_i (1 - 2^{-p})} + O(h_i^{p+1}). \quad (2.6)$$

The disadvantage of this kind of step size control is the large number of function evaluations. A method with stage  $s$  has to evaluate the function  $\mathbf{f}$  on  $s + 2s - 1 = 3s - 1$  points and this can lead to an extensive computing time. In order to avoid this disadvantage the embedded methods can be used, which use two approximations  $\mathbf{x}_{i+1}^{(1)}$  and  $\mathbf{x}_{i+1}^{(2)}$  of order  $p$  and  $p + 1$ , respectively. The essential feature of embedded methods is, that both approximations are obtained by using the same stages  $\mathbf{k}_j$ , thereby decreasing the computational cost for error estimation dramatically. As approximation for the solution at  $\mathbf{x}_{i+1}$  typically  $\mathbf{x}_{i+1}^{(1)}$  is used for this method while  $\mathbf{x}_{i+1}^{(2)}$  is only used for error estimation. The local error for step size control is

$$\delta_i = \frac{\|\mathbf{x}_{i+1}^{(1)} - \mathbf{x}_{i+1}^{(2)}\|_{\infty}}{h_i} + O(h_i^{p+1}). \quad (2.7)$$

These embedded methods are called Runge-Kutta-Fehlberg pair with order  $p$  and  $p + 1$ , abbreviated *RKF* $p(p+1)$  (*Guthmann* [1994]).

The previously presented methods are using the result of the higher order only for error estimation whereas  $\mathbf{x}_{i+1}^{(1)}$  is used as approximation of  $\mathbf{x}(t_{i+1})$ . *Dormand and Prince* [1981] have developed embedded methods which resolve this disadvantage. As before two approximations  $\mathbf{x}_{i+1}^{(1)}$ ,  $\mathbf{x}_{i+1}^{(2)}$  are computed with methods of order  $p$  and  $q$ , where usually  $q = p + 1$ . The computation is now continued with  $\mathbf{x}_{i+1}^{(2)}$  instead of  $\mathbf{x}_{i+1}^{(1)}$  which leads to a higher accuracy. These method is named *RK* $p(q)$  method. One of the most popular method is the *RK5(4)* method with the tableau defined in table A.5 in the appendix (*Dormand and Prince* [1980]).

The local error estimation via equation (2.7) provides

$$\frac{\mathbf{x}_{i+1}^{(1)} - \mathbf{x}_{i+1}^{(2)}}{h} = -\frac{71}{57600}\mathbf{k}_1 + \frac{71}{16695}\mathbf{k}_3 - \frac{71}{1920}\mathbf{k}_4 + \frac{17253}{339200}\mathbf{k}_5 - \frac{22}{525}\mathbf{k}_6 + \frac{1}{40}\mathbf{k}_7. \quad (2.8)$$

This method of order 5 and stage 7 needs less computing time than conventional Runge-Kutta methods. It is established in practice and often used in celestial mechanics. In this thesis a numerical integration method is needed which provides a high accuracy at small time steps of one second. *Schwinger* [2001] tested different methods for integrating the equation of motion of a spacecraft orbiting a comet with testing scenarios from *Hull et al.* [1972] and found that the *RK5(4)* method provides also high accuracy by using comparably small step sizes. As the prescribed time step in this work is one second, methods with higher order (see *Dormand and Prince* [1981]) would lose their advantages of high accuracy at large step sizes due to the given small step size of one second.

There are more than the above mentioned methods (see *Montenbruck and Gill* [2000], *Vallado* [2001], *Gander* [1985] and *Guthmann* [1994]), but implementing such a method would go beyond the scope of the thesis. It is shown in section 2.5 that the selected and implemented integration method *RK5(4)* provides sufficient accuracy and is adequate for solving the equations of motion for Mars Express (MEX) and Rosetta (ROS).

## 2.3 Gravitational forces acting on a spacecraft

The motion of a spacecraft is changed by the gravitational attraction of the central body the spacecraft is orbiting. The central body can be treated as a point mass or if it is irregular shaped and / or has nonuniform mass distribution the deviation from a point mass has also be taken into account for a precise orbit determination. In addition the gravitational attraction of other bodies needs be incorporated into the force model if the gravitational force of these bodies are significant. The relevant mathematical representations and their numerical realization are summarized in this section.

### 2.3.1 The two-body equation

In order to change the velocity  $\mathbf{v}$  of body with constant mass  $m$  in an inertial frame a force  $\mathbf{F}$  is necessary according to Newton's second law

$$\mathbf{F} = m \frac{d\mathbf{v}}{dt} = m\mathbf{a}, \quad (2.9)$$

where  $\mathbf{a}$  is the acceleration due to the force  $\mathbf{F}$  acting on the body, assuming an ideal inertial reference frame  $\mathbf{I}, \mathbf{J}, \mathbf{K}$  that is fixed in inertial space or has an origin moving with constant velocity. The system of two bodies comprises the central body and a spacecraft with the respective masses  $m_c$  and  $m_{SC}$ . The bodycentric  $\mathbf{X}, \mathbf{Y}, \mathbf{Z}$ -system is displaced from the ideal inertial reference frame  $\mathbf{I}, \mathbf{J}, \mathbf{K}$ , but does not rotate or accelerate with respect to  $\mathbf{I}, \mathbf{J}, \mathbf{K}$  (see Figure 2.4). The force acting on the spacecraft in the bodycentric frame can be written according to Newton's law of gravitation as

$$\mathbf{F}_g = -Gm_cm_{SC} \frac{\mathbf{r}}{|\mathbf{r}|^3}. \quad (2.10)$$

Here  $G$  is the gravitational constant and  $\mathbf{r}$  the vector from the central body to the spacecraft. This equation is valid only if the central body and the spacecraft can be treated as a point mass and no other force acts on the inertial system. Using the position vector of the central body  $\mathbf{r}_c$  and the spacecraft  $\mathbf{r}_{SC}$  with respect to the origin of the  $\mathbf{I}, \mathbf{J}, \mathbf{K}$  reference system a vector from the central body to the spacecraft can be expressed as

$$\mathbf{r} = \mathbf{r}_{SC} - \mathbf{r}_c. \quad (2.11)$$

This equation can be differentiated without considering the derivatives of each axis of the coordinate system due to the fact that the reference system is an inertial system. The acceleration of the spacecraft relative to the center of the central body is then

$$\ddot{\mathbf{r}} = \ddot{\mathbf{r}}_{SC} - \ddot{\mathbf{r}}_c. \quad (2.12)$$

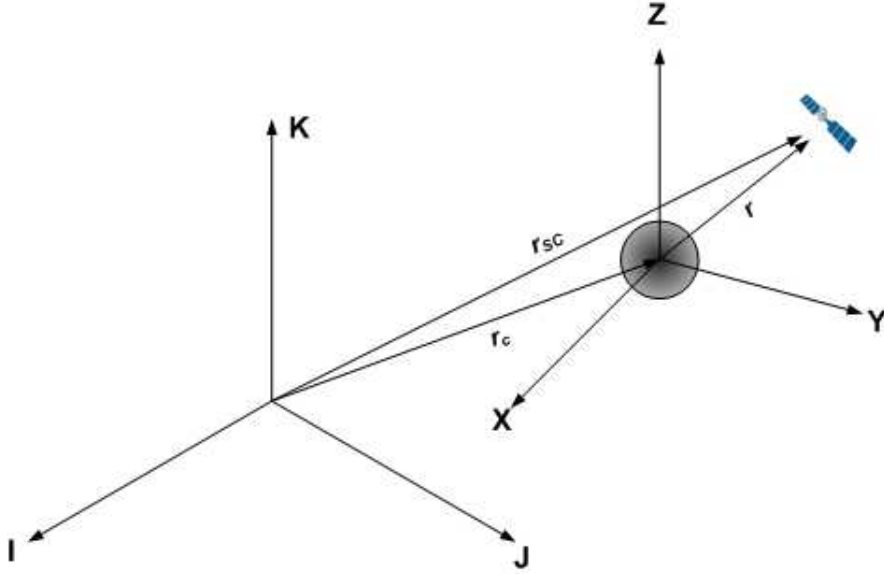


**Figure 2.4:** Geometry for two bodies in an inertial reference frame.  $\mathbf{I}, \mathbf{J}, \mathbf{K}$  is assumed to be an inertial coordinate system.  $\mathbf{X}, \mathbf{Y}, \mathbf{Z}$  is displaced from  $\mathbf{I}, \mathbf{J}, \mathbf{K}$ , but does not rotate or accelerate with respect to  $\mathbf{I}, \mathbf{J}, \mathbf{K}$ .

Newton's second law and his law of gravitation leads to the following expression for the inertial forces:

$$\mathbf{F}_{SC} = m_{SC}\ddot{\mathbf{r}}_{SC} = -Gm_c m_{SC} \frac{\mathbf{r}}{|\mathbf{r}|^3} \quad (2.13)$$

$$\mathbf{F}_c = m_c\ddot{\mathbf{r}}_c = Gm_c m_{SC} \frac{\mathbf{r}}{|\mathbf{r}|^3}. \quad (2.14)$$

The different signs of the gravitational force on the right side of equations (2.13) and (2.14) originate from the opposite direction of the force of the central body and the force of the spacecraft. The relative acceleration  $\ddot{\mathbf{r}}$  can now be written by solving for the individual forces and using equation (2.12).

$$\ddot{\mathbf{r}} = -G(m_c + m_{SC}) \frac{\mathbf{r}}{|\mathbf{r}|^3}. \quad (2.15)$$

Assuming that the mass  $m_{SC}$  of the spacecraft is very small compared to the mass of the central body  $m_c$  and can be neglected, then the two-body equation can be written as

$$\ddot{\mathbf{r}} = -Gm_c \frac{\mathbf{r}}{|\mathbf{r}|^3}. \quad (2.16)$$

This is the basic two-body equation which is an idealized approximation and describes the gravitational forces acting on a satellite precisely if the central body can be treated as a point mass. If the central body is orbited also by a moon like the Earth the perturbation of the orbit by the moon has also be taken into account.

### 2.3.2 The n-body equation

In the case of a spacecraft orbiting a solar system body the gravitational attraction of the Sun and other bodies must also be taken into account. Therefore an equation which comprises more than one body the so called n-body equation is derived based the two-body equation.

Assuming the same requirements as used in section 2.3.1 for the two-body equation but introducing a third body as shown in Figure 2.5. The mass of the central body is denoted by  $m_c$ , the mass of the third body by  $m_3$ , the vector from the central body to the spacecraft by  $\mathbf{r}$ , and the vector from the central body to the third body by  $\mathbf{r}_3$  (see Figure 2.5). The inertial forces on the spacecraft and the central body are then

$$\mathbf{F}_{SC} = m_{SC}\ddot{\mathbf{r}}_{SC} = -Gm_cm_{SC}\frac{\mathbf{r}}{|\mathbf{r}|^3} - Gm_3m_{SC}\frac{\mathbf{r} - \mathbf{r}_3}{|\mathbf{r} - \mathbf{r}_3|^3} \quad (2.17)$$

$$\mathbf{F}_c = m_c\ddot{\mathbf{r}}_c = Gm_cm_{SC}\frac{\mathbf{r}}{|\mathbf{r}|^3} + Gm_cm_3\frac{\mathbf{r}_3}{|\mathbf{r}_3|^3}. \quad (2.18)$$

The acceleration felt by the spacecraft relative to the mass center of the central body is according to equation (2.11)

$$\ddot{\mathbf{r}} = -Gm_c\frac{\mathbf{r}}{|\mathbf{r}|^3} - Gm_3\frac{\mathbf{r} - \mathbf{r}_3}{|\mathbf{r} - \mathbf{r}_3|^3} + Gm_{SC}\frac{\mathbf{r}}{|\mathbf{r}|^3} + Gm_3\frac{\mathbf{r}_3}{|\mathbf{r}_3|^3}, \quad (2.19)$$

Reordering the terms and the assumption that the mass  $m_{SC}$  of the spacecraft is negligible produces

$$\ddot{\mathbf{r}}_3 = -Gm_c\frac{\mathbf{r}}{|\mathbf{r}|^3} - Gm_3\left(\frac{\mathbf{r} - \mathbf{r}_3}{|\mathbf{r} - \mathbf{r}_3|^3} + \frac{\mathbf{r}_3}{|\mathbf{r}_3|^3}\right). \quad (2.20)$$

The first term the two-body acceleration of the spacecraft due to the central body. The left-hand term in the bracket is called the direct effect and represents the acceleration of the third body directly on the satellite. The right-hand term is the acceleration of the third body on the central body and is named consequentially the indirect term. Expanding equation (2.20) to n bodies and leads to the n-body equation

$$\ddot{\mathbf{r}} = -Gm_c\frac{\mathbf{r}}{|\mathbf{r}|^3} - \sum_{i=1}^n Gm_i\left(\frac{\mathbf{r} - \mathbf{r}_i}{|\mathbf{r} - \mathbf{r}_i|^3} + \frac{\mathbf{r}_i}{|\mathbf{r}_i|^3}\right). \quad (2.21)$$

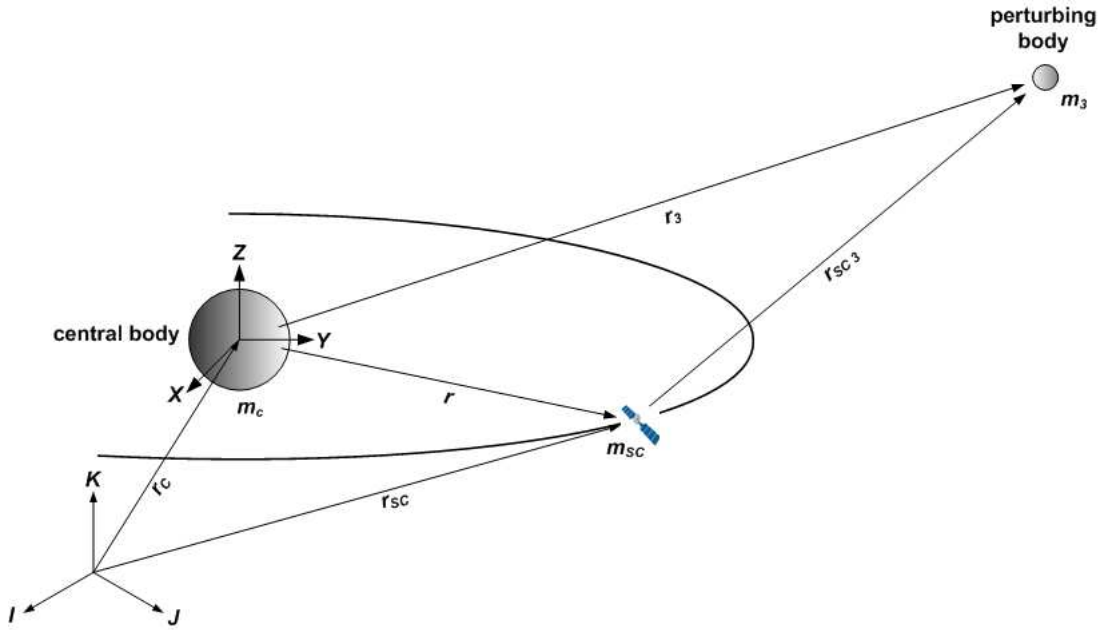


**Figure 2.5:** Geometry of the three-body problem in an inertial reference frame  $I, J, K$ .

### 2.3.3 Sphere of influence

In equation (2.21) the central body represents the body with the highest gravitational attraction on the spacecraft. Sometimes it is not clear which is the body with the highest gravitational attraction regarding the mass of the bodies and distance from each other. But wrong selection of the central body would lead to inaccurate orbit determination.

This problem can be solved with the concept of the sphere of influence. The sphere of influence for a central body is an imaginary sphere within the gravity of the object is primarily responsible for all orbital motion. Outside this sphere, other bodies influence most of the spacecrafts motion.

Assuming three bodies with masses  $m_1$ ,  $m_2$  and  $m_3$  (Fig. 2.6),  $m_1$  is the central body,  $m_2$  the spacecraft, and  $m_3$  the perturbing body, the equation of motion can be written according to equation (2.21)

$$\ddot{\mathbf{r}}_{12} + G(m_1 + m_2) \frac{\mathbf{r}_{12}}{r_{12}^3} = -Gm_3 \left( \frac{\mathbf{r}_{13}}{r_{13}^3} + \frac{\mathbf{r}_{32}}{r_{32}^3} \right). \quad (2.22)$$

If the central body is  $m_3$  and  $m_1$  the perturbing body the equation of motion is accordingly

$$\ddot{\mathbf{r}}_{32} + G(m_3 + m_2) \frac{\mathbf{r}_{32}}{r_{32}^3} = -Gm_1 \left( \frac{\mathbf{r}_{12}}{r_{12}^3} - \frac{\mathbf{r}_{13}}{r_{13}^3} \right). \quad (2.23)$$

From this equations it can be distinguished, by the ratio of the disturbing force (right hand side of the equations) to the corresponding central attraction (left hand side), which of the equations has to be used. Whichever provides the smaller ratio is the one to be preferred.

The surface boundary over which these two ratios are equal is almost spherical if  $r_{12} \ll r_{13}$ . Equating both ratios and assuming that  $m_3 \ll m_1$  and  $m_1 \gg m_2$  the sphere of influence about  $m_1$  is approximately

$$\frac{r_{12}}{r_{13}} = \left( \frac{m_1}{m_3} \right)^{\frac{2}{5}}. \quad (2.24)$$

This equation describes a sphere about  $m_1$  on the boundary of which the ratio of disturbing to primary accelerations is the same for both equations (2.22) and (2.23). Inside the sphere the motion of  $m_2$  relative to  $m_1$  should be computed and outside  $m_3$  should be treated as the central body. A table of the sphere of influence for the planets with respect to the Sun can be found in *Battin* [1987], page 397 or in *Häusler* [2008c].

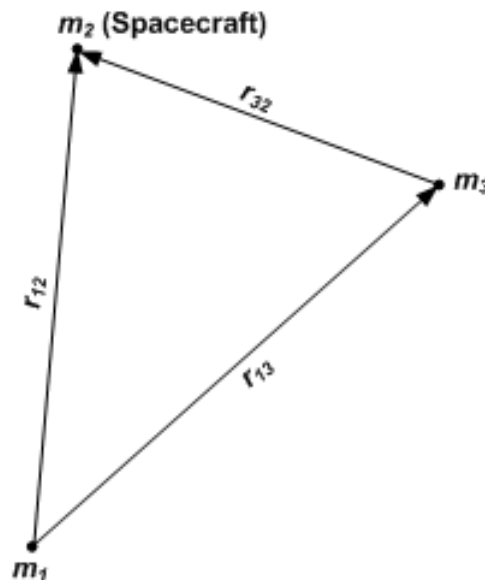


**Figure 2.6:** Sphere of influence (Source: Häusler [2008c], changed).

### 2.3.4 The gravity potential of a body

In the previous sections the equation of motion for a satellite orbiting a central body was developed based on the assumption that all bodies can be treated as point masses. However this is in most cases not true for practical purposes. Mars for instance consists of large volcanoes but also of valleys and this leads to a gravity field strongly deviating from a point mass representation. In the following the gravity potential of a body with non-spherical shape and a nonuniform density distribution is derived. In addition, a numerical implementation is developed with which the acceleration felt by satellite orbiting around such a body can be computed precisely.

The acceleration of a body according to equation (2.16) can also be written using a potential  $U$  in the form

$$\ddot{\mathbf{r}} = -\text{grad}(U) \quad \text{with} \quad U = Gm_c \frac{1}{r}. \quad (2.25)$$

The mass of a body can be expressed by the sum of a large but finite number of very small mass elements  $dm$ . The summation of each mass element over the entire body results in the potential of a body with arbitrary shape and density distribution

$$U(\mathbf{r}) = G \iiint_{Vol} \frac{\rho(\mathbf{s})}{|\mathbf{r} - \mathbf{s}|} dV, \quad (2.26)$$

where  $\mathbf{r}$  is the position vector of the point in which the potential is determined and  $\mathbf{s}$  the position vector of the infinitesimal mass  $dm$  of the body (Fig. 2.7), which are expressed using the individual density and volume of the specific mass element

$$dm = \rho(\mathbf{s})dV \quad (2.27)$$

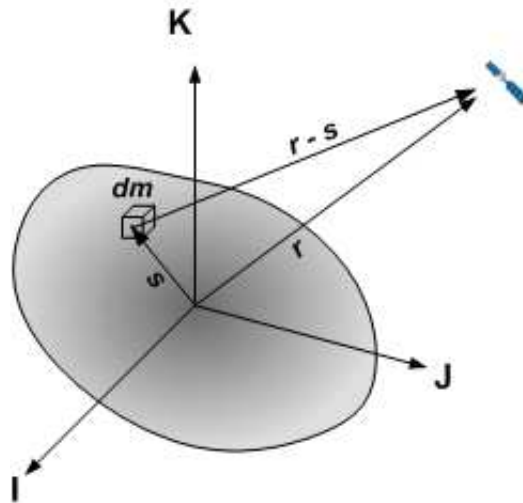


**Figure 2.7:** Contribution of a small mass element to the gravity potential of a body.

### 2.3.4.1 Expansion of the gravity potential in spherical harmonics

In order to determine the gravity potential of an irregular shaped body using equation (2.26) the inverse of the distance  $|\mathbf{r} - \mathbf{s}|$  can be expanded in a series of Legendre polynomials. For this purpose the origin of the coordinate system has to align with the center of mass and a reference radius is selected which fulfills the condition  $\bar{R} := \max\{|\mathbf{s}| \mid \mathbf{s} \in Vol\}$ .  $\bar{R}$  describes a sphere enclosing the body and  $\mathbf{r}$  lies outside of the body if  $|\mathbf{r}| > \bar{R}$  for all points, so that

$$\frac{1}{|\mathbf{r} - \mathbf{s}|} = \frac{1}{r} \sum_{n=0}^{\infty} \left(\frac{s}{r}\right)^n P_n(\cos \gamma) \quad \text{with} \quad \cos \gamma = \frac{\mathbf{r} \cdot \mathbf{s}}{r s}, \quad (2.28)$$

where  $\gamma$  is the angle between  $\mathbf{r}$  and  $\mathbf{s}$ , and

$$P_n(x) = \frac{1}{2^n n!} \frac{d^n}{dx^n} (x^2 - 1)^n \quad (2.29)$$

is the Legendre polynomial or zonal spherical harmonics of degree  $n$ . Introducing spherical coordinates, i.e. radius  $r$ , latitude  $\phi$  and longitude  $\lambda$  of the point  $\mathbf{r}$  and analogue  $r'$ ,  $\phi'$ ,  $\lambda'$  of  $\mathbf{s}$ , the addition theorem of Legendre polynomials (*Kautzleben* [1965])

$$P_n(\cos \gamma) = \sum_{m=0}^n (2 - \delta_{0,m}) \frac{(n-m)!}{(n+m)!} P_{n,m}(\cos \phi) P_{n,m}(\cos \phi') \cos m(\lambda - \lambda') \quad (2.30)$$

can be used, where  $\delta_{0,m}$  is the Kronecker delta symbol and  $P_{n,m}(x)$  are the associated Legendre polynomials of degree  $n$  and order  $m$  which are defined by

$$P_{n,m}(x) = (1 - x^2)^{(m/2)} \frac{d^m P_n(x)}{dx^m}. \quad (2.31)$$

This formulation is inefficient for practical computation. A more efficient way to calculate these functions can be accomplished by recursion. This method is described in detail in *Press et al.* [1986] or *Vallado* [2001].

Inserting the associated Legendre polynomial and equation (2.28) into equation (2.26) the gravity potential of non-spherical body can be written as

$$U = \frac{Gm_c}{r} \sum_{n=0}^{\infty} \sum_{m=0}^n \left(\frac{\bar{R}}{r}\right)^n P_{n,m}(\cos \phi) (C_{n,m} \cos m\lambda + S_{n,m} \sin m\lambda) \quad (2.32)$$

$$= \frac{Gm_c}{r} \sum_{n=0}^{\infty} \sum_{m=0}^n \left(\frac{\bar{R}}{r}\right)^n (C_n^m(\phi, \lambda) C_{n,m} + S_n^m(\phi, \lambda) S_{n,m}), \quad (2.33)$$

where the  $C_{n,m}$  and  $S_{n,m}$  are the gravitational coefficients defined as

$$C_{n,m} = \frac{2 - \delta_{0,m}}{m_c} \frac{(n-m)!}{(n+m)!} \iiint_{Vol} \left(\frac{s}{R}\right)^n P_{n,m}(\cos \phi') \cos(m\lambda') \rho(r', \phi', \lambda') dV \quad (2.34a)$$

$$S_{n,m} = \frac{2 - \delta_{0,m}}{m_c} \frac{(n-m)!}{(n+m)!} \iiint_{Vol} \left(\frac{s}{R}\right)^n P_{n,m}(\cos \phi') \sin(m\lambda') \rho(r', \phi', \lambda') dV. \quad (2.34b)$$

These coefficients describe the dependence of internal mass distributions within the body and are used for precise orbit determination around a non-spherical body.

The  $C_n^m(\phi, \lambda)$  and  $S_n^m(\phi, \lambda)$  in equation (2.33) are called spherical harmonics and determine lines on a sphere by the indices  $n$  and  $m$  along which the functions vanish. The spherical harmonics can be divided into three different types (see Figure 2.8): zonal, sectorial and tesseral harmonics.

*Zonal harmonics* are characterized by the fact that the index  $m$  equals zero. Therefore the potential is no longer depending on the longitude  $\lambda$ . The potential is symmetric along the pole axis. The sphere is divided in  $n + 1$  bands of latitude, in which the potential is alternately increasing (+) and decreasing (-), i.e. every root of the zonal harmonics indicates a transition between negative and positive values (Fig. 2.8(a)).

*Sectorial harmonics* are defined by  $n = m$ . and displaying bands of longitude on the sphere as it can be seen in figure 2.8(b). The Legendre polynomials  $P_{n,n}$  are only zero at the poles in this case. In addition the term  $(\sin(n\lambda) + \cos(n\lambda))$  vanishes also for  $2n$  different values of  $\lambda$ . Therefore, the line along which the spherical harmonics  $C_n^m(\phi, \lambda)$  and  $S_n^m(\phi, \lambda)$  equal zero indicates meridians which divide the sphere in  $2n$  sectors. Every sector indicates  $n$  positive (+) and  $n$  negative mass concentrations.

If  $n \neq 0$  and  $m \neq 0$  then specific regions of the body are represented and these functions are called *tesseral harmonics*. The sphere is divided into the form of a checkerboard as shown in Figure 2.8(c) (Vallado [2001]).

### 2.3.4.2 Gravitational coefficients

The gravitational coefficients from equations (2.34a) and (2.34b) serve as weighting factors in the expansion of the potential of a body with nonuniform mass distribution. As the origin of the coordinate system is aligned with the center of mass, some of the low-degree and order coefficients can be simplified in the following form.

- If  $m = 0$  and  $n = 0$  then from equation (2.34a) it can be derived that

$$C_{0,0} = \frac{1}{m_c} \iiint_{Vol} \rho(\mathbf{s}) dV = 1. \quad (2.35)$$

- If  $m = 0$  then the term  $\sin(m\lambda')$  equals zero and therefore

$$S_{n,0} = 0 \quad \text{for all } n. \quad (2.36)$$

- The following gravity coefficients are vanishing.

$$C_{1,0} = \frac{1}{m_c \bar{R}} \iiint_{\text{Vol}} s \cos \theta' \rho(\mathbf{s}) dV \quad (2.37)$$

$$= \frac{1}{m_c \bar{R}} \iiint_{\text{Vol}} z' \rho(\mathbf{s}) dV$$

$$= \frac{\bar{z}}{\bar{R}}$$

$$C_{1,1} = \frac{\bar{x}}{\bar{R}} \quad (2.38)$$

$$S_{1,1} = \frac{\bar{y}}{\bar{R}}, \quad (2.39)$$

where  $\bar{x}$ ,  $\bar{y}$ ,  $\bar{z}$  are the coordinates of the center of mass defined by

$$\bar{\mathbf{r}} = \begin{pmatrix} \bar{x} \\ \bar{y} \\ \bar{z} \end{pmatrix} = \frac{1}{m_c} \int \mathbf{s} \rho(\mathbf{s}) d^3 \mathbf{s}. \quad (2.40)$$

- If the axis of the coordinate system are selected in the way that they are aligned with the main axis of inertia, i.e. the off-diagonal elements of the inertia tensor  $I_{xy}$ ,  $I_{yz}$  and  $I_{xz}$  vanish then

$$C_{2,1} = \frac{2}{6m_c \bar{R}^2} \iiint_{\text{Vol}} 3 \cos \theta' \sin \theta' \cos \phi' \rho(\mathbf{s}) dV \quad (2.41)$$

$$= \frac{1}{m_c \bar{R}^2} \iiint_{\text{Vol}} xz \rho(\mathbf{s}) dV$$

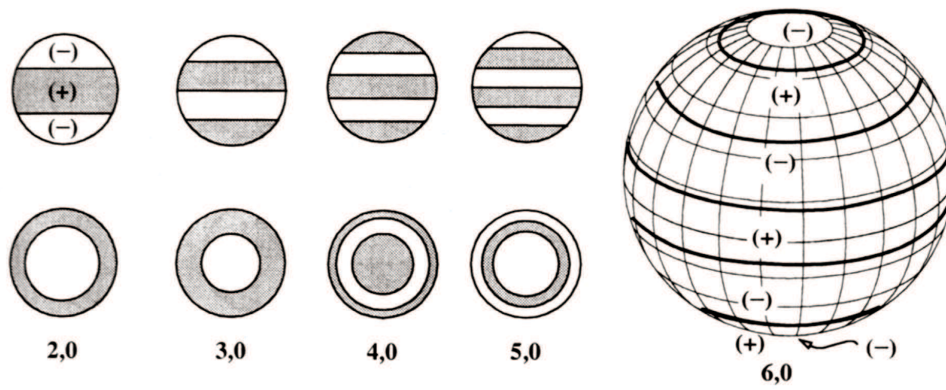
$$= -\frac{I_{xz}}{m_c \bar{R}^2} = 0$$

and accordingly:

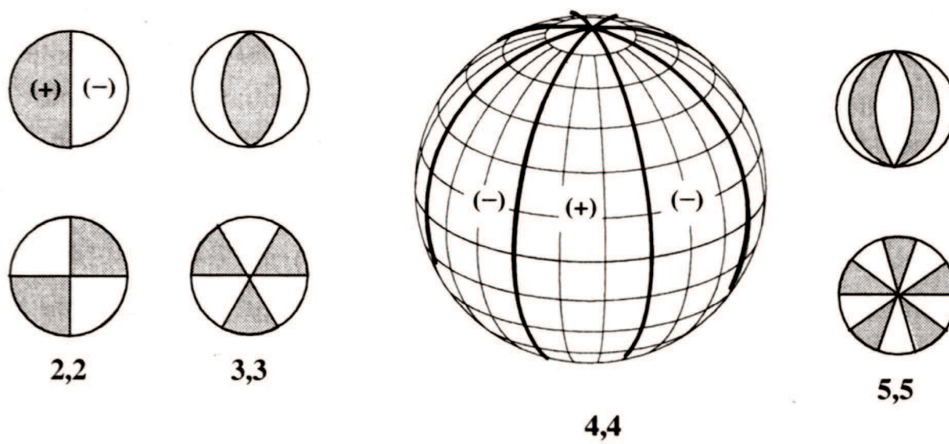
$$S_{2,1} = -\frac{I_{yz}}{M \bar{R}^2} = 0 \quad (2.42)$$

$$S_{2,2} = -\frac{I_{xy}}{2M \bar{R}^2} = 0. \quad (2.43)$$

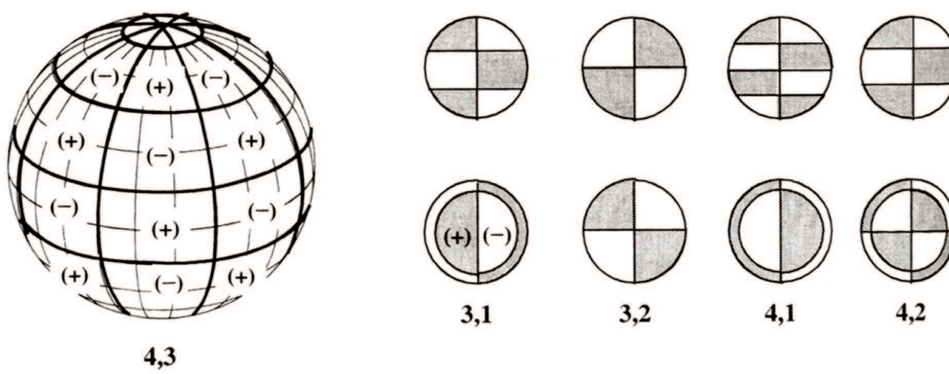
Therefore the lowest order gravitational coefficients, which are not vanishing, are  $C_{2,0}$  and  $C_{2,2}$ , if the coordinate system is well selected. The coefficient  $C_{2,0}$  represents the flattening of the body, i.e. the difference between the polar and the equatorial diameter and is for example the largest coefficient for the Earth's gravity potential, being three orders of magnitude larger than  $C_{3,0}$ , which accounts for bulb-like shape of the Earth.



(a) Zonal harmonics



(b) Sectorial harmonics



(c) Tesseral harmonics

**Figure 2.8:** Spherical harmonics (Source: Vallado [2001], changed)

### 2.3.4.3 Normalization

The gravitational coefficients may differ over a range of ten or more orders of magnitude. Therefore, normalized coefficients are used in practice which are much more uniform and provide higher accuracy for gravity potential computation. The normalization is defined as

$$\Pi_{n,m} = \sqrt{\frac{(n+m)!}{(2-\delta_{0,m})(n-m)!(2n+1)}}. \quad (2.44)$$

Thus the normalized coefficients of the expansion are

$$\begin{Bmatrix} \bar{C}_{n,m} \\ \bar{S}_{n,m} \end{Bmatrix} = \Pi_{n,m} \begin{Bmatrix} C_{n,m} \\ S_{n,m} \end{Bmatrix}. \quad (2.45)$$

And the normalized associated Legendre polynomials are

$$\bar{P}_{n,m} = \frac{P_{n,m}}{\Pi_{n,m}}. \quad (2.46)$$

Obviously, the product of the unnormalized Legendre polynomials and the unnormalized coefficients is equal to the product of the normalized Legendre polynomials and the normalized coefficients, i.e.

$$\bar{C}_{n,m}\bar{P}_{n,m} = C_{n,m}P_{n,m} \quad \text{and} \quad \bar{S}_{n,m}\bar{P}_{n,m} = S_{n,m}P_{n,m} \quad (2.47)$$

Equation (2.44) defines the normalization coefficients most commonly used in geophysical science. Most published gravitational coefficients are based on this normalization, although other definitions of normalization factors do exist (see *Kautzleben* [1965]).

### 2.3.4.4 Time varying gravitational coefficients

In the previous section the central body was treated as a point mass or as a rigid body with an irregular shape and therefore a nonuniform gravity potential. However, no solar system body is perfectly rigid and thus subjected to time varying deformations due to tidal forces.

These forces are caused by the difference in gravitational attraction and centrifugal forces, i.e. the difference in the attraction at points inside and outside the central body experiencing by the gravitational attraction of an orbiting body. The impact of the relative small difference forces is significant. The major part of the attraction is compensated by the centrifugal force arising by orbiting around the barycenter of the two bodies. But the centrifugal force has the same amplitude and direction at all locations because all points of the central body are describing congruent orbits. Therefore it only compensates the gravitational force at the center of mass of the

central body and all other points experience a differential force, which is called tidal force (*Kertz [1995], Agnew [2007]*).

In the case of the Earth, the tidal forces of the Moon and the Sun acting on the Earth result in a small time varying deformation of the solid body of the Earth. The oceans also respond to the gravitational attraction of the Moon and the Sun and the effect is called ocean tides. Therefore the Earth's gravity field is not constant in time but shows small periodic changes. These small variations in the gravity field also effect the motion of a spacecraft. In the case of Mars only the gravity field of the Sun distorts the shape of Mars.

The change in the gravity coefficients of a central body due to solid tides of can be written according to *McCarthy and Petit [2003]*:

$$\begin{Bmatrix} \Delta C_{n,m} \\ \Delta S_{n,m} \end{Bmatrix} = \frac{k_{n,m}}{2n+1} \sum_{i=1}^l \frac{m_j}{m_c} \left( \frac{\bar{R}}{r_i} \right)^{n+1} \bar{P}_{n,m}(\sin(\phi_i)) \begin{Bmatrix} \cos(m\lambda_i) \\ \sin(m\lambda_i) \end{Bmatrix} \quad (2.48)$$

where  $k_{n,m}$  are the nominal Love numbers of degree  $n$  and order  $m$ ,  $m_i$  is the mass of the disturbing body like moon or sun in the case of the Earth,  $m_c$  the mass of the central body,  $\bar{R}$  the equatorial radius of the central body,  $r_i$  the distance from the center of the central body to the disturbing one,  $\phi_i$  is the body-fixed latitude and  $\lambda$  the body-fixed longitude of the disturbing body and  $\bar{P}_{n,m}$  the normalized associated Legendre polynomials. The variation of the largest gravity coefficients  $\bar{C}_{2,0}$  and  $\bar{C}_{3,0}$  can than be computed via

$$\Delta \bar{C}_{2,0} = \frac{k_{2,0}}{2\sqrt{5}} \sum_{i=1}^l \frac{m_j}{m_c} \left( \frac{\bar{R}}{r_i} \right)^3 (3 \sin^2(\phi_i) - 1) \quad (2.49)$$

$$\Delta \bar{C}_{3,0} = \frac{k_{3,0}}{2\sqrt{7}} \sum_{i=1}^l \frac{m_j}{m_c} \left( \frac{\bar{R}}{r_i} \right)^4 (5 \sin^3(\phi_i) - 3 \sin(\phi_i)) \quad (2.50)$$

Another effect resulting from the tidal deformations is a change in position of a ground station located on the surface of the Earth. Detailed information on this effect will be given in section 2.6.2.

### 2.3.5 Numerical computation of the gravitational acceleration of an irregular shaped body

Computing the gradient of the gravity potential of an irregular shaped body according to equation (2.32) is quite time consuming. Therefore an optimized algorithm is useful to save time in repetitive calculation. *Cunningham [1970]* formulated a recursion algorithm and *Montenbruck and Gill [2000]* adopted it (a detailed description can be found in appendix A.4). This algorithm is suitable for a direct computation of the acceleration felt by spacecraft in a body-fixed frame. It uses unnormalized gravitational coefficients

$C_{n,m}$  and  $S_{n,m}$ , which makes the algorithm numerical inaccurate due to the small size of the unnormalized gravitational coefficients of high degree  $n$  and order  $m$ . This algorithm is modified in this thesis for use with normalized gravitational coefficients  $\bar{C}_{n,m}$  and  $\bar{S}_{n,m}$  ensuring high accuracy of the computed acceleration. The modification of the algorithm is explained in the following.

The gravity potential of a irregular shaped body using normalized gravitational coefficients  $\bar{C}_{n,m}$  and  $\bar{S}_{n,m}$  is analogue defined to the definition in *Montenbruck and Gill* [2000]

$$U = \frac{GM}{\bar{R}} \sum_{n=0}^{\infty} \sum_{m=0}^n (\bar{C}_{n,m} \bar{V}_{n,m} + \bar{S}_{n,m} \bar{W}_{n,m}) , \quad (2.51)$$

with the normalized recursion coefficients

$$\bar{V}_{n,m} = \left(\frac{\bar{R}}{r}\right)^{n+1} \bar{P}_{n,m}(\sin \phi) \cos(m\lambda) \quad (2.52a)$$

$$\bar{W}_{n,m} = \left(\frac{\bar{R}}{r}\right)^{n+1} \bar{P}_{n,m}(\sin \phi) \sin(m\lambda) , \quad (2.52b)$$

and the radius  $r$ , the latitude  $\phi$ , the longitude  $\lambda$  of the point  $\mathbf{r}$ , and the reference radius  $\bar{R}$  as defined in section 2.3.4.1.

The relation between normalized and unnormalized gravity coefficients and Legendre polynomials is

$$\bar{C}_{n,m} \bar{P}_{n,m} = C_{n,m} P_{n,m} \quad \text{and} \quad \bar{S}_{n,m} \bar{P}_{n,m} = S_{n,m} P_{n,m} . \quad (2.53)$$

In order to normalize the Legendre polynomials the following normalization factor (see section 2.3.4.3) is used

$$\Pi_{n,m} = \sqrt{\frac{(2 - \delta_{0,m}) (n - m)! (2n + 1)}{(n + m)!}} . \quad (2.54)$$

In recursion algorithms the current result is computed from previous ones like

$$P_{n,m} = P_{n-i, m-j} (\dots) \quad \text{with } i, j \in \mathbb{N} . \quad (2.55)$$

Therefore, the normalized recurrence coefficients can be computed based on the algorithm in *Montenbruck and Gill* [2000] using a compensation factor  $X_{n,m}^{(i,j)}$  which satisfies the following relation using the normalization factor defined in equation (2.44) and the relation between normalized and unnormalized gravitational coefficients and Legendre polynomials from equation (2.47)

$$\Pi_{n,m} P_{n,m} = X_{n,m}^{(i,j)} \Pi_{n+i, m+j} P_{n+i, m+j} (\dots) . \quad (2.56)$$

This yields for the compensation factor

$$X_{n,m}^{(i,j)} = \frac{\Pi_{n,m}}{\Pi_{n+i,m+j}}. \quad (2.57)$$

Initial conditions for the recurrence coefficients are according to *Montenbruck and Gill* [2000]

$$\bar{V}_{0,0} = \frac{\bar{R}}{r} \quad \text{and} \quad \bar{W}_{0,0} = 0 \quad (2.58)$$

In order to compute the recurrence coefficients  $\bar{V}_{m,n}$  and  $\bar{W}_{n,m}$  the following compensation factors are needed.

$$X_{m,m}^{(-1,-1)} \stackrel{m \geq 0}{=} \frac{\Pi_{m,m}}{\Pi_{m-1,m-1}} = \frac{1}{2m-1} \sqrt{\frac{(2m+1)}{(2-\delta_{0,m-1})m}} \quad (2.59)$$

$$X_{n,m}^{(-1,0)} = \frac{\Pi_{n,m}}{\Pi_{n-1,m}} = \sqrt{\frac{(2n+1)(n-m)}{(n+m)(2n-1)}} \quad (2.60)$$

$$X_{n,m}^{(-2,0)} = \frac{\Pi_{n,m}}{\Pi_{n-2,m}} = \sqrt{\frac{(2n+1)(n-m)(n-m-1)}{(n+m)(n+m-1)(2n-3)}} \quad (2.61)$$

With these compensation factors  $X_{n,m}^{(i,j)}$  the normalized recurrence coefficients are

$$\begin{aligned} \bar{V}_{m,m} &\stackrel{m \geq 0}{=} \frac{\bar{R}}{r^2} X_{m,m}^{(-1,-1)} (2m-1) (x \bar{V}_{m-1,m-1} - y \bar{W}_{m-1,m-1}) \\ &= \frac{\bar{R}}{r^2} \sqrt{\frac{2m+1}{(2-\delta_{0,m-1})m}} (x \bar{V}_{m-1,m-1} - y \bar{W}_{m-1,m-1}) \end{aligned} \quad (2.62a)$$

$$\begin{aligned} \bar{W}_{m,m} &\stackrel{m \geq 0}{=} \frac{\bar{R}}{r^2} X_{m,m}^{(-1,-1)} (2m-1) (x \bar{W}_{m-1,m-1} + y \bar{V}_{m-1,m-1}) \\ &= \frac{\bar{R}}{r^2} \sqrt{\frac{2m+1}{(2-\delta_{0,m-1})m}} (x \bar{W}_{m-1,m-1} + y \bar{V}_{m-1,m-1}) \end{aligned} \quad (2.62b)$$

$$\begin{aligned} \bar{V}_{n,m} &= \frac{\bar{R}}{r^2} \frac{1}{(n-m)} \left( X_{n,m}^{(-1,0)} (2n-1) z \bar{V}_{n-1,m} \right. \\ &\quad \left. - X_{n,m}^{(-2,0)} (n+m-1) \bar{R} \bar{V}_{n-2,m} \right) \\ &= \frac{\bar{R}}{r^2} \sqrt{\frac{2n+1}{(n+m)(n-m)}} \left( \sqrt{2n-1} z \bar{V}_{n-1,m} \right. \\ &\quad \left. - \sqrt{\frac{(n+m-1)(n-m-1)}{2n-3}} \bar{R} \bar{V}_{n-2,m} \right) \end{aligned} \quad (2.62c)$$

$$\begin{aligned}
\overline{W}_{n,m} &= \frac{\overline{R}}{r^2} \frac{1}{(n-m)} \left( X_{n,m}^{(-1,0)} (2n-1) z \overline{W}_{n-1,m} \right. \\
&\quad \left. - X_{n,m}^{(-2,0)} (n+m-1) \overline{R} \overline{W}_{n-2,m} \right) \\
&= \frac{\overline{R}}{r^2} \sqrt{\frac{2n+1}{(n+m)(n-m)}} \left( \sqrt{2n-1} z \overline{W}_{n-1,m} \right. \\
&\quad \left. - \sqrt{\frac{(n+m-1)(n-m-1)}{2n-3}} \overline{R} \overline{W}_{n-2,m} \right) \quad (2.62d)
\end{aligned}$$

In order to compute the acceleration from normalized gravitational coefficients a compensation factor must be implemented as a moderator between the normalized gravity coefficients  $\overline{C}_{n,m}$ ,  $\overline{S}_{n,m}$  and the normalized recurrence coefficients  $\overline{V}_{n,m}$ ,  $\overline{W}_{n,m}$ , because they are multiplied with different degree and order. Therefore the following condition has to be complied with

$$\begin{aligned}
C_{n,m} P_{n+i,m+j} &= \frac{1}{\Pi_{n,m}} C_{n,m} X_{n,m}^{(i,j)} \Pi_{n+i,m+j} P_{n+i,m+j} \\
&= \overline{C}_{n,m} X_{n,m}^{(i,j)} \overline{P}_{n+i,m+j} \quad (2.63)
\end{aligned}$$

Hence, the compensation factor for the acceleration is equally defined as for the recursion coefficients in equation (2.57).

The specific compensation factors necessary for further computations can be derived as follows

$$X_{n,0}^{(1,1)} = \frac{\Pi_{n,0}}{\Pi_{n+1,1}} = \sqrt{\frac{(2n+1)(n+1)(n+2)}{2(2n+3)}} \quad (2.64)$$

$$X_{n,0}^{(1,0)} = \frac{\Pi_{n,0}}{\Pi_{n+1,0}} = \sqrt{\frac{2n+1}{2n+3}} \quad (2.65)$$

$$X_{n,m}^{(1,1)} \stackrel{m \geq 0}{=} \frac{\Pi_{n,m}}{\Pi_{n+1,m+1}} = \sqrt{\frac{(2n+1)(n+m+2)(n+m+1)}{2n+3}} \quad (2.66)$$

$$X_{n,m}^{(1,-1)} \stackrel{m \geq 0}{=} \frac{\Pi_{n,m}}{\Pi_{n+1,m-1}} = \sqrt{\frac{2(2n+1)}{(n-m+2)(n-m+1)(2-\delta_{0,m-1})(2n+3)}} \quad (2.67)$$

$$X_{n,m}^{(1,0)} \stackrel{m \geq 0}{=} \frac{\Pi_{n,m}}{\Pi_{n+1,m}} = \sqrt{\frac{(2n+1)(n+m+1)}{(n-m+1)(2n+3)}}. \quad (2.68)$$

The partial accelerations calculated with normalized coefficients are then given by

$$\begin{aligned}
\ddot{x}_{n,0} &= -\frac{GM}{\overline{R}^2} \overline{C}_{n,0} X_{n,0}^{(1,1)} \overline{V}_{n+1,1} \\
&= -\frac{GM}{\overline{R}^2} \sqrt{\frac{(2n+1)(n+1)(n+2)}{2(2n+3)}} (\overline{C}_{n,0} \overline{V}_{n+1,1}) \quad (2.69a)
\end{aligned}$$

$$\begin{aligned}
\ddot{x}_{n,m} &\stackrel{m \geq 0}{=} -\frac{1}{2} \frac{GM}{R^2} \left( \overline{C}_{n,m} X_{n,m}^{(1,1)} \overline{V}_{n+1,m+1} + \overline{S}_{n,m} X_{n,m}^{(1,1)} \overline{W}_{n+1,m+1} \right. \\
&\quad - (n-m+2)(n-m+1) \left( \overline{C}_{n,m} X_{n,m}^{(1,-1)} \overline{V}_{n+1,m-1} \right. \\
&\quad \left. \left. + \overline{S}_{n,m} X_{n,m}^{(1,-1)} \overline{W}_{n+1,m-1} \right) \right) \\
&= -\frac{1}{2} \frac{GM}{R^2} \sqrt{\frac{2n+1}{2n+3}} \left( \sqrt{(n+m+2)(n+m+1)} \left( \overline{C}_{n,m} \overline{V}_{n+1,m+1} \right. \right. \\
&\quad \left. \left. + \overline{S}_{n,m} \overline{W}_{n+1,m+1} \right) - \sqrt{\frac{2(n-m+2)(n-m+1)}{2-\delta_{0,m-1}}} \right. \\
&\quad \left. \left( \overline{C}_{n,m} \overline{V}_{n+1,m-1} + \overline{S}_{n,m} \overline{W}_{n+1,m-1} \right) \right) \tag{2.69b}
\end{aligned}$$

$$\begin{aligned}
\ddot{y}_{n,0} &= -\frac{GM}{R^2} \overline{C}_{n,0} X_{n,0}^{(1,1)} \overline{W}_{n+1,1} = \\
&= -\frac{GM}{R^2} \sqrt{\frac{(2n+1)(n+1)(n+2)}{2(2n+3)}} \left( \overline{C}_{n,0} \overline{W}_{n+1,1} \right) \tag{2.70a}
\end{aligned}$$

$$\begin{aligned}
\ddot{y}_{n,m} &\stackrel{m \geq 0}{=} -\frac{1}{2} \frac{GM}{R^2} \left( \overline{C}_{n,m} X_{n,m}^{(1,1)} \overline{W}_{n+1,m+1} - \overline{S}_{n,m} X_{n,m}^{(1,1)} \overline{V}_{n+1,m+1} \right. \\
&\quad \left. + (n-m+2)(n-m+1) \left( \overline{C}_{n,m} X_{n,m}^{(1,-1)} \overline{W}_{n+1,m-1} \right. \right. \\
&\quad \left. \left. - \overline{S}_{n,m} X_{n,m}^{(1,-1)} \overline{V}_{n+1,m-1} \right) \right) \\
&= -\frac{1}{2} \frac{GM}{R^2} \sqrt{\frac{2n+1}{2n+3}} \left( \sqrt{(n+m+2)(n+m+1)} \left( \overline{C}_{n,m} \overline{W}_{n+1,m+1} \right. \right. \\
&\quad \left. \left. - \overline{S}_{n,m} \overline{V}_{n+1,m+1} \right) + \sqrt{\frac{2(n-m+2)(n-m+1)}{2-\delta_{0,m-1}}} \right. \\
&\quad \left. \left( \overline{C}_{n,m} \overline{W}_{n+1,m-1} - \overline{S}_{n,m} \overline{V}_{n+1,m-1} \right) \right) \tag{2.70b}
\end{aligned}$$

$$\begin{aligned}
\ddot{z}_{n,0} &= -\frac{GM}{R^2} (n+1) \overline{C}_{n,0} X_{n,0}^{(1,0)} \overline{V}_{n+1,0} = \\
&= -\frac{GM}{R^2} (n+1) \sqrt{\frac{(2n+1)}{(2n+3)}} \overline{C}_{n,0} \overline{V}_{n+1,0} \tag{2.71a}
\end{aligned}$$

$$\begin{aligned}
\ddot{z}_{n,m} &\stackrel{m \geq 0}{=} -\frac{GM}{R^2} (n-m+1) X_{n,m}^{(1,0)} \left( \overline{C}_{n,m} \overline{V}_{n+1,m} + \overline{S}_{n,m} \overline{W}_{n+1,m} \right) \\
&= -\frac{GM}{R^2} \sqrt{\frac{(2n+1)(n+m+1)(n-m+1)}{(2n+3)}} \left( \overline{C}_{n,m} \overline{V}_{n+1,m} \right. \\
&\quad \left. + \overline{S}_{n,m} \overline{W}_{n+1,m} \right) \tag{2.71b}
\end{aligned}$$

The acceleration  $\ddot{\mathbf{r}}$  can be computed in Cartesian coordinates by adding the partial accelerations.

$$\ddot{x} = \sum_{n=0}^{\infty} \sum_{m=0}^n \ddot{x}_{n,m}, \quad \ddot{y} = \sum_{n=0}^{\infty} \sum_{m=0}^n \ddot{y}_{n,m}, \quad \ddot{z} = \sum_{n=0}^{\infty} \sum_{m=0}^n \ddot{z}_{n,m}. \tag{2.72}$$

## 2.4 Non-gravitational forces acting on a spacecraft

The orbit of a spacecraft is not only driven by gravitational forces but modified also by solar radiation pressure, atmospheric drag and other effects acting on a spacecraft. These forces will be described in detail in the following without claiming to be complete.

### 2.4.1 Solar radiation pressure

The Sun emits light energy (photons) depending on solar activity. During periods of intense solar storms the radiation is very strong and the force caused by the radiation at times of low activity very small. The body of a spacecraft absorbs and reflects photons which causes small forces changing the orbit of the spacecraft. The magnitude of the acceleration is inversely proportional to the squared distance of the spacecraft from the Sun.

The solar radiation pressure depends on the number of incoming photons and on their energy. The energy of a photon is given by  $h \cdot f$ , where  $h$  is Plank's constant and  $f$  the frequency of the photon. The solar flux  $q_s$  is defined as solar energy  $\Delta E_f$  per time unit  $\Delta t$  which passes through the area  $A$ . Hence, the force acting on the spacecraft can be written:

$$\mathbf{F}_R = \frac{\Delta p}{\Delta t} = \frac{q_s}{c} A, \quad (2.73)$$

where  $c$  is the speed of light and  $\Delta p$  the impulse of the photon. The resulting radiation pressure is

$$\mathbf{P}_R = \frac{q_s}{c}. \quad (2.74)$$

The solar flux at a distance of  $r_0 = 1$  Astronomical Unit (AU) is approximately  $1367 \text{ W/m}^2$  (*Montenbruck and Gill* [2000]). The solar radiation pressure is  $\mathbf{P}_R = 4.56 \times 10^{-6} \frac{\text{N}}{\text{m}^2}$ . However, this is only the case if the surface absorbs all incoming photons and the incident radiation is perpendicular to the surface.

In Figure 2.9 a more general case is shown. Here  $A_{exp}$  is the exposed surface which is inclined to the incoming radiation by the incident angle  $\phi_{inc}$ . Fractions of the incoming radiation are absorbed and reflected. Reflection can take place specular, i.e. the incident angle  $\phi_{inc}$  equals the reflection angle  $\phi_{ref}$ , or diffuse, if this is not the case (see Figure 2.9). The fraction of specular or diffuse reflected radiation depends on the roughness of the surface, i.e. the optical properties of the spacecraft. The resulting accelerations caused by absorption, specular and diffuse reflection are according to *Milani et al.* [1987]:

$$\ddot{\mathbf{r}}_{abs} = -\frac{q_s}{c} \cos(\phi_{inc}) \frac{A_{exp}}{m_{SC}} \mathbf{e}_{\odot} \quad (2.75a)$$

$$\ddot{\mathbf{r}}_{spec} = -2\frac{q_s}{c} \cos^2(\phi_{inc}) \frac{A_{exp}}{m_{SC}} \mathbf{e}_N \quad (2.75b)$$

$$\ddot{\mathbf{r}}_{dif} = -\frac{q_s}{c} \cos(\phi_{inc}) \frac{A_{exp}}{m_{SC}} \left( \mathbf{e}_{\odot} + \frac{2}{3} \mathbf{e}_N \right). \quad (2.75c)$$

Here, vector  $\mathbf{e}_{\odot}$  is the unit vector in the direction of the sun and  $\mathbf{e}_N$  the vector normal to the surface. Introducing coefficients  $\alpha$ ,  $\delta$  and  $\varepsilon$  describing the fraction of absorbed, diffuse and specular reflected radiation ( $\alpha + \delta + \varepsilon = 1$ ) and combining equation (2.75a), (2.75b) and (2.75c), the acceleration due to the solar radiation pressure felt by a satellite with mass  $m_{SC}$  at a distance  $r_{\odot}$  from the Sun can be written as

$$\ddot{\mathbf{r}} = -k \frac{q_s}{c} \frac{r_0^2}{r_{\odot}^2} \cos(\phi_{inc}) \frac{A_{exp}}{m_{SC}} \left( (\alpha + \delta) \mathbf{e}_{\odot} + 2 \left( \varepsilon \cos(\phi_{inc}) + \delta \frac{1}{3} \right) \mathbf{e}_N \right). \quad (2.76)$$

Here  $r_0$  is 1 AU. The activity of the Sun, i.e. the solar flux is not constant over time, which is accounted for by introducing a scaling factor  $k$ . This scaling factor is usually treated as a free parameter in the orbit determination process.

Equation (2.76) can be simplified if it is assumed that the surface normal  $\mathbf{e}_N$  always points in the direction of the Sun and if no detailed information about the optical properties of the spacecraft is available:

$$\ddot{\mathbf{r}} = -k \frac{q_s}{c} \frac{r_0^2}{r_{\odot}^2} \frac{A_{exp}}{m_{SC}} \mathbf{e}_{\odot} \quad (2.77)$$

This expression can also be used if no high precision is acquired.

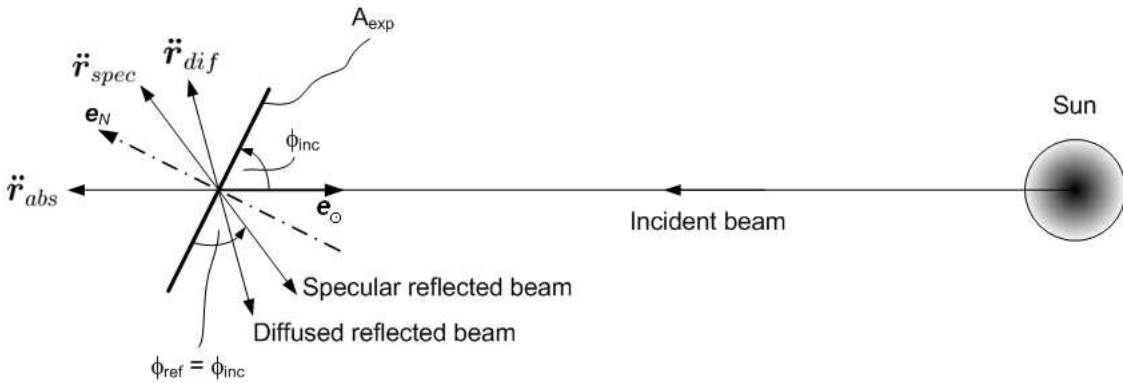


**Figure 2.9:** The incident radiation results in accelerations  $\ddot{\mathbf{r}}_{abs}$ ,  $\ddot{\mathbf{r}}_{spec}$  and  $\ddot{\mathbf{r}}_{dif}$  caused by absorption, specular and diffuse reflection

### 2.4.2 Shadow function

The acceleration given by equation (2.76) assumes full illumination of the satellite by the Sun. In a realistic scenario it is possible that the satellite disappears behind the planet as seen from the Sun and therefore is not or only partially exposed to the solar radiation pressure. This problem can be solved by introducing a shadow function  $\nu$ , which is defined as follows

$$\begin{aligned} \nu &= 0, \text{ if the satellite is behind the planet and entirely in the shadow,} \\ \nu &= 1, \text{ if the satellite is fully illuminated by the Sun, and} \\ 0 &< \nu < 1 \text{ partially illuminated by the Sun.} \end{aligned}$$

*Montenbruck and Gill* [2000] developed analytical expressions for illumination conditions from a conical shadow model. The apparent radius of the occulted body (the Sun)  $a$ , the apparent radius of the occulting body (the planet)  $b$  and the apparent separation of the centers of both bodies  $c$  can be obtained via the following equations.

$$a = \arcsin \frac{R_{\odot}}{|\mathbf{r}_{\odot} - \mathbf{r}|} \quad (2.78)$$

$$b = \arcsin \frac{R_B}{s} \quad (2.79)$$

$$c = \arccos \frac{-\mathbf{s}^T (\mathbf{r}_{\odot} - \mathbf{r})}{s |\mathbf{r}_{\odot} - \mathbf{r}|} \quad (2.80)$$

Here,  $R_{\odot}$  is the Radius of the Sun (696000 km),  $\mathbf{r}_{\odot}$  the coordinates of the Sun,  $\mathbf{r}$  the coordinates of the spacecraft,  $R_B$  the radius of the occulted body, and  $\mathbf{s}$  the vector from spacecraft to occulted body. The occulted array is then

$$A = a^2 \cdot \arccos \left( \frac{x}{a} \right) + b^2 \cdot \arccos \left( \frac{c-x}{b} \right) - c \cdot y, \quad (2.81)$$

with

$$x = \frac{a^2 + c^2 - b^2}{2c} \quad (2.82)$$

$$y = \sqrt{a^2 - x^2}. \quad (2.83)$$

Hence, the remaining fraction of the radiation on the spacecraft is

$$\nu = 1 - \frac{A}{\pi a^2}. \quad (2.84)$$

Accordingly, the resulting acceleration from the solar radiation pressure (see equation (2.76)) felt by the spacecraft is

$$\ddot{\mathbf{r}} = -\nu k \frac{q_s r_0^2}{c r_{\odot}^2} \cos(\phi) \frac{A_{exp}}{m_{sc}} \left( (\alpha + \delta) \mathbf{e}_{\odot} + 2 \left( \varepsilon \cos(\phi) + \delta \frac{1}{3} \right) \mathbf{e}_N \right). \quad (2.85)$$

### 2.4.3 Atmospheric drag

A spacecraft orbiting a planet encounters air molecules from the planet's atmosphere. The change in the molecules' momentum due to collision with the spacecraft leads to a force acting on the spacecraft, called atmospheric drag. This force depends on the local density of the atmosphere and the surface area of the spacecraft exposed in the direction of motion (*Montenbruck and Gill* [2000])

$$\ddot{\mathbf{r}}_D = -\frac{1}{2}C_D \frac{A_{exp}}{m_{sc}} \rho v_r^2 \mathbf{e}_v, \quad (2.86)$$

where  $\rho$  is the atmospheric density,  $v$  is the velocity of the spacecraft relative to the atmosphere and  $C_D$  is the drag coefficient, a dimensionless quantity, which describes the interaction between the surface material of the spacecraft and the atmosphere. Usually  $C_D$  or the ballistic coefficient  $C_D \frac{A_{exp}}{m_{sc}}$  is estimated in the orbit determination process as a free parameter. The unit vector  $\mathbf{e}_v = \frac{\mathbf{v}_r}{v_r}$  allows for the fact that the direction of the drag acceleration is always anti-parallel to the relative velocity vector  $\mathbf{v}_r$ . The relative velocity of the spacecraft can be computed under the assumption that the atmosphere co-rotates with the planet

$$\mathbf{v}_r = \mathbf{v} - \boldsymbol{\omega} \times \mathbf{r}, \quad (2.87)$$

with the inertial velocity vector of the spacecraft  $\mathbf{v}$ , the position vector  $\mathbf{r}$  and the angular velocity of the planet  $\boldsymbol{\omega}$ . The atmospheric density can be computed either from standard atmospheric models or from dynamic models. It is also necessary to use a precise model for the spacecraft as it is used for the solar radiation pressure modeling.

### 2.4.4 Albedo and infrared radiation

The incoming solar radiation reflected and scattered from a body is called albedo radiation. The optical albedo indicates the ability of reflection and scattering of the incident solar radiation, i.e. the ratio of reflected and incoming radiation, and is usually given in percent of the reflected radiation from the body. In addition, planetary surfaces and atmospheres emit infrared radiation, which also contributes to the radiation pressure felt by an orbiting spacecraft.

*Montenbruck and Gill* [2000] gives a formulation which accounts for the acceleration acting on a spacecraft due to optical and infrared radiation summing up individual terms, corresponding to different area elements  $dA_j$  of the planet

$$\ddot{\mathbf{r}}_{rad} = \sum_{j=1}^N C_R \left( \nu_j a_j \cos \theta_j^E + \frac{1}{4} \epsilon_j \right) \frac{q_s A_{exp}}{c m_{sc}} \cos \theta_j^S \frac{dA_j}{\pi r_j^2} \mathbf{e}_j. \quad (2.88)$$

Here,  $C_R$  is the radiation pressure coefficient of the spacecraft,  $\nu_j$  the shadow function for the planets area element  $dA_j$ ,  $a_j$  the albedo,  $\epsilon_j$  the emissivity,  $\theta_j^E$  and  $\theta_j^S$  the angles

of the planet surface or spacecraft surface normals to the incident radiation,  $\frac{q_s}{c}$  the radiation pressure,  $r_j$  the distance between planet and spacecraft, and  $\mathbf{e}_j$  the unit vector from the surface to the spacecraft.

### 2.4.5 Thrust forces

In order to control the orbit and the attitude of spacecraft the thruster-system on board a spacecraft has to be applied. For a detailed orbit determination this effect has to be accounted for. Thrusters are burned best in pairs to produce a pure momentum-free torque. Thrusters are acting primarily in the along-track and cross-track direction. Maneuvers can be treated as instantaneous velocity increments taking place at time  $t_m$

$$\mathbf{v}(t_m^+) = \mathbf{v}(t_m^-) + \Delta\mathbf{v}(t_m). \quad (2.89)$$

Dealing with extended maneuvers needs a complex thrust model but in the following only a simple model based on constant thrust is shown (*Montenbruck and Gill [2000]*). A spacecraft of mass  $m$  experiencing a thrust acceleration assuming a one dimensional motion

$$a = \frac{F}{m} = \frac{|\dot{m}|c_e}{m}, \quad (2.90)$$

with propellant mass  $|dm| = |\dot{m}| dt$  ejected from the propulsion system per time  $dt$  at velocity  $c_e$ .

The entire velocity increment can be computed by integration over the burn time  $\Delta t$

$$\begin{aligned} \Delta v &= \int_{t_0}^{t_0+\Delta t} a(t) dt = -c_e \int_{m(t_0)}^{m(t_0+\Delta t)} \frac{1}{m} dm \\ &= -c_e \ln \frac{m(t_0 + \Delta t)}{m(t_0)}, \end{aligned} \quad (2.91)$$

which is the Ziolkowski equation. Assuming a constant mass-flow rate  $|\dot{m}|$ , the entire velocity increment is

$$\Delta v = -\frac{F}{|\dot{m}|} \ln \left( 1 - \frac{|\dot{m}| \Delta t}{m(t_0)} \right). \quad (2.92)$$

Using equation (2.90) and (2.92) the resulting acceleration is then

$$a(t) = \frac{|\dot{m}|}{m(t)} \frac{1}{-\ln \left( 1 - \frac{|\dot{m}| \Delta t}{m(t_0)} \right)} \Delta v. \quad (2.93)$$

Introducing a time-dependent set of orthogonal unit vectors  $\mathbf{e}_1, \mathbf{e}_2, \mathbf{e}_3$  with constant projected thrust vector components  $F_1, F_2$  and  $F_3$  the resulting acceleration in the inertial reference frame is given by

$$\mathbf{a}(t) = \frac{|\dot{m}|}{m(t)} \frac{1}{-\ln\left(1 - \frac{|\dot{m}|\Delta t}{m(t_0)}\right)} \mathbf{E} \Delta \mathbf{v}(t), \quad (2.94)$$

where  $\Delta \mathbf{v}(t)$  are the velocity increments in the thrust reference frame and the rotation matrix  $\mathbf{E}(t) = (\mathbf{e}_1, \mathbf{e}_2, \mathbf{e}_3)$  transforms the acceleration from the thrust reference frame into the inertial frame.

In the case of a negligible mass flow  $|\dot{m}| \Delta t \ll m(t_0)$  the resulting acceleration can be simplified to

$$\mathbf{a}(t) = \frac{1}{m} \mathbf{E}(t) \begin{pmatrix} F_1 \\ F_2 \\ F_3 \end{pmatrix}. \quad (2.95)$$

## 2.5 Force model

In the following section the force model used for Mars Express (MEX) and Rosetta (ROS) is defined and the accuracy of the force model is tested. There are no synthetically generated orbit data available which would allow to compare the orbit resulting from the force model. The flight dynamics team at European Space Operation Center (ESOC) however provides reconstructed orbit data for MEX based on Doppler and ranging measurements (*del Rio* [2006]). *Rosenblatt et al.* [2008] provides also a reconstructed orbit for MEX with a slightly higher precision which can be used as a reference orbit for comparison. In the case of ROS no reconstructed orbit data are available but ESOC provides predicted orbit data appropriate for comparison.

The position of the Sun and the planets of the solar system are computed according to the latest released ephemeris file *DE421* from Jet Propulsion Laboratory (JPL) (*Folkner et al.* [2008]). The values of the according body masses are listed in Table A.1.

### 2.5.1 Mars Express

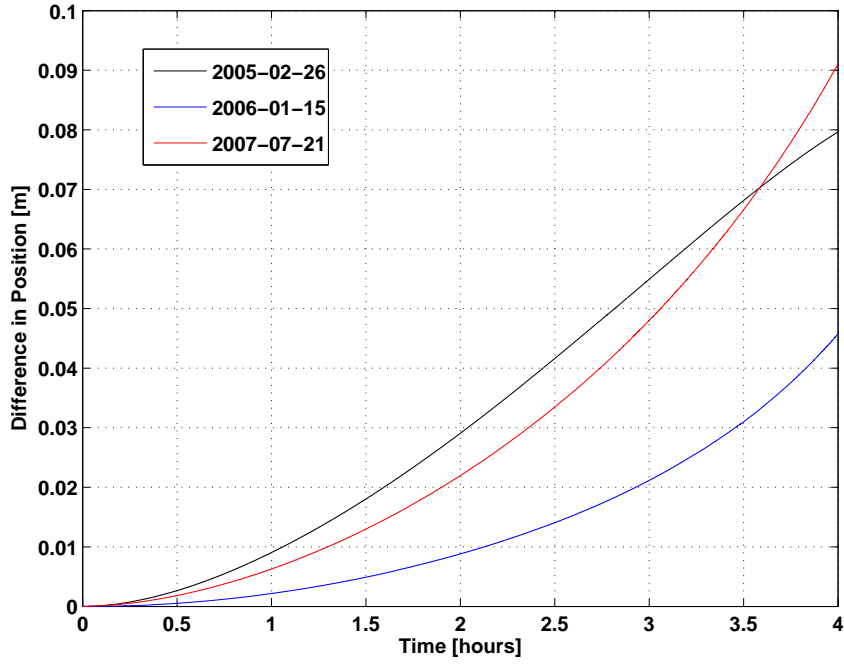
In order to test the accuracy of the MEX orbit by integrating the equation of motion, a reference orbit is needed for comparison. *Rosenblatt et al.* [2008] determined an accurate orbit of MEX and published the data in form of SPICE-kernels. The orbit determination was computed with the software package Geodesie par Integrations Numeriques Simultanees (GINS) originally developed at Centre National d'Etudes Spatiales (CNES) to compute precise orbits of satellites around the Earth as well as its gravity fields (*Marty et al.* [2007]). Therefore the force model used in GINS and for the determination of the reference orbit of MEX is adequate for testing the force model developed in this thesis.

The MEX orbit provided by *Rosenblatt et al.* [2008] is compared with the results from the integration of the following equation of motion:

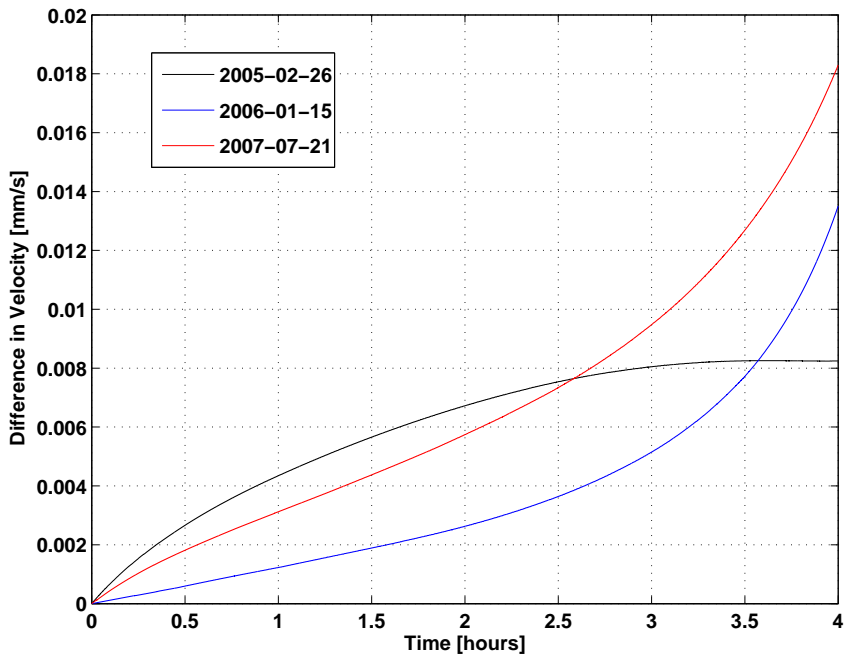
$$\mathbf{a}_{SC} = \mathbf{a}_c + \mathbf{a}_{Ph} + \mathbf{a}_{De} + \mathbf{a}_{\odot} + \mathbf{a}_{Pl} + \mathbf{a}_{SR}. \quad (2.96)$$

Here, Mars is treated as the central body in the equation of motion (see section 2.3.3 for more details) and  $\mathbf{a}_c$  is the acceleration caused by the gravity field of Mars. The latest gravity model *MGS95J* to degree and order 95 (*Konopliv et al.* [2006]) is used. The accelerations from the gravity field model of Mars are computed according to the recursion formalism developed in section 2.3.5. The seasonal changes of the gravity coefficients caused by the mass exchange between the polar ice caps and atmosphere are neglected in the gravity model for Mars because their contributions are small at distances from Mars where flybys are usually performed.

$\mathbf{a}_{Ph}$  and  $\mathbf{a}_{De}$  are the accelerations by the point mass representation of the Martian moons Phobos and Deimos.  $\mathbf{a}_{\odot}$  and  $\mathbf{a}_{Pl}$  are the point mass representations of the Sun and the planets, respectively.



(a) Difference in position



(b) Difference in velocity

**Figure 2.10:** Comparison of the position and velocity obtained from the integration of the equation of motion based on the force model (equation 2.96) with a reference orbit for Mars Express provided by Rosenblatt et al. [2008]. The difference between the reference orbit and the integrated orbit is in position and velocity for all three time periods (February 26, 2005 from 09:00 am - 1:00 pm ( $k = 1.11$ ), January 15, 2006 from 6:00 pm - 10:00 pm and September 21 ( $k = 1.18$ ), 2007 from 7:00 pm - 11:00 pm ( $k = 1.23$ )) smaller than 9 cm and 0.02 mm/s, respectively. This difference is very small compared to the total Doppler velocity error of 0.26 mm/s at X-band due to transponder noise at the ground station and transponder phase noise (see section 2.9)

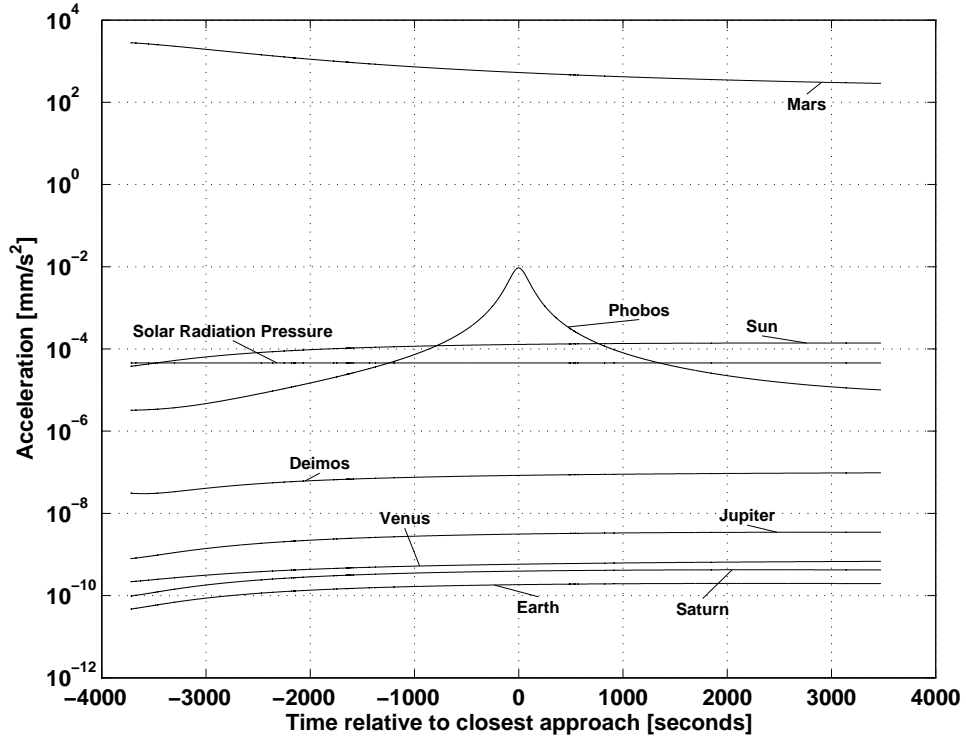
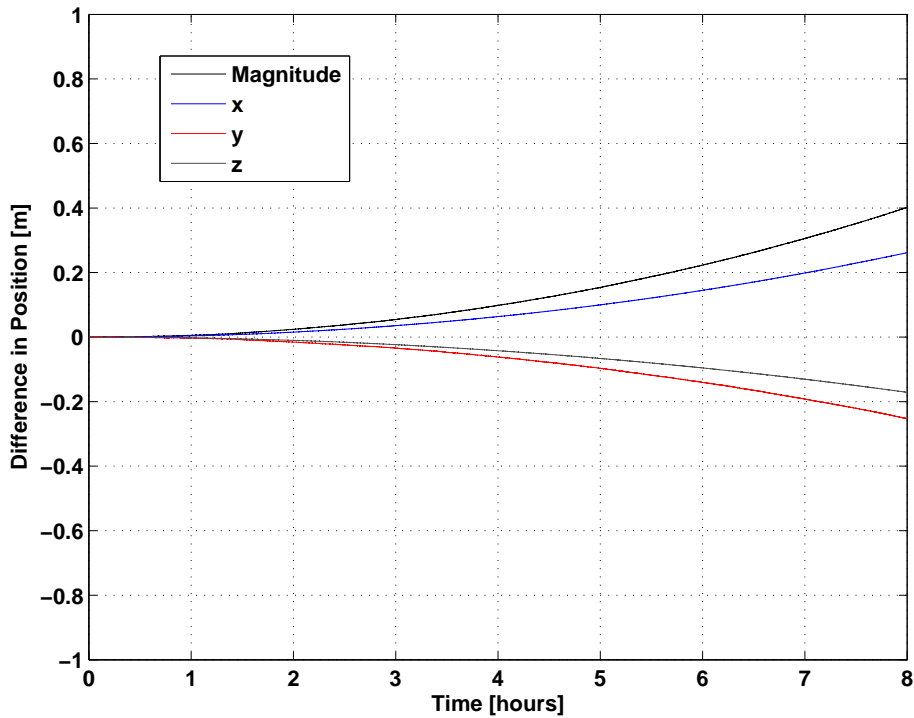


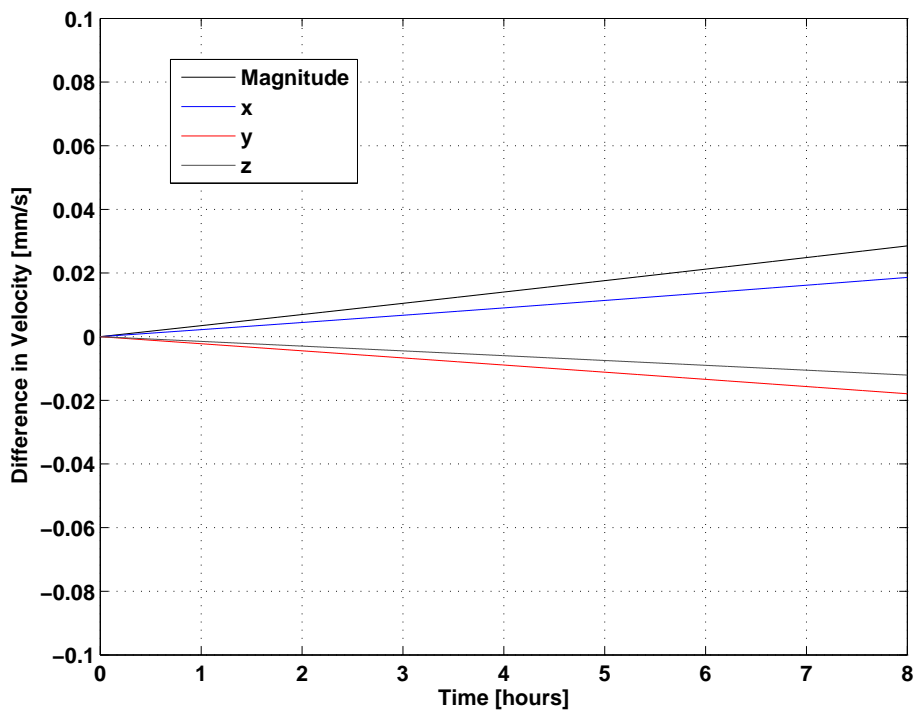
**Figure 2.11:** Forces acting on MEX  $\pm 1$  hour around closest approach of the flyby in July, 2008 (see section 5.1.1.2)

The acceleration caused by the solar radiation pressure is  $\mathbf{a}_{SR}$ . A detailed model for the optical parameter of each surface of MEX has been provided by *Morley* [2004] and can be found in Table A.2. The direction of the Sun with respect to orientation of the bus and the solar panels of MEX are determined and incorporated into the computation as well as a shadow function representing the illumination of the spacecraft. The detailed description of the models can be found in section 2.4.1.

In Figure 2.11 the accelerations acting on the spacecraft at the time of the closest approach for the flyby in 2008 at Phobos (see section 5.1.1.2) are shown as an example. The largest acceleration is caused by Mars as the central body, followed by Phobos, Sun and the solar radiation pressure. The accelerations caused by the planets are very small with the contribution by the Earth as the smallest one with  $\mathbf{a}_E \approx 3 \cdot 10^{-10}$  mm/s<sup>2</sup>. The velocity change after 4 hours is approximately  $10^{-7}$  mm/s. Accelerations smaller than that of the Earth from other bodies are not considered in the force model due to their insignificant contributions. The distance between Mars and MEX ranges during the close flyby between 5000 km - 10000 km. The acceleration by atmospheric drag equals zero due the absence of atmosphere particles at this distances. Accelerations caused by optical and infrared radiation are at this distance smaller than  $10^{-11}$  mm/s<sup>2</sup> according to equation (2.88). They are also neglected. No Wheel off-Loading (WoL) events or spacecraft manoeuvre occur when the close flyby at Phobos was performed. Therefore, no such contributions are considered in the force model.



(a) Difference in position



(b) Difference in velocity

**Figure 2.12:** Comparison of the position and velocity from integration of the equation of motion with a reference orbit for ROS at September 4, 2008 from 12:00 - 20:00. The scaling factor for the acceleration due to the solar radiation pressure  $k = 1.32$ . The difference between the reference orbit and the integrated orbit is in position and velocity 40 cm and 0.025 mm/s, respectively. This difference is very small compared to the total Doppler velocity error of 0.26 mm/s at X-band due to transponder noise at the ground station and transponder phase noise (see section 2.9).

The position and velocity is compared with the reference orbit for three time periods. Different values for the scaling factor  $k$  of the solar radiation pressure are used for comparison (see section 2.4.1): On February 26, 2005 from 09:00 am - 1:00 pm ( $k = 1.11$ ), January 15, 2006 from 6:00 pm - 10:00 pm and September 21 ( $k = 1.18$ ), 2007 from 7:00 pm - 11:00 pm ( $k = 1.23$ ). The distance between MEX and Mars is similar to the distance at close flybys at Phobos at these time periods.

The position and velocity differences shown in Figure 2.10(a) and 2.10(b) are for all three time periods smaller than 9 cm and 0.02 mm/s, respectively. These differences are smaller than the accuracy of the measurements stated by *Rosenblatt et al.* [2008] to be 1.2 mHz or 0.02 mm/s and 3 m at an integration time of 60 seconds (X-band at 8.5 GHz). That proves that the integration of the equation of motion and the selected force model provides an adequate precision. The used values of the scaling factor  $k$  of the solar radiation pressure are also very close to the values from *Rosenblatt et al.* [2008] which demonstrates the precision of the complex model for the solar radiation pressure.

*Rosenblatt et al.* [2008] used an older model for the position of the Sun and the planets of the solar system which explains the small differences between the reference orbit and the integrated orbit. The high precision of the numerical force model developed in this thesis has been shown by this comparison.

## 2.5.2 Rosetta

The flight dynamics team at ESOC provides predicted orbit data for the entire mission. These orbit data are less precise compared to the data for MEX but accurate enough for testing the precision of the force model developed for the Rosetta spacecraft in this thesis.

ROS conducts close flybys at Mars and Earth on its way to 67 P/Churyumov-Gerasimenko. For the two asteroid flybys at Steins and Lutetia the force model from MEX is adapted to ROS as follows

$$\mathbf{a}_{SC} = \mathbf{a}_c + \mathbf{a}_{As} + \mathbf{a}_{Pl} + \mathbf{a}_{SR}. \quad (2.97)$$

Here  $\mathbf{a}_c$  is the acceleration caused by the central body, the Sun, treated as a point mass,  $\mathbf{a}_{As}$  the acceleration from the gravitational attraction of the asteroids Lutetia or Steins, and  $\mathbf{a}_{Pl}$  the acceleration due to the point mass representations of the planets.

The acceleration caused by the solar radiation pressure is  $\mathbf{a}_{SR}$ . A detailed model for the optical parameter of each of Rosetta surface is provided by *Morley* [2008] and listed in Table A.3. The Rosetta spacecrafts bus with the dimensions  $2.8 \times 2.1 \times 2.0$  m and the area  $A = 32.13 \text{ m}^2$  of the solar panels are very large. Therefore, a complex model for  $\mathbf{a}_{SR}$  is used, i.e. the direction of the Sun with respect to the orientation of each area of the bus and the solar panels of the spacecraft are determined separately. A detailed description can be found in section 2.4.1.

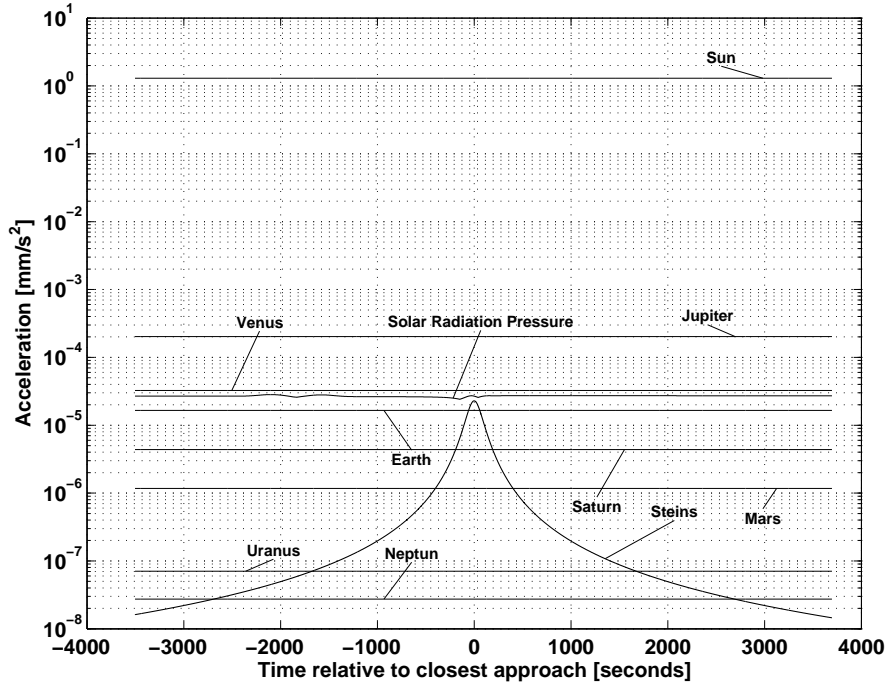


**Figure 2.13:** Forces acting on Rosetta  $\pm 1$  hour around closest approach of the Steins flyby in September, 2008 (see section 5.2)

Figure 2.13 shows the accelerations felt by ROS at the time of the closest approach at the asteroid Steins (see section 5.2) according to the force model. The influence of the outer planets is larger compared to the MEX force model. The acceleration due to the solar radiation pressure is in the same order of magnitude as for MEX although the solar panels of ROS having a much larger area which is compensated by the larger distance to the Sun.

In Figure 5.20(a) and 5.20(b) a comparison between the orbit provided by ESOC and a orbit based on the force model at September 4, 2008 from 12:00 am - 8:00 pm is shown with a scaling factor for the solar radiation pressure  $k = 1.32$ . The difference in position and velocity after eight hours integration time is 40 cm and 0.025 mm/s, respectively. This shows the high precision of the numerical force model for the Rosetta spacecraft. The time period for comparison is selected because it is close to the flyby at the asteroids Steins. For other time periods the difference remains in the same order of magnitude.

### 2.5.3 Precision of the force model

The high precision of the orbit computed with the integration method (see section 2.2) for the equation of motion and the force model established for Mars Express and Rosetta at the time of the flybys has been demonstrated by the comparison with reference orbits. The difference in velocity is for both spacecrafts 0.02 mm/s. This difference is very small compared to the total Doppler velocity error of 0.26 mm/s at X-band due to transponder noise at the ground station and transponder phase noise (see section 2.9).

## 2.6 The relativistic Doppler effect

If a spacecraft is transmitting an electromagnetic wave with frequency  $f_T$  and on Earth the signal is received via a ground station with frequency  $f_R$ , the relativistic Doppler effect taking into account effects of special relativity of order  $(\frac{v}{c})^2$  and effects of the general relativity can be computed from the following equation (see Figure 2.14) according to Häusler [2002]

$$\frac{\Delta f}{f_T} = 1 - \frac{1 - \mathbf{n}\boldsymbol{\beta}_R + \frac{1}{2}|\boldsymbol{\beta}_R|^2 - \frac{\Phi_R}{c^2}}{1 - \mathbf{n}\boldsymbol{\beta}_T + \frac{1}{2}|\boldsymbol{\beta}_T|^2 - \frac{\Phi_T}{c^2}}. \quad (2.98)$$

Here,

- $\Delta f$  is the Doppler frequency shift with  $\Delta f = f_T - f_R$  where  $f_T$  is the transmitted frequency and  $f_R$  is the received frequency,
- $\mathbf{n}$  is the normalized vector from transmitter at transmission time  $t_T$  to receiver at receiving time  $t_R$ ,
- $\boldsymbol{\beta}_T$  is the normalized velocity of transmitter with  $\boldsymbol{\beta}_T = \frac{\mathbf{v}_T}{c}$ , where  $\mathbf{v}_T$  is the velocity of the transmitter at the time of transmission  $t_T$ ,
- $\boldsymbol{\beta}_R$  is the normalized velocity of receiver with  $\boldsymbol{\beta}_R = \frac{\mathbf{v}_R}{c}$ , where  $\mathbf{v}_R$  is the velocity of the receiver at the time of reception  $t_R$ ,
- $c$  is the speed of light,
- $\Phi_T$  is the gravity potential of the Sun and the planet in which sphere of influence the transmitter is located, with  $\Phi_T = -\frac{\mu_\odot}{r_\odot} - \frac{\mu_p}{r_p}$  and  $r_\odot$  the distance from the transmitter to the Sun and  $r_p$  the distance from the transmitter to the planet, and
- $\Phi_R$  the gravity potential of the Sun and the planet in which sphere of influence the receiver is located, with  $\Phi_R = -\frac{\mu_\odot}{r_\odot} - \frac{\mu_p}{r_p}$  and  $r_\odot$  the distance from the receiver to the Sun and  $r_p$  the distance from the receiver to the planet.

If the receiver or transmitter is located on Earth the centrifugal acceleration from Earth rotation should also to be taken into account using the following equation

$$\Phi_c = -\frac{1}{2} \cdot \left( \omega_\otimes \sin \left( \frac{\Pi}{2} - \phi \right) r \right)^2, \quad (2.99)$$

whereas

- $\omega_\otimes$  is the angular velocity of the Earth in radian per second,
- $\phi$  the geographical latitude of the ground station, and
- $r$  distance from the center of the earth to the ground station.

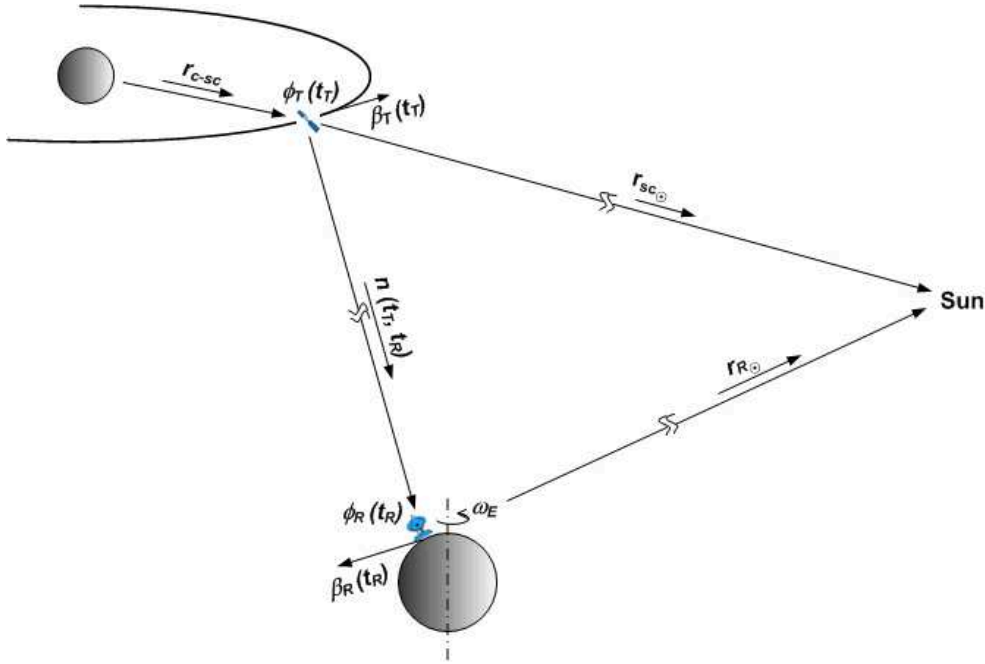


**Figure 2.14:** Parameter for the computation of the relativistic Doppler effect in the down-link case i.e. the spacecraft is transmitting a radio signal to the ground station located on Earth.

Equation (2.98) requires the knowledge of the travel time of the radio signal from the instant of transmission to the instant of reception. These light time corrections are calculated iteratively starting from an initial value (assuming infinite speed of light) using a Newtonian formulation (Häusler [2002], NAIF [2009]).

In the literature other approximations can be found for the relativistic Doppler effect (Morabito and Asmar [1995], Schneider [1988], Ashby [2003] or Soffel [1989]). However the differences between the different expressions for the relativistic Doppler effect is in the range of a few mHz (Selle [2005]). The precision of the used formulation (2.98) is tested in section 3.

## 2.6.1 Relativistic summation

If the normalized velocity in equation 2.98 is computed barycentric and planetocentric velocities have to be added but it has to be taken care that nothing moves faster than light. Therefore the velocities have to be summed up in a relativistic way.

Assuming a system  $S'$  moving relative to system  $S$  with the velocity  $\mathbf{u}$  and an observer is situated in the system  $S$ . A body is assumed to have the velocity  $\mathbf{v}'$  in system  $S'$ . Calculating the velocity  $\mathbf{v}$  of the body in system  $S$  in a non-relativistic way can be done via

$$\mathbf{v} = \mathbf{v}' + \mathbf{u}. \quad (2.100)$$

However, if  $|\mathbf{u}|$  and  $|\mathbf{v}'| > \frac{c}{2}$  this would lead to  $|\mathbf{v}| > c$ . This can't be true, because the effects of time dilatation and contraction of the length requires the existence of a limited velocity not depending on the reference frame.

The time dilatation, i.e. the time interval between two events in the moving system  $S'$ , seems to be extended for the observer in the resting frame  $S$  by the Lorentz term

$$\gamma = \frac{1}{\sqrt{1 - \left(\frac{u}{c}\right)^2}} \quad (2.101)$$

and the contraction of the length, i.e. the length of a distance in the moving system  $S'$ , seems to be for the observer in the resting system  $S$  shortened by the factor  $\frac{1}{\gamma}$ .

The velocity in the system  $S$  is via relativistic summation (see *Dorfmüller et al.* [1998])

$$\mathbf{v} = \frac{1}{\gamma(1 + \boldsymbol{\beta}_u \cdot \boldsymbol{\beta}_{v'})} (\mathbf{v}' + (\gamma - 1)(\mathbf{v}' \cdot \tilde{\mathbf{u}}) \tilde{\mathbf{u}} + \gamma \mathbf{u}), \quad (2.102)$$

whereas

- $\tilde{\mathbf{u}}$  is the unit vector of the velocity  $\mathbf{u}$  of the system  $S'$  relative to system  $S$ ,
- $\boldsymbol{\beta}_u$  the normalized velocity of the system  $S'$  relative to system  $S$ , i.e.  $\frac{\mathbf{u}}{c}$ , and
- $\boldsymbol{\beta}_{v'}$  the normalized velocity of the body in system  $S'$ , i.e.  $\frac{\mathbf{v}'}{c}$ .

## 2.6.2 Precise ground station position

The precise modeling of the Doppler effect requires an accurate knowledge at centimeter level of the position of the ground station on the surface of the Earth. The crust of the Earth is variable and reference points are displaced by linear effects like the tectonic plate motion and non-linear effects like the solid Earth tides. Methods to model this effects are described in the following.

In the celestial reference frame for a precise ground station position effects due to precession, nutation, Earth rotation, and polar motion have to be taken into account. In section 2.1.3 the transformation from the celestial to the terrestrial coordinate system is described in which the effects are considered.

### 2.6.2.1 Tectonic plate motion

The lithosphere of the Earth is divided laterally into a number of tectonic plates. Twelve major plates and several minor plates exist. The tectonic plates are moving relative to each other and a comprehensive model of current plate motions shows rates of separation at plate boundaries that range from 20 mm/year in the North Atlantic to about 160 mm/year on the East Pacific Rise. The model also gives rates of closure ranging from about 10 mm/year between Africa and Eurasia to about 80 mm/year between the Naza plate and South America.

Depending on the location of the ground station the site displacement from tectonic plate motion has to be considered for a precise ground station position. The NNR-NUVEL1A model for plate motions (see *McCarthy and Petit* [2003]) can be used for

modeling. From the original coordinates  $\mathbf{r}_0 = (x_0, y_0, z_0)$  in the International Terrestrial Reference Frame (ITRF) (see section 2.1) at time  $t_0$  new coordinates  $\mathbf{r} = (x, y, z)$  at time  $t$  can be computed from the Cartesian rotation vector  $\mathbf{\Omega}$  via

$$x = x_0 + (\Omega_y z_0 - \Omega_z y_0) (t - t_0) \quad (2.103)$$

$$y = y_0 + (\Omega_z x_0 - \Omega_x z_0) (t - t_0) \quad (2.104)$$

$$z = z_0 + (\Omega_x y_0 - \Omega_y x_0) (t - t_0). \quad (2.105)$$

The values of the rotation vector  $\mathbf{\Omega}$  for each of the major plates can be found in Table A.4 in the appendix.

### 2.6.2.2 Site displacement due to solid Earth tides

Tidal forces arise from gravitational attraction of bodies external to the Earth. The resulting deformation of the shape of the non perfectly rigid Earth causes site displacements. The tidal acceleration at a point on or in the Earth is the difference between the acceleration caused by the attraction of the external body and the orbital acceleration. Assuming the Earth being spherical symmetric, the orbital acceleration is the acceleration caused by the attraction of the external body at the Earth's center of mass, making the tidal force the difference between the attraction at the center of mass, and that at the point of observation. The tidal potential can be expressed as (*Agnew* [2007])

$$V_{tid} = \frac{GM_{ex}}{R(t)} \sum_{n=2}^{\infty} \left( \frac{a}{R(t)} \right)^n \frac{4\pi}{2n+1} \sum_{m=-n}^n Y_{nm}^* (\theta' (t), \phi' (t)) Y_{nm} (\theta, \phi). \quad (2.106)$$

Here,  $M_{ex}$  is the mass of the external body,  $R(t)$  the distance between the center of mass of the Earth and the center of mass of the external body,  $a$  the distance of the observation point on Earth from the center of mass of the Earth,  $\theta, \phi$  the colatitude and east longitude of the observation point, and  $\theta' (t), \phi' (t)$  the colatitude and east longitude of the sub-body point of the center of mass of the external body and  $Y_{nm} (\theta, \phi)$  the fully normalized complex spherical harmonics defined by

$$Y_{nm} (\theta, \phi) = N_n^m P_n^m (\cos \theta) e^{im\phi}. \quad (2.107)$$

Here,

$$N_n^m = (-1)^m \left[ \frac{2n+1}{4\pi} \frac{(n-m)!}{(n+m)!} \right]^{\frac{1}{2}} \quad (2.108)$$

is the normalizing factor and  $P_n^m$  is the associated Legendre polynomial of degree  $n$  and order  $m$ . The solid tides can be expressed as a sum of sinusoids as

$$T_{nm} = \sum_{k=1}^{k_{nm}} A_{knm} e^{i(2\pi f_{knm} t + \varphi_{knm})}, \quad (2.109)$$

where, for each degree  $n$  and order  $m$   $k_{nm}$  sinusoids with specified real amplitudes  $A$ , frequencies  $f$ , and phases  $\varphi$  are summed. A table of harmonic amplitudes and frequencies can be used to model the tidal potential. This method can be used for Earth tides of any type (*Agnew [2007]*).

*McCarthy and Petit [2003]* developed a numerical two-step procedure using the sum of sinusoids in order to model site displacements caused by solid tides which will be described only briefly here because of its complexity.

In the first step corrections in the time domain are computed, i.e. the in-phase correction for degree 2 and 3, the out-of-phase correction for degree 2 only of the diurnal and semidiurnal tides and the contribution from the latitude dependence of the diurnal and semidiurnal tides. The second step comprises estimating corrections in the frequency domain, i.e. the in-phase correction for degree 2 of the diurnal and semidiurnal tides and the in-phase and out-of-phase correction of degree 2 of the long-period tides. This model is used in this thesis for computing the site displacement effects due to solid Earth tides.

### 2.6.2.3 Other effects

There are additional effects which are changing the position of a ground station. Here, some of them are briefly described and summarized in Table 2.1 without claiming completeness.

- **Ocean loading**

The site displacement due to ocean loading is mainly in the horizontal direction. It is due to temporal variations of the ocean mass distribution and the associated load on the crust, which produces time-varying deformations of the Earth. Ground stations close to the coast or on islands are affected strongest. The effect has periods about 12 hours, 24 hours, 14 days, but also monthly and half year periods due to Sun and moon. The amplitude is smaller than that of the solid tides and in the range of a few centimeter.

- **Atmospheric loading**

The surface of the Earth is deformed by temporal variations in the geographic distribution of atmospheric mass load. The mass load variations can originate from pressure variations, for example seasonal pressure changes due to air mass movements between the continents and oceans. Other surface loads caused by changes in snow and ice cover, soil moisture and groundwater, as well as ocean bottom pressure also contribute to surface displacements, but for the latter ones no sufficient models are available. The atmospheric load from pressure variations can be modeled via two basic methods. Firstly, computing the corrections based on geophysical models or simple approximations or, secondly, using empirical

models based on site dependent data like meteorological data measured at the ground station. The order of magnitude of the effect due to atmospheric loading on the location of a ground station is approximately a few millimeter.

- **Thermal deformation of the antenna**

The structure of an antenna can be deformed depending on the temperature and can therefore cause errors in the position of the antenna. These errors are in the range of a few millimeter.

- **Postglacial rebound**

This is due to the slowly raising of the crust of the Earth since the polar caps are melt and the maximum is in the range of millimeter per year.

The order of magnitude of these effects are all in the range of centimeter or smaller (Table 2.1). With the complexity of the models, the effort of modeling this effects can not be justified with the higher accuracy and would go beyond the scope of this work. In this thesis plate tectonic and solid Earth tides effects are implemented in the computation of the ground station position which serves an accuracy at the centimeter level. A detailed description of the effects of site displacements and their accurate numeric modeling is given in *McCarthy and Petit* [2003].

Effect	Order of magnitude
Tectonic plate motion	cm/year
Solid Tides	dm
Ocean Tide Loading	cm
Pole Tides	mm - cm
Atmospheric Loading	mm
Thermal deformation of the antenna	mm
Postglacial rebound	mm/year

**Table 2.1:** Summary of the order of magnitude for site displacement effects (*Hennig [2008]*).

## 2.7 Data calibration

### 2.7.1 Introduction

An electromagnetic wave emitted from the spacecraft in order to be received at ground station and vice versa passes the atmosphere of the Earth. Thereby the wave interacts with electrons, ions, atoms and molecules contained in the Earth atmosphere and plasma environment. Thus the direction and velocity of propagation and also the polarization and the field strength of the signal is changed.

The velocity and the wavelength of an electromagnetic wave depends on the refractive index  $n$  of the surrounding media and is related by the following equation

$$n = \frac{c}{c_n} = \frac{\lambda}{\lambda_n}, \quad (2.110)$$

where  $c$  is the speed of light,  $\lambda$  the vacuum wavelength, and  $c_n$ ,  $\lambda_n$  are the corresponding values in media with refractive index  $n$ . The refractive index depends mainly on the dielectric constant, the permeability, and the conductivity of the medium.

Assuming a simplified model of a plane atmosphere with a constant refractivity the basic effect of the atmospheric refraction can be described by Snellius's law

$$n \sin(z) = \sin(z_0). \quad (2.111)$$

Here  $z_0$  is the zenith angle, i.e. the angle of the incoming ray and  $z$  the angle in the medium with refractive index  $n$ . The signal traversing the atmosphere is bended and due to the reduced velocity inside the atmosphere, if  $n > 1$ , a signal is delayed in time. Neglecting the small bending angle at Earth the path delay  $\Delta\tau$  caused in a layer with height  $h$  and refractive index  $n$  of the atmosphere is then

$$\Delta\tau = h(n-1) \frac{1}{\sin \epsilon}, \quad (2.112)$$

where  $\epsilon = 90^\circ - z_0$  is the elevation angle (*Montenbruck and Gill [2000]*). The troposphere of the Earth is a non-dispersive media for radio waves, i.e. the refractive index is independent from frequency, but for the ionospheric correction it must be distinguished between the refractive index of a single electromagnetic wave (e.g. the carrier phase) and wave groups (e.g. ranging signals).

The changes in signal path, i.e. frequency changes of the radio signal by the contributions of the troposphere and ionosphere of the Earth have to be removed accurately from the data in order to obtain the frequency, i.e. the Doppler velocity, due to the motion of a spacecraft. Different models for these corrections are shown in the following.

## 2.7.2 Modeling tropospheric delays

The troposphere of the Earth ranging from the sea surface level to approximately 8 km at the pole and 16 at the equator consists almost completely of neutral gas. The propagation of electromagnetic waves is mainly affected by the temperature  $T$ , the atmospheric pressure  $P$  and the partial pressure of water vapour  $e$ . The tropospheric refractive index is always larger than one. The tropospheric refraction consists of the refraction caused by the nonwater-vapor components of the atmosphere ( $N_2$ ,  $O_2$ ,  $CO_2$ , and Ar), the dry component, and the contribution of the highly variable water vapour content of the atmosphere, the wet component. Both have to be modeled separately. The tropospheric delay can be computed in general from

$$\tau_{tropo} = \delta_d m_d(\epsilon) + \delta_w m_w(\epsilon) . \quad (2.113)$$

In the following models for the path delay  $\delta_d$  and  $\delta_w$  in the zenith direction and the mapping functions  $m_d(\epsilon)$  and  $m_w(\epsilon)$  projecting the delay into the direction of the signal path for both components are shown.

The tropospheric correction models using the temperature  $T$  in Kelvin, the pressure  $P$  in hPa, the partial water vapour pressure  $e$  at ground station in hPa, the latitude  $\phi$  of the ground station and the height  $h$  of the ground station above the reference ellipsoid in km.

### 2.7.2.1 Zenith delay

#### Dry component:

- Model from *Janes et al.* [1991]

$$\delta_d = 1.552 \times 10^{-5} \left[ \frac{\text{m}}{\text{hPa}} \right] \frac{P}{T} (40136 [\text{K}] + 148.72 (T - 273.15 [\text{K}])) \quad (2.114)$$

- Model from *Saastamoinen* [1972]

$$\delta_d = \frac{2.2767 \times 10^{-3} \left[ \frac{\text{m}}{\text{hPa}} \right] P}{1 - 2.66 \times 10^{-3} \left[ \frac{1}{\text{km}} \right] \cos(2\phi) - 2.8 \times 10^{-4} \cdot h} \quad (2.115)$$

#### Wet component

- Model from *Mendes and Langely* [1998]

$$\delta_w = 0.122 [\text{m}] + 9.45 \times 10^{-3} \left[ \frac{\text{m}}{\text{hPa}} \right] e \quad (2.116)$$

- Model from *Ifadis* [1986]

$$\begin{aligned} \delta_w = & 5.54 \times 10^{-3} [\text{m}] - 8.8 \times 10^{-5} \left[ \frac{\text{m}}{\text{hPa}} \right] (P - 1000 [\text{hPa}]) \\ & + 2.72 \times 10^{-5} \left[ \frac{\text{m}}{\text{hPa}} \right] e + 2.771 \left[ \frac{\text{m K}}{\text{hPa}} \right] \frac{e}{T} \end{aligned} \quad (2.117)$$

### 2.7.2.2 Mapping functions

The mapping function projects the path delay in zenith direction into the direction of the signal path according to the elevation angle  $\epsilon$ .

#### Dry component:

- Mapping function from *Chao* [1972]

$$m_d(\epsilon) = \frac{1}{\sin \epsilon + \frac{0.00143}{\tan \epsilon + 0.00035}} \quad (2.118)$$

#### Wet component:

- Mapping function from *Chao* [1972]

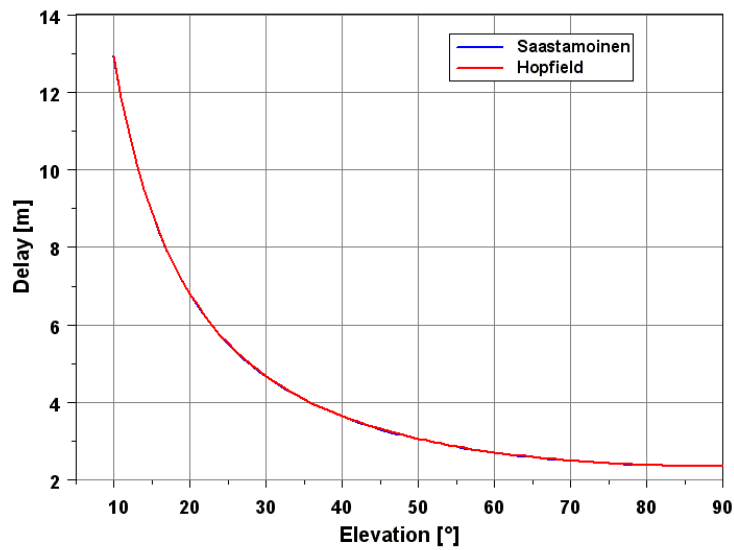
$$m_w(\epsilon) = \frac{1}{\sin \epsilon + \frac{0.00035}{\tan \epsilon + 0.0017}} \quad (2.119)$$

### 2.7.2.3 Comparison

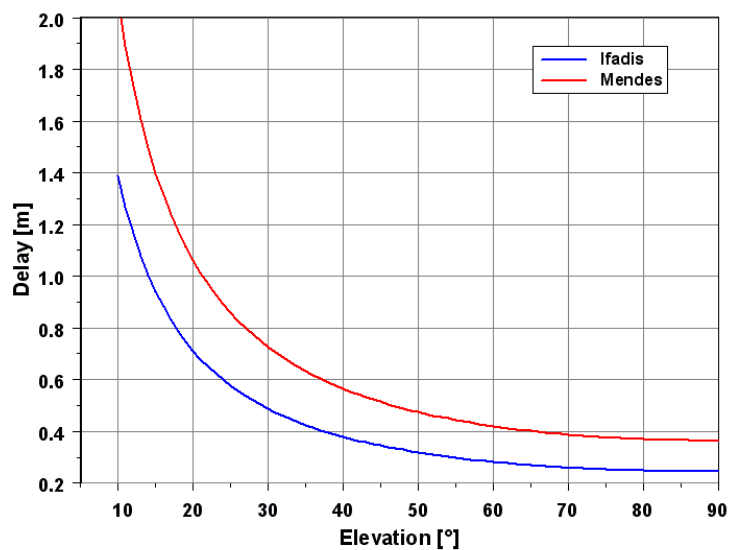
*Janes et al.* [1991] compared the results from the ray-tracing method with different models for tropospheric delay prediction using a standard atmosphere. The ray-tracing technique divides the atmosphere into small layers with respective refraction index and computes the ray path of the signal separately for each layer using Snellius's law. Therefore results from this method can be used for testing the accuracy of tropospheric delay predictions from the different models. *Janes et al.* [1991] found that the zenith delay model for the dry component from *Saastamoinen* [1972] agrees well within a few millimeters, but models for the wet component show differences in the centimeter level with the ray-tracing results. A comparison of ray-tracing results with several mapping functions performed by *Mendes and Langely* [1994] show agreements for all tested mapping functions in the sub-centimeter level.

This agreement can also be confirmed comparing the above defined models as it can be seen in Figure 2.15(a) for the dry component and in Figure 2.15(b) for the wet component. The path delay of the models are projected into the direction of the signal using the mapping functions according to equations 2.118 and 2.119.

For data analysis the model from *Saastamoinen* [1972] for the dry component and from *Ifadis* [1986] for the wet component, and the straightforward mapping functions from *Chao* [1972] are used.



(a) Dry component



(b) Wet component

**Figure 2.15:** Comparison of different models for the dry and wet component of the signal path delay caused by the troposphere of the Earth. Used for modeling are temperature  $T = 295.5$  K, pressure  $P = 978.0$  hPa and humidity  $H = 66$  %. The mapping functions are according to equation (2.118) and (2.119)

### 2.7.3 Ionospheric correction

The ionosphere of the Earth ranges from 50 km to 1000 km. The source of the ionospheric refraction, the ions and free electrons are mainly generated by the absorption of ultra violet radiation from the Sun. Different regions can be distinguished by the electron density: the D region (60 - 90 km), the E region (105 - 160 km) and the F region (160 - 500 km), which can be subdivided into the F<sub>1</sub> region (160 - 180 km) and the F<sub>2</sub> region (200 - 500 km). The D and F<sub>1</sub> region vanish at night, while the E region becomes considerably weaker and the F<sub>2</sub> region is also reduced. At an altitude of 300 km a maximum electron density of about 10<sup>12</sup> electrons/m<sup>3</sup> can be found.

The ionosphere is a dispersive medium, i.e. the refractive index is a function of the frequency of the signal. Neglecting the perturbations due to ions, the contributions from the magnetic field of the Earth, and absorption effects, the ionospheric refractive index is (Häusler [2008b])

$$n = 1 - \frac{1}{2} \frac{f_p^2}{f^2}. \quad (2.120)$$

Here,  $f_p$  denotes the plasma frequency varying from 10 MHz at day to 3 MHz at night

$$f_p = \frac{1}{2\pi} \sqrt{\frac{d_e e_0^2}{m_e \epsilon_0}}, \quad (2.121)$$

with the electron number density  $d_e$ , the electron charge  $e_0$ , the vacuum dielectric constant  $\epsilon_0$ , and the electron mass  $m_e$ . The ionospheric refraction leads to a reduction of the group velocity and an increase of the phase velocity. Both corrections for range and carrier phase measurements  $\Delta\rho$  and  $\Delta\phi$  are

$$\Delta\rho = \int_0^S (n - 1) ds = \frac{40.31 \left[ \frac{m^3}{s^2} \right]}{f^2} TEC \quad (2.122)$$

$$\Delta\phi\lambda_0 = 2\pi \int_0^S (n - 1) ds = -2\pi \frac{40.31 \left[ \frac{m^3}{s^2} \right]}{f^2} TEC. \quad (2.123)$$

Here is  $TEC$  the total electron content along the path length  $S$ . The electron density of the ionosphere varies with altitude, Sun activity and with local time. This makes it difficult to construct global ionospheric models that predict the electron density accurately. But the electron density can be measured and used for correction of the contributions of the ionosphere on an electromagnetic wave. For Deep Space Network (DSN) ground stations the ionospheric correction can be reconstructed from auxiliary files provided by the Tracking System Analytic Calibration (TSAC) group of JPL. For measurements recorded at European Space Agency (ESA) ground stations another method has to be used because no information is provided by ESA about ionospheric corrections. Both methods are explained and compared below.

### 2.7.3.1 Correction provided by TSAC

The TSAC group of JPL provides the path delay signature in form of a polynomial which can be computed from the polynomial coefficients  $a_i$  via (see *Morabito and Asmar [1995]*)

$$\Delta\rho_{ion}(t_j) = \sum_{i=0}^9 a_i x^i(t_j), \quad (2.124)$$

with

$$x(t_j) = 2 \frac{t_j - t_s}{t_e - t_s}. \quad (2.125)$$

Here  $t_j$  is the time stamp at which the correction have to be computed,  $t_s$  the start time  $t_e$  the stop time of the interval for which the polynomial is defined. Using the speed of light  $c$  the ionospheric correction  $f_{ion}^S$  scaled to a 2.3 GHz  $f_S$  frequency at time  $t_j$  can be computed from

$$f_{ion}^S(t_j) = \frac{f_S}{c} \cdot \frac{\Delta\rho_{ion}(t_j + \Delta t) - \Delta\rho_{ion}(t_j - \Delta t)}{\Delta t}. \quad (2.126)$$

This is only true for one-way S-band downlink. Appendix A.5.1 contains formulations from which the correction can be computed for other up- and downlink configurations.

### 2.7.3.2 The Klobuchar model

*Klobuchar [1975]* developed a model by representing the average monthly diurnal behavior of time delay at a location on Earth as a simple positive cosine wave dependence with a constant offset term (see also *Parkinson and Spilker [1996]*):

$$\Delta t_{iono} = \begin{cases} C & \text{if } \frac{(t-\phi)2\pi}{P} > 90^\circ \\ C + A \cos \frac{2\pi(t-\phi)}{P} & \text{else.} \end{cases} \quad (2.127)$$

Here,  $C$  is the constant offset,  $A$  the amplitude,  $P$  the period,  $\phi$  the phase of the function and  $t$  the local time at the ionospheric point. Using the first two terms of the Taylor expansion of the cosine function:

$$\Delta t_{iono} = C + A \left( 1 - \frac{x^2}{2} - \frac{x^4}{24} \right) \quad \text{with } x = \frac{2\pi(t-\phi)}{P}. \quad (2.128)$$

At the mean ionospheric height of 350 km the zenith angle  $z = \sin^{-1}(0.94798 \cos \epsilon)$ , where  $\epsilon$  is the unrefracted auxiliary elevation angle and the numerical  $0.94798 = a_e / (a_e + 350 \text{ km})$  with  $a_e = 6378.136$  km as the mean equatorial radius of the Earth. The geodetic latitude  $\phi_I$  and longitude  $\lambda_I$  of the sub-ionospheric point is computed using the auxiliary azimuth angle  $\sigma$  and the longitude  $\lambda_0$  of the receiving ground station

$$\phi_I = \sin^{-1}(\sin \phi_0 \sin(\epsilon + z) + \cos \phi_0 \cos(\epsilon + z) \cos \sigma) \quad (2.129)$$

$$\lambda_I = \lambda_0 + \sin^{-1} \left( \frac{\cos(\epsilon + z) \sin \sigma}{\cos \phi_I} \right). \quad (2.130)$$

As ionospheric properties are aligned with geomagnetic latitude rather than geographic latitude, the Klobuchar model is formulated in geomagnetic coordinates. The transformation from geodetic to geomagnetic latitude, assuming that the Earth's magnetic field can be represented by an Earth centered dipole, can be achieved by the following approximation (*Klobuchar* [1975]):

$$\Phi_I = \phi_I + 11.6^\circ \cos(\lambda_I - 291^\circ) . \quad (2.131)$$

The amplitude  $A$  and the period  $P$  can be computed from

$$A = A_0 + A_1\Phi_I + A_2\Phi_I^2 + A_3\Phi_I^3 \quad (2.132)$$

$$P = P_0 + P_1\Phi_I + P_2\Phi_I^2 + P_3\Phi_I^3 \quad (2.133)$$

The slant factor is used to convert into slant time and can be approximated by

$$\tau_{sl} = 1 + 2 \left( \frac{96 - \epsilon}{90} \right)^3 . \quad (2.134)$$

Thus, the ionospheric path delay in time is (*Klobuchar* [1975])

$$\Delta t_{iono} = \tau_{sl} \left( C + A \left( 1 - \frac{x^2}{2} - \frac{x^4}{24} \right) \right) . \quad (2.135)$$

The ranging delay is then

$$\Delta \rho_{iono}(t) = \Delta t_{iono} \cdot c . \quad (2.136)$$

The coefficients  $A_0, A_1, A_2, A_3$  of the amplitude  $A$  and  $P_0, P_1, P_2, P_3$  of the period  $P$  are available from <ftp://ftp.unibe.ch/aiub/CODE/> and are computed from daily measured global ionosphere maps (*Schaer S.* [1997]).

### 2.7.3.3 Comparison

In Figure 2.16 the frequency shifts for a two-way X-band downlink computed from the polynomial representation of the path delay provided by the TSAC group and from the Klobuchar model based on an ionospheric map for 1 March 2006 are shown. Obviously both corrections are in good agreement and can be used equivalently.

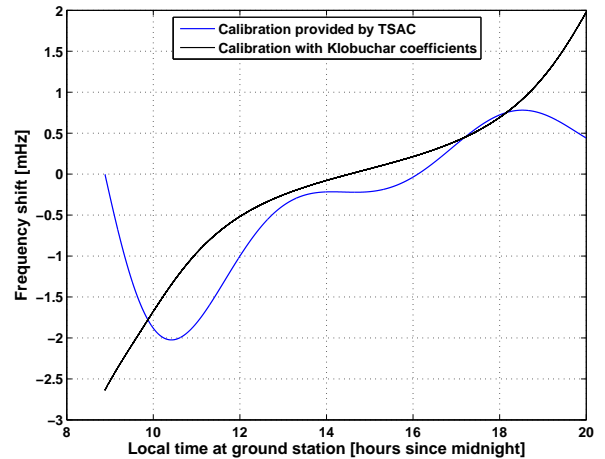


**Figure 2.16:** Comparison of the frequency shift for a two-way X-band downlink computed based on Klobuchar coefficients and ionospheric calibration files provided by TSAC for 1 March 2006

## 2.7.4 Frequency shift caused by the atmosphere of the Earth

The total frequency shift depending on the uplink frequency  $f_{up}$  and the transponder ratio  $k$  for a two-way recording can be computed according to Pätzold [2004] via:

$$\Delta f_{cal}(t) = f_{up}(t) \cdot \frac{1+k}{c} \cdot (\Delta\tau_{trop}(t) + \Delta\tau_{iono}(t)) \quad (2.137)$$

where

$$\Delta\tau_{trop}(t) = \frac{\phi_{trop}(t + \Delta t) - \phi_{trop}(t - \Delta t)}{\Delta t} \quad (2.138)$$

$$\Delta\tau_{iono}(t) = \frac{\phi_{iono}(t + \Delta t) - \phi_{iono}(t - \Delta t)}{\Delta t} \quad (2.139)$$

In this equation it is assumed that the elevation angle at the time, when the signal is transmitted from the ground station and when the signal is received at ground station equals. This is only true when the spacecraft is close to the ground station. However, for spacecraft like Rosetta (ROS) this is not true because of the large round trip light time  $t_\tau$ . Therefore, a formulation should be used in which the elevation angle at transmission and reception is treated separately

$$\begin{aligned} \Delta f_{cal}(t) = f_{up}(t) \frac{k}{c} & (\Delta\tau_{trop}(t) + \Delta\tau_{trop}(t - t_\tau) \\ & + \Delta\tau_{iono}(t) + \Delta\tau_{iono}(t - t_\tau)). \end{aligned} \quad (2.140)$$

In Figure 2.17 a comparison of the total frequency shift caused by the atmosphere of the Earth is shown firstly based on equation 2.137 and secondly on equation 2.140 for a measurement in X-band (8.4 GHz) for the ROS spacecraft on 5 September 2009. At the beginning of the recording (small elevation angles) a large difference between the corrections according to equations (2.137) and (2.140) can be seen. It decreases during the recording due to larger elevation angles which reduces the tropospheric correction. For higher accuracy equation (2.140) is used for the computation of the atmospheric correction in this thesis.

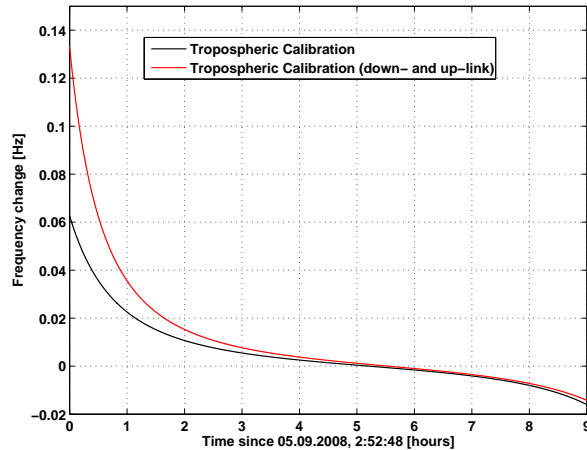


**Figure 2.17:** Comparison of the frequency correction for the atmosphere of the Earth in X-band (8.4 GHz) for the Rosetta spacecraft on 5 September 2009. The red line indicates the correction based on the more precise formulation according to equation (2.140) and the black line the correction based on a simplified model according to equation (2.137)

## 2.8 Orbit determination and parameter estimation

The equation of motion of a spacecraft contains parameter which need to be estimated from the measured data. For example, the initial state vector of the spacecraft, the scale factor for the solar radiation pressure or the core parameter of this thesis, the mass, and if possible other parameter of the gravity field of a body. This can be realized by a weighted least square estimation method. Applying this method means dealing with the inverse of matrix which may be ill-posed or contain unimportant parameter. The least square fitting method and numerical solutions for the problems are described in the following.

### 2.8.1 Weighted least squares estimation

The basic idea of least square estimation is to find the model parameter for which the square of the difference between the model data and the measured data becomes as small as possible. Assuming a vector consisting of  $m$  recorded data

$$\mathbf{d} = (d_1, d_2, \dots, d_m)^T$$

and a vector

$$\mathbf{x} = (x_1, x_2, \dots, x_n)^T$$

containing  $n$  free model parameters like the mass of the body. The model  $\mathbf{g}$  provides a link between the model parameters and observations:

$$\mathbf{g}(\mathbf{x}) = (g_1(\mathbf{x}), g_2(\mathbf{x}), \dots, g_m(\mathbf{x}))^T.$$

Here,  $g_i(\mathbf{x})$  is the value predicted by the model for observation  $d_i$ . The difference between the model data and the observation is then

$$\boldsymbol{\epsilon} = \mathbf{d} - \mathbf{g}. \quad (2.141)$$

In order to compute values of  $\mathbf{x}$  such that  $\mathbf{g}(\mathbf{x})$  matches  $\mathbf{d}$ , the partial derivatives of the model  $\mathbf{g}$  is expanded around  $\mathbf{x}$  in a Taylor series

$$\mathbf{g}(\mathbf{x} + \delta\mathbf{x}) = \mathbf{g}(\mathbf{x}) + \mathbf{J}\delta\mathbf{x} + \mathbf{R}(\mathbf{g}, \delta\mathbf{x}). \quad (2.142)$$

If the model function  $\mathbf{g}$  is linear it can be written as

$$\mathbf{g}(\mathbf{x} + \delta\mathbf{x}) = \mathbf{g}(\mathbf{x}) + \mathbf{J}\delta\mathbf{x}. \quad (2.143)$$

$\mathbf{J}$  is the  $(m \times n)$  Jacobian matrix also referred to as sensitivity matrix containing the partial derivatives of the model function

$$\mathbf{J} = \begin{pmatrix} \frac{\partial g_1}{\partial x_1} & \cdots & \frac{\partial g_m}{\partial x_1} \\ \vdots & \ddots & \vdots \\ \frac{\partial g_1}{\partial x_n} & \cdots & \frac{\partial g_m}{\partial x_n} \end{pmatrix} \quad (1 \leq i \leq m, 1 \leq j \leq n)$$

The partial derivatives in  $\mathbf{J}$  can be derived analytically for each parameter if an appropriate analytical function is available. The analytical expression of the partial derivatives can become very complex and the numerical implementation of the corresponding formulas is quite laborious and error prone. The rigorous computation can be replaced by a simple difference quotient approximation. With a symmetric differential quotient approximation

$$\frac{\partial g_i}{\partial x_j} = \frac{g(x_j + \Delta x_j) - g(x_j - \Delta x_j)}{2\Delta x_j}. \quad (2.144)$$

the partial derivatives are obtained which are correct up to second order in  $x_j$  (*Montenbruck and Gill [2000]*).

So far, all observations are treated equally, but the noise of measurements usually varies, i.e. the standard deviation  $\sigma_i$  is different. This difference can be accounted for by introducing an  $(m \times m)$  weight matrix (*Juup and Vozoff [1975]*)

$$\mathbf{W} = \text{diag}(\sigma_1^{-2}, \sigma_2^{-2}, \dots, \sigma_m^{-2}) = \begin{pmatrix} \sigma_1^{-2} & & 0 \\ & \ddots & \\ 0 & & \sigma_m^{-2} \end{pmatrix}. \quad (2.145)$$

Agreement between the measured data and the model data with respect to the model parameter can be found by minimizing

$$\begin{aligned} \mathbf{q}(\mathbf{x}) &= \|\boldsymbol{\epsilon} - \mathbf{J}\delta\mathbf{x}\|_{\mathbf{W}} = \\ &= \left( (\mathbf{d} - \mathbf{g}(\mathbf{x}) - \mathbf{J}\delta\mathbf{x})^T \mathbf{W} (\mathbf{d} - \mathbf{g}(\mathbf{x}) - \mathbf{J}\delta\mathbf{x}) \right)^{\frac{1}{2}} \end{aligned} \quad (2.146)$$

$$\Rightarrow \mathbf{q}^2(\mathbf{x}) = \boldsymbol{\epsilon}^T \mathbf{W} \boldsymbol{\epsilon} - 2\mathbf{J}^T \mathbf{W} \boldsymbol{\epsilon} \delta\mathbf{x} + \mathbf{J}^T \mathbf{W} \mathbf{J} \delta^2 \mathbf{x}. \quad (2.147)$$

Differentiation with respect to  $\mathbf{x}$  leads to

$$\delta\mathbf{x} = (\mathbf{J}^T \mathbf{W} \mathbf{J})^{-1} \mathbf{J}^T \mathbf{W} \boldsymbol{\epsilon}. \quad (2.148)$$

This formulation can be used to estimate in an iterative process a new model with new parameter from the change  $\delta\mathbf{x}$  in order to minimize the difference between measured data and model data (*Juup and Vozoff [1975]*, *Aster et al. [2005]*).

### 2.8.2 Singular value decomposition

The inverse of the matrix  $(\mathbf{J}^T \mathbf{W} \mathbf{J})$  in equation 2.148 can be computed numerically using Singular Value Decomposition (SVD). The SVD for an  $(m \times n)$  matrix  $\mathbf{A}$  with rank  $p \leq \min(m, n)$  is denoted by

$$\mathbf{A} = \mathbf{U} \mathbf{S} \mathbf{V}^T = \sum_{i=1}^n s_i \mathbf{u}_i \mathbf{v}_i^T, \quad (2.149)$$

where  $\mathbf{U}$  is an  $(m \times m)$  and  $\mathbf{V}$  an  $(n \times n)$  matrix.  $\mathbf{U}$  and  $\mathbf{V}$  are orthogonal matrices

$$\mathbf{U}^T \mathbf{U} = \mathbf{I}_m \quad (2.150)$$

$$\mathbf{V}^T \mathbf{V} = \mathbf{I}_n. \quad (2.151)$$

$\mathbf{S}$  is an  $(m \times n)$  diagonal matrix where each diagonal element  $s_i$  is the non-negative square root of an eigenvalue of  $\mathbf{A}^T \mathbf{A}$ . The pseudo inverse of  $\mathbf{A}$  can now be computed via

$$\mathbf{A}^{-1} = \mathbf{V} \mathbf{S}^{-1} \mathbf{U}^T = \sum_{i=1}^n \frac{\mathbf{v}_i \mathbf{u}_i^T}{s_i}, \quad (2.152)$$

with the so called singular values  $s_i$

$$s_i^{-1} = \begin{cases} \frac{1}{s_i} & \text{if } s_i > 0 \\ 0 & \text{if } s_i = 0. \end{cases} \quad (2.153)$$

For numerical purposes this formulation is not appropriate because  $s_i$  will not be exactly zero and therefore the inversion will be instable. Additionally very small values of  $s_i$  would produce very large values of  $s_i^{-1}$ . For this reason the change of the respective parameter would be overestimated and result in wrong parameter estimation or divergence of the iteration process. A method to solve this problem will be explained in the next section.

### 2.8.3 Damping factor

The numerical values of  $s_i$  can lead to ill-posedness through irrelevant parameter (zero singular values of  $\mathbf{A}$ ), and unimportant parameters (small singular values of  $\mathbf{A}$ ). One way would be to omit terms with small singular values. This would stabilize the solution in the sense that it would make the result less sensitive to data noise. But this would also reduce the resolution and the model estimation would no longer be unbiased.

The problem can be solved by introducing a damping factor  $\alpha$ . Equation 2.148 becomes then

$$\delta \mathbf{x} = (\mathbf{J}^T \mathbf{W} \mathbf{J} + \alpha^2 \mathbf{I})^{-1} \mathbf{J}^T \mathbf{W} \boldsymbol{\epsilon}. \quad (2.154)$$

The damping factor  $\alpha$  can be obtained from the Eigenvalues of the Jacobian matrix  $\mathbf{J}$  according to *Aster et al.* [2005] via

$$\alpha = \max \left( \text{eig} \left( (\mathbf{J}^T \mathbf{W})^{-1} \right) \right).$$

This numerical method provides a stable weighted least square estimation algorithm which can be used to determine the parameter of a model to be fitted to recorded data within an iterative process.

#### 2.8.4 Error estimation

The recordings from Radio Science measurements are affected by measurement errors. These errors influence the uncertainty of the estimated parameter. The covariance matrix  $\mathbf{P}$  contains the estimates for the closeness of the model with the measurement data and is defined as (*Vallado* [2001])

$$\mathbf{P} = (\mathbf{J}^T \mathbf{W} \mathbf{J})^{-1} = \begin{pmatrix} \sigma_{11}^2 & \cdots & \mu_{1i} \sigma_1 \sigma_i & \cdots & \mu_{1n} \sigma_1 \sigma_n \\ \vdots & \ddots & & & \vdots \\ \mu_{i1} \sigma_i \sigma_1 & & \sigma_{ii}^2 & & \mu_{in} \sigma_i \sigma_n \\ \vdots & & & \ddots & \vdots \\ \mu_{n1} \sigma_n \sigma_1 & \cdots & \mu_{ni} \sigma_n \sigma_i & \cdots & \sigma_{nn}^2 \end{pmatrix} \quad (2.155)$$

with the Jacobian matrix  $\mathbf{J}$  and the weight matrix  $\mathbf{W}$  as defined above. The diagonal terms are the variances  $\sigma_{ii}^2$  of the estimate and the square root of the variances are the sample standard deviations  $\sigma_{ii}$  of each estimated parameter. The 95% confidence interval, i.e.  $1 \sigma$  of the parameter  $x_i$  is (*Aster et al.* [2005])

$$\Delta x_i = \pm 1.96 \cdot \sqrt{\mathbf{P}_{ii}} \quad (2.156)$$

The factor 1.96 results from

$$\frac{1}{\sigma \sqrt{2\pi}} \int_{-1.96\sigma}^{1.96\sigma} e^{-\frac{x^2}{2\sigma^2}} dx \approx 0.95. \quad (2.157)$$

The off-diagonal elements of  $\mathbf{P}$  are called covariance terms. They contain the correlation coefficients  $\mu_{ij}$  representing the degree of correlation among the estimated parameter. Zero indicates no correlation, positive signs a direct correlation, while negative signs imply an inverse relationship. The correlation should be zero or, at least, very small (*Brandt* [1998], *Montenbruck and Gill* [2000]).

## 2.9 Noise reduction filter

The uncertainty in the parameter estimated from the recorded data increases with the noise of the data. Applying digital filters can be used to reduce the noise. In the following only a brief introduction into digital filter is given, a detailed description would go beyond the scope of this work. In addition, the filters which are used in this work and the method for selection of the filter are explained.

### 2.9.1 Noise sources

The noise of the data recorded at the ground station is generated mostly by the following sources (*Pätzold et al.* [2004]):

- Thermal noise essentially by the receiver of the ground station, but also from the transponder onboard the spacecraft.
- Instrumentation errors like quantization errors or reference instability.
- The troposphere and ionosphere of the Earth, and the interplanetary plasma. These contributions are modeled and subtracted from the recorded data, but not all contributions can be removed entirely (see section 2.7).

The velocity error  $\sigma_v$  due to the thermal noise of the receiver at the ground station is given by

$$\sigma_v = \frac{c}{4\pi f \Delta t} \sqrt{\frac{2BN_0}{C}} \quad (2.158)$$

and the phase noise  $\sigma_\phi$  of the transponder by (*Pätzold et al.* [2004])

$$\sigma_\phi = \frac{c\sqrt{2}}{4\pi ft} \sigma_v. \quad (2.159)$$

$c$  is the speed of light,  $f$  the frequency,  $\Delta t$  the sample time,  $B$  the receiver bandwidth,  $C$  and  $N$  the received carrier power and the noise power density, respectively. The transponder phase noise  $\sigma_\phi$  was experimentally determined by *Remus et al.* [2001] for Mars Express and Rosetta with a transponder electrical qualification model on ground. A summary of the Doppler velocity errors at different distances is given in Table 2.2. The total error in X-band in two-way coherent mode of 0.26 mm/s corresponds to an error of 14.6 mHz referring to a downlink frequency of 8.4 GHz.

More information about noise sources during Radio Science measurements is given in *Yuen* [1983] and more detailed information for MEX and ROS can be found in *Pätzold* [2003], and *Pätzold* [2006], respectively.

	at 0.8 AU		at 2.5 AU	
	S-Band	X-Band	S-Band	X-Band
Thermal noise (ground station) [mm/s]	0.90	0.01	2.00	0.03
Transponder phase noise [mm/s]	0.42	0.26	0.42	0.26
Total error [mm/s]	0.99	0.26	2.04	0.26

**Table 2.2:** The Doppler velocity error in two-way coherent mode at different distances for Mars Express and Rosetta at 1 sec integration time (Pätzold et al. [2004]).

## 2.9.2 Digital filters

The noise of a measurement can be reduced by applying filter. In general, a filter can be considered as a transfer function between any input function  $x(t)$  and the according output function  $y(t)$ . Here, digital filters are used, i.e. filtering is applied numerically. The discrete input sequence

$$x(t) = x_n = x(n\Delta t) \quad n = 0, 1, 2, \dots, N - 1, \quad (2.160)$$

with a time interval  $\Delta t$  and  $N$  samples is related to the output sequence  $y_n$  in the time domain via the discrete convolution

$$y(t) = y_n = \sum_{j=0}^{N-1} h_j x_{n-j}. \quad (2.161)$$

In the time domain, digital filters are characterized by the discrete impulse response function  $h_n$  and in the frequency domain by its discrete Fourier transformation, the discrete frequency response function  $H_k$ . The input to output relation is according to the convolution theorem in the frequency domain

$$Y_k = H_k X_k. \quad (2.162)$$

The discrete input function  $x(t)$  is in the frequency domain using the discrete Fourier transformation

$$X(f) = X(\Delta f k) = X_k = \Delta t \sum_{n=0}^{N-1} x_n e^{-i2\pi k \Delta f n \Delta t}, \quad (2.163)$$

were the frequency  $f = k\Delta f$  and the sample frequency  $\Delta f = \frac{1}{T} = \frac{1}{N\Delta t}$ . Replacing  $f$  with the new variable (Häusler [2008a])

$$z = e^{-i2\pi k \Delta f \Delta t} \quad (2.164)$$

results in the  $z$ -transform of the discrete input function

$$\mathcal{Z}(x_n) = X(z) = \Delta t \sum_{n=0}^{N-1} x_n z^n. \quad (2.165)$$

The sum on the right side is the  $z$ -transform of  $x(t)$ . The discrete convolution of two sequences can be realized by the product of their  $z$ -transforms (*Buttkus* [2000]). Therefore equation (2.162) reads then in the  $z$  domain

$$Y(z) = H(z)X(z). \quad (2.166)$$

The most important class of digital filters are filters where the transfer function  $H(z)$  can be written as the ratio of two polynomials in  $z$ :

$$H(z) = \frac{\sum_{k=k_0}^M a_k z^k}{\sum_{k=0}^L b_k z^k}, \quad \text{with } b_0 = 1. \quad (2.167)$$

It follows from the input to output relation (2.166) in the  $z$  domain

$$\begin{aligned} (1 + b_1 z + b_2 z^2 + \dots + b_L z^L) Y(z) = \\ (a_{k_0} z^{k_0} + a_{k_0+1} z^{k_0+1} + \dots + a_M z^M) X(z). \end{aligned} \quad (2.168)$$

Using that  $X(z)z^k$  is the  $z$  transform of the time series  $(x_{j-k})$  it can be transformed to

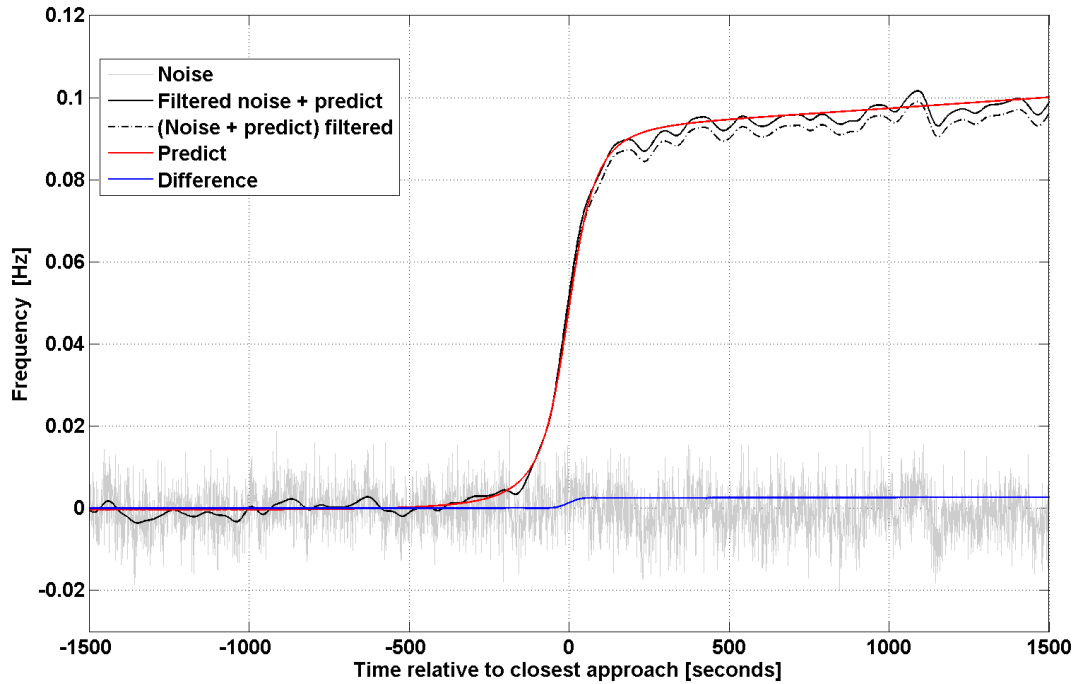
$$\begin{aligned} (y_n) + b_1(y_{n-1}) + \dots + b_L(y_{n-L}) = \\ a_{k_0}(x_{n-k_0}) + a_{k_0+1}(x_{n-k_0-1}) + \dots + a_M(x_{n-M}). \end{aligned} \quad (2.169)$$

Therefore the following recursive filter equation is fulfilled at any time  $n$

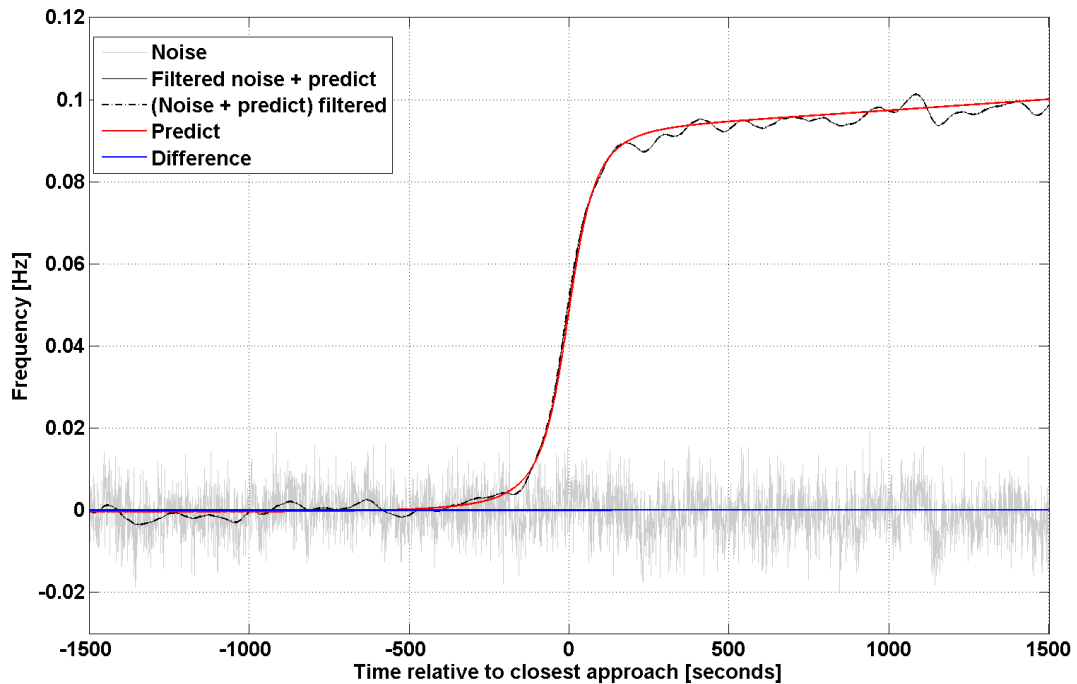
$$\begin{aligned} y_n = & a_{k_0}(x_{n-k_0}) + a_{k_0+1}(x_{n-k_0-1}) + \dots + a_M(x_{n-M}) \\ & - b_1(y_{n-1}) - \dots - b_L(y_{n-L}). \end{aligned} \quad (2.170)$$

The filter can be classified with regard to the coefficients  $b_k$  in equation (2.167). For nonrecursive filters of finite length all  $b_k$  are all equal to zero for  $k \geq 1$ .  $H(z)$  is then a polynomial with zeroes, but without poles. If one of the coefficients  $b_k$  is not equal to zero for  $k \neq 0$ , the filter is recursive (*Buttkus* [2000]).

Filters can also be distinguished by their phase response into Zero phase filters having a frequency response that has a phase which is composed entirely of zeroes, and the frequency response of linear phase filters and nonlinear phase filters having linear and nonlinear phases, respectively. Zero phase can be achieved by combining forward and reverse filtering, i.e after filtering in the forward direction, then filtering again in the reverse direction. The result has then a frequency response with zero phase (*Smith* [1998]).



(a) Kaiser window filtering with cut-off frequency  $f_c = 15$  mHz



(b) Kaiser window filtering with cut-off frequency  $f_c = 47$  mHz

**Figure 2.18:** Comparison of applied filters. The used data are from the Phobos flyby in July, 2008. Here different cut-off frequencies for the Kaiser window are used. In the figure above the filter reduces not only the noise but also the frequency shift caused by the gravity field of Phobos, indicated by the blue line, i.e. the difference between  $f_n$  and the filtered noise  $\check{f}_n$ . In the figure below only the noise is reduced because  $|f_n - \check{f}_n|$  is approximately zero.

### 2.9.3 Appropriate filter

Not all digital filters are useful for every type of measurement. The filter with its specific configuration parameter should reduce only the noise of the data and leave the frequency change caused by the gravity field of the perturbing body unmodified. This frequency change is different for every measurement. For this reason the parameter of the selected filter has to be defined for each measurement separately.

*Stiffel* [2008] tested different filters in order to find the best filter with specific configuration parameters for each performed flyby. Hence predicted frequency changes  $f_p$  are generated and real noise  $f_n$  from a measurement is added. The filter is then applied to the noisy predicted frequency changes  $f_{pn} = f_p + f_n$  and in addition to the noise  $f_n$  only. Subtracting from the filtered noisy predicted frequency changes the predicted frequency changes only filtered noise  $f_n$  remains. The difference between  $f_n$  and the filtered noise  $\check{f}_n$  indicates the quality of the filter. Defining a limit  $f_l$  according to the measurement accuracy, the filter reduces only the noise if  $|f_n - \check{f}_n|$  is smaller than  $f_l$ . If  $|f_n - \check{f}_n|$  is larger than  $f_l$ , the filter reduces the noise but changes also the frequency shift caused by the gravitational attraction of the perturbing body, i.e.

$$\left| \underbrace{filt(f_{pn}) - f_p}_{f_n} - \underbrace{filt(f_n)}_{\check{f}_n} \right| \begin{cases} < f_l & \Rightarrow \text{only noise reduced} \\ \geq f_l & \Rightarrow f_p \text{ also modified.} \end{cases} \quad (2.171)$$

Figure 2.18 shows two examples for the result of the above described method. The applied filter was a Kaiser window with two different cut-off frequencies  $f_c$ . The cut-off frequency defines the bandwidth of the filter. In Figure 2.18(a) the selected cut-off frequency of 15 mHz seems to be too small and not only noise is reduced but also the frequency change caused by the perturbing body is modified. The resulting mass estimate would be falsified. In Figure 2.18(b) the ideal cut-off frequency is selected which can be seen by the nearly zero difference (indicated by the blue line) between  $\check{f}_n$  and  $f_n$ .

*Stiffel* [2008] found out with this method that a Kaiser window filter and a moving average filter applied consecutively reducing most of the measurement noise.

The Kaiser window filter is defined (*Buttkus* [2000])

$$w(k) = \begin{cases} \frac{I_0\left(\alpha\sqrt{1-\frac{2k}{(N-1)^2}}\right)}{I_0(\alpha)} & \text{if } |k| \leq \frac{N-1}{2} \\ 0 & \text{if } |k| > \frac{N-1}{2}, \end{cases} \quad (2.172)$$

with  $N$  the number of data points,  $k = 1, 2 \dots N$ , and the Bessel function  $I_0(\alpha)$  of zeroth order

$$I_0(\alpha) = 1 + \sum_{k=1}^{\infty} \left( \frac{\left(\frac{\alpha}{2}\right)^{2k}}{k!} \right)^2. \quad (2.173)$$

The parameter  $\alpha$  changes the amplitude of the side lobes and the transition bandwidth.

The moving average filter is defined by

$$y(n) = \frac{1}{M} \sum_{k=0}^{M-1} x(n-k), \quad (2.174)$$

with  $n$  the current time at which the value should be calculated and  $M$  the length of the time interval used for averaging (*Buttkus* [2000]).

For the analysis of the measured data from close flybys only these two filters are used. Both filters are applied consecutively in forward and reverse direction ensuring a zero phase.

The limit  $f_l$  needed to define the cut-off frequency  $f_c$  of the Kaiser window filter and the time interval  $M$  of the moving average filter is computed from the sensitivity  $GM_s$ . The sensitivity is estimated from an upper and lower limit of the mass value and the resulting upper and lower limit of the amplitude of the frequency change caused by the gravitational attraction of the mass, i.e.

$$GM_s = \frac{GM_{up} - GM_{low}}{f_{up} - f_{low}} = \frac{\Delta GM}{\Delta f} \quad (2.175)$$

This method ensures that the used filter technique only reduces the noise level and does not eliminate any information about the mass of the body in the measured data. Applying these filters with a priori estimated configuration parameters decreases the standard deviation of the measurement noise at least by a factor of 3 (*Stiffel* [2008]).

---

## Doppler accuracy and curve fitting

---

As described in the previous sections the method in this thesis for estimating gravitational parameter of a solar system body from Radio Science measurements is based on the difference between the received frequency at the ground station  $f_{mes}$  and a predicted frequency  $f_{pre}$ . This frequency is based on the hypothetical unperturbed orbit of the spacecraft, all necessary forces are taken into account except the force which perturbs due to the gravitational attraction of the body. When subtracting the frequency shift  $f_{atm}$  if the signal propagates through the Earth atmosphere, only the residual frequency shift  $f_{res}$  due to the perturbing body remains

$$f_{res} = f_{mes} - f_{pre} - f_{atm} . \quad (3.1)$$

Radio Science observations without any perturbation due the gravitational attraction of Phobos are used to determine  $f_{res}$ , i.e. the accuracy of the used models. The frequency residuals are not equaling zero, but all used observations having small offsets in the order of a few tenth of mHz typically between 10 mHz and 20 mHz at X-band (8.4 GHz). This is in the order of the Doppler velocity error due to thermal noise at the ground station and transponder phase noise of 0.26 mHz  $\equiv$  14.6 mHz at X-band in two way mode. In Figure 3.1 typical frequency residuals  $f_{res}$  from three measurements illustrating these offsets. These measurements have mean offset values of 15.2 mHz, -8.9 mHz and -6.7 mHz, respectively. It can be seen that the frequency residuals are not constant offsets, i.e. they are having change rates or slopes. The three measurements in Figure 3.1 showing slope values of 1.8 mHz/h, 0.6 mHz/h and 4.9 mHz/h, respectively.

The same is true for close flybys, i.e.  $f_{res}$  contains usually not only the frequency shift due to the perturbing body but also uncertainties due to the choice of the initial state vector, the scale factor of the solar radiation pressure and measurement noise caused by thermal noise or systematic errors. In Figure 3.2 the theoretical frequency shift  $f_{the}$

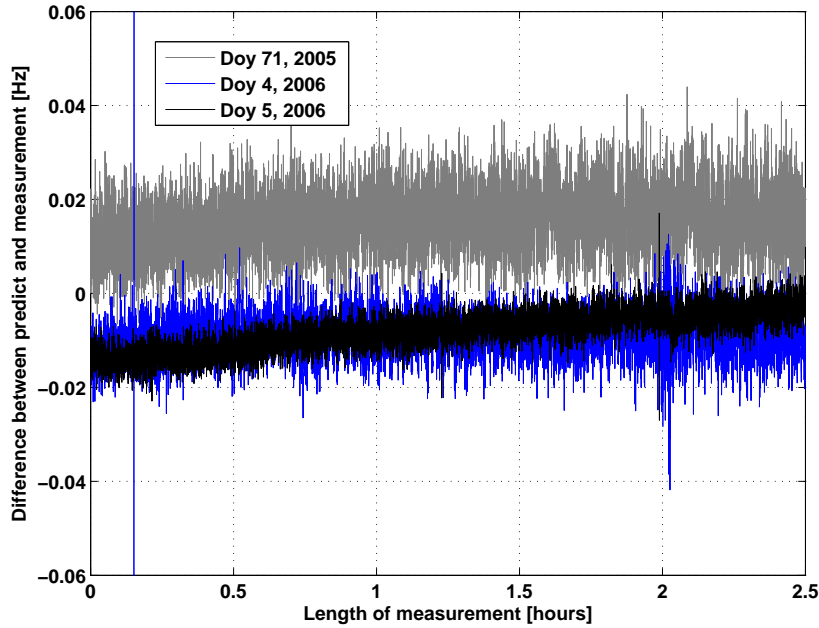


**Figure 3.1:** *Difference between predicted and measured frequency for three measurements.*

(blue line) and the true frequency shift of the first guess for the Phobos flyby in 2008 is shown. The initial state vector is taken from the orbit SPICE kernels of MEX provided by ESOC, the scale factor for the solar radiation pressure is  $k = 1.3$  and the mass of Phobos was assumed  $GM = 0.712 \times 10^{-3} \text{ km}^3/\text{s}^2$ .

Obviously, both measured and predicted frequency shift are not aligned. But for a precise estimate of the gravitational parameter of the perturbing body it must be ensured that the constant offset and the linear trend at the beginning of the measurement when the gravity field of Phobos does not significantly effect the frequency equals zero as it is for the predicted frequency shift in this time range.

Therefore the constant offset is introduced as a fitting parameter to ensure that the first data points of  $f_{res}$  and of  $f_{the}$  are aligning. The constant offset accounts for the uncertainty in the initial position of the spacecraft because only information about the velocity can be obtained from Doppler data. The initial velocity of the spacecraft taken from the orbit SPICE kernels as a first guess is therefore considered as a fitting parameter and estimated during the fitting process. The same is done for the scale factor of the solar radiation pressure. Both fitting parameter ensure that the linear drift caused by the uncertainty in the initial values will vanish.

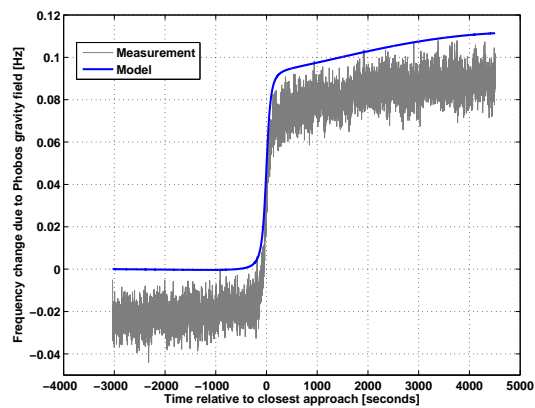


**Figure 3.2:** *First guess frequency residuals of the Phobos flyby in 2008. The blue line indicates the predicted frequency shift due to the gravity field of Phobos ( $GM = 0.712 \times 10^{-3} \text{ km}^3/\text{s}^2$ .) and the gray line the frequency residuals  $f_{res}$ .*

---

## Physical properties of the target bodies

---

The ESA Rosetta (ROS) spacecraft performs during the journey to its main target 67P Churyumov-Gerasimenko the flyby of two main belt asteroids: 2867 Steins, visited in September 2008, and 21 Lutetia, whose flyby is scheduled for July 2010. The flyby at Steins is analyzed and for the Lutetia flyby feasibility studies are done and shown in the next chapter. The Mars Express spacecraft has also performed flybys at the Martian moon Phobos which are also analyzed and the results are shown and interpreted in the next chapter. Therefore in the following the physical parameter of the bodies are given.

### 4.1 The asteroid 2867 Steins

The asteroid 2867 Steins was discovered in 1969 by N. S. Chernykh. It is classified as a member of the main asteroid belt and is orbiting the Sun in a perihelion distance of about 2.018 AU, a semi major axis of about 2.363 AU and with inclination of 0.146 in 3.63 years (*JPL* [2009]).

The size of Steins was estimated using images (see Figure 4.1) from the imaging instrument OSIRIS (Optical, Spectroscopic, and Infrared Remote Imaging System) onboard ROS. The mean radius of Steins is  $2.7 \pm 0.3$  km, the volume is  $78 \pm 30$  km<sup>3</sup> by constructing a 3-dimensional shape model from the images taken at the flyby in September 2008 (*Besse et al.* [2009]). The dimension of Steins have been determined to be  $5.73 \pm 0.52$ ,  $4.95 \pm 0.45$ , and  $4.58 \pm 0.41$  km from ground based measurements (*Lamy et al.* [2008]).

Three different types of craters were observed on the surface of Steins (Fig. 4.1). Small craters are randomly distributed. A chain of craters at the top of the asteroid

and one large crater of 2.5 km diameter are approximately 43% of the largest axis of Steins (*Burchell and Leliwa-Kopystynski* [2009]).

The spectra of Steins obtained from a ground based observational campaign shows the typical behavior of E-type asteroids, in particular of the E[II] subgroup. The spectrum is usually attributed to sulfides like troilite and oldhamite. It was also concluded from the observations that Steins has a quite homogeneous surface composition (*Dotto et al.* [2009]).



**Figure 4.1:** Asteroid Steins seen from a distance of 800 km, taken by the OSIRIS imaging system on board ROS from two different perspectives (Source: <http://www.esa.int/esa-mmng/mmng.pl?b=b&type=I&mission=Rosetta&start=1>).

## 4.2 The asteroid 21 Lutetia

The main belt asteroid 21 Lutetia was discovered on November 15, 1852 by Herman Mayer Salomon Goldschmidt at the observatory of Paris. The spectral classification of Lutetia ranges from M-type to C-type (*Birlan et al.* [2004]) and all available information about Lutetia suggests a primitive composition. Some of the physical parameters of Lutetia are summarized in the following Table.

Parameter	Lutetia
Taxonomic type	C (M)
Albedo	$0.221 \pm 0.20$
Diameter [km]	$95.5 \pm 4.1$
Density [ $\frac{\text{g}}{\text{cm}^3}$ ]	$2.0 \pm 1.0$
Semimajor axis [AU]	2.435
Eccentricity	0.164
Inclination [deg]	3.064
Synodical rotation period [h]	$8.17 \pm 0.01$

**Table 4.1:** Summary of the physical parameters of the asteroid Lutetia. Values are taken from *Barucci et al.* [2005] and *Müller et al.* [2006] except for the density values which are assumed values based on the taxonomic type.

## 4.3 The Martian moon Phobos

Asaph Hall discovered 1877 the two moons of Mars, Phobos and Deimos. Phobos is the larger of the two Martian moons. The first pictures from Phobos were taken from Mariner 9 in 1971. Subsequent missions expanded the knowledge of Phobos but there are still some questions remaining unsolved. In the following the current knowledge is summarized for later interpretation based on the results obtained from close flybys of Mars Express (MEX).

### 4.3.1 Shape, topography and volume

Phobos is irregularly shaped and because of its small size not able to form a uniform sphere by its self gravity. The shape of Phobos can be described as an ellipsoid with principal axis  $a = 13.4 \pm 0.5$  km,  $b = 11.2 \pm 0.5$  km and  $c = 9.2 \pm 0.5$  km (*Seidelmann et al.* [2001]). The surface is covered by a large number of impact craters. The largest feature on the surface is the Stickney crater (Fig. 4.3) with a diameter of approximately 10 km.

The surface shows some grooves (Fig. 4.2) with a width of 100 - 200 m, a maximum depth of 30 m and a maximum length 20 km (*Thomas et al.* [1992]). The grooves can be grouped into 12 families of different ages. The grooves seem to be chains of secondary impacts formed from Mars impact ejecta (*Murray et al.* [2006]).



**Figure 4.2:** Grooves on the surface of Phobos (Source: <http://www.esa.int/esa-mm/mmg.pl?topic=&subtopic=&subm1=GO&keyword=Phobos>)

*Duxbury* [1989] and *Duxbury and Callahan* [1989] developed a model for the shape of Phobos based on a spherical harmonic expansion to degree and order six using a control network of surface features. This model was later expanded by *Duxbury* [1991] using a spherical harmonic expansion to degree and order eight. Corrections by analytical expressions for the Stickney crater and additional craters have been applied. The resulting volume is computed to  $5680 \pm 250$  km<sup>3</sup> (*Duxbury* [1991]).

*Thomas* [1993] developed a numerical shape model of Phobos using both limb and stereogrammetric data from Mariner 9 and Viking Orbiter achieving a volume of  $5748 \pm 190$  km<sup>3</sup>.

A new control point network for Phobos was recently established by *Willner et al.* [2009] from image data obtained by the Super Resolution Channel (SRC) of MEX. It

includes 665 surface control points and a spherical harmonic function model to degree and order 17 was derived. The volume was computed from the model to  $5689.8 \pm 60$  km<sup>3</sup>. This volume estimate shows a considerable small error compared to the previous volume estimates from *Duxbury* [1991] and *Thomas* [1993] and is used for density estimations in section 5.1.2.



**Figure 4.3:** The Stickney crater and other surface features of Phobos (Source: <http://www.esa.int/esa-mm/mmg.pl?topic=&subtopic=&subml=GO&keyword=Phobos>)

### 4.3.2 Mass

There is a long history of the mass estimation of Phobos. In February 1977 the Viking Orbiter I (VOI) performed 17 close flybys with closest approach distances from 80 km to 350 km. Different mass estimates have been achieved using this tracking data (*Christensen et al.* [1977], *Tolson et al.* [1977], *Tolson et al.* [1978], *Williams et al.* [1988]). The results from this estimates vary over a broad range (see Table 4.2).

The Phobos 2 mission was inserted into a quasi-satellite orbit around Phobos on 21 March 1989 and rendezvoused with Phobos, flying within 500 km to Phobos for 22 orbits until 27 March 1989. The tracking data sets from these flybys were analyzed by *Kolyuka et al.* [1990] and resulted in a mass estimate with a very small error bar (see Table 4.2). No information is available about how the formal error has been estimated. It is not clear in which way the data have been analyzed. MEX is the first spacecraft since the flybys from the Phobos 2 mission which is able to perform close flybys (distances below 500 km) at Phobos.

The reanalysis of the VOI and Mariner 9 (M9) tracking data are done by *Smith et al.* [1995] using distant encounters only. The derived value seems to be vary low compared to results from the close flybys.

On November 7, 1996, Mars Global Surveyor (MGS) was launched from Cape Canaveral and inserted into its orbit around Mars in September 1997. The orbit of MGS was nearly circular with an periapsis altitude of 380 km (*Yuan et al.* [2001]). A new gravity model for Mars was derived using VOI, Viking Orbiter II (VOII), M9 and MGS radiometric tracking data to degree and order 85. The mass of Phobos and Deimos were adjusted simultaneously with the gravity coefficients of Mars (*Yuan et al.* [2001]).

Based on the larger database of tracking data, i. e. 6 years of MGS and 3 years of Mars Odyssey (ODY), a higher degree and order Mars gravity field was estimated by *Konopliv et al.* [2006] (see section 2.5) and the mass of Phobos and Deimos are estimated in the global solution of the gravity field of Mars. The flyby data from VOI were reprocessed with this latest model for the orientation and gravity of Mars.

The latest estimate of the mass of Phobos was derived by *Rosenblatt et al.* [2008] using radio tracking data from MEX over the period of 2004 to 2006. In this work the tracking data were used to fit a model of the MEX motion. The mass of Phobos and Deimos were also estimated based on an improved model of the ephemerides of both moons.

The results of all mass estimates are summarized scaled to the formal error of one standard deviation in Table 4.2. The latest mass estimates of Phobos are all based on distant encounters. All estimates from distant encounters show extremely small errors which are driven statistically by the number of used tracking data.

GM [ $10^{-3} \frac{\text{km}^3}{\text{s}^2}$ ]	Data	Referenz
0.66±0.08	4 VOI flybys in 90 - 220 km	<i>Christensen et al.</i> [1977]
0.73±0.07	11 VOI flybys in 90 -220 km	<i>Tolson et al.</i> [1977]
0.66±0.04	17 VOI flybys in 80 - 300 km	<i>Tolson et al.</i> [1978]
0.85±0.07	8 VOI flybys in 100 - 209 km	<i>Williams et al.</i> [1988]
0.722±0.005	Phobos 2 orbiting within 500 km, 22 orbits	<i>Kolyuka et al.</i> [1990]
0.587±0.033	M9, VOI and VOII distant encounters	<i>Smith et al.</i> [1995]
0.7138±0.0005	M9, VOI, VOII and MGS	<i>Yuan et al.</i> [2001]
0.716±0.00005	MGS and ODY, VOI flybys (90 - 200 km)	<i>Konopliv et al.</i> [2006]
0.711±0.0002	MEX tracking data	<i>Rosenblatt et al.</i> [2008]

**Table 4.2:** Previous mass estimates of Phobos. The formal uncertainties correspond to one standard deviation. No information about the formal error is available for *Kolyuka et al.* [1990], *Williams et al.* [1988], *Tolson et al.* [1977] and *Christensen et al.* [1977].

### 4.3.3 The Orbit of Phobos

Phobos is located at a distance of  $\sim 2.8$  Mars radii ( $R_M$ ) from the center of Mars and within the synchronous orbit of  $\sim 5.9 R_M$ , along which the mean motion  $n$  of a satellite is equal to the planetary spin period  $\Omega$ . The orbit of Deimos is beyond the synchronous position at a distance of about  $\sim 6.9 (R_M)$ . The tidal bulge caused by the tidal forces raised on Mars by Phobos ( $n > \Omega$ ) lags the inner satellites position. It exerts thereby a retarding torque on the satellite and causes Phobos spiraling towards Mars. The tidal force in case of Deimos ( $n < \Omega$ ) pulls it forward and therefore Deimos is spiraling away. Phobos and Deimos are on nearly circular equatorial orbits. The rotation has been synchronized with their orbits by tidal forces (*Veverka and Burns [1980], Peale [2007]*).

The accuracy of the ephemerides has increased in the last years due to a lots of tracking data from spacecrafts orbiting Mars. It was found from SRC measurement onboard MEX that there are inconsistencies in the orbit predictions of Phobos which resulted in offsets of 12 km and -2 km in along track direction and  $\pm 1$  km and  $\pm 8$  km in across track direction in the models provided by JPL and ESOC, respectively (*Oberst et al. [2006]*).

New ephemerides have been computed based on new observations. *Lainey et al. [2007]* used earth-based and spacecraft observations from 1877 to 2005 with an accuracy of roughly 1 km. This error seems to be small compared to other solutions. It is not explained in detail how this error was estimated. *Willner et al. [2008]* used astrometric measurements on the basis of 69 SRC images obtained from 28 close flybys from MEX performed between 2004 and 2007. It was reported that Phobos is ahead of its predicted position along track of 1.5 - 2.6 km. The latest ephemeris provided by *Jacobson [2008]* includes also recent Earth-based and MEX observations and the one sigma ephemeris error is computed to be  $\pm 2$  km in the radial and out-of-plane directions and  $\pm 5$  km in the in-orbit direction.

Figure 4.4 shows a comparison between the ephemerides from *Lainey et al. [2007]* and *Jacobson [2008]* based on SPICE kernels `lainey_pho_dei.bsp` and `MAR080S.BSP` both available from *NAIF [2009]*. There is no SPICE kernel available referring to *Willner et al. [2008]*. The SPICE kernel (`MAR033_HRSC_V03.BSP`) refers to *Oberst et al. [2006]* and is less accurate ( $\pm 3$  km in radial and out-of-plane direction and  $\pm 15$  km in-orbit direction). The comparison between the latest models are shown in Figure 4.4 and it is obviously that both models are in agreement within their errors.

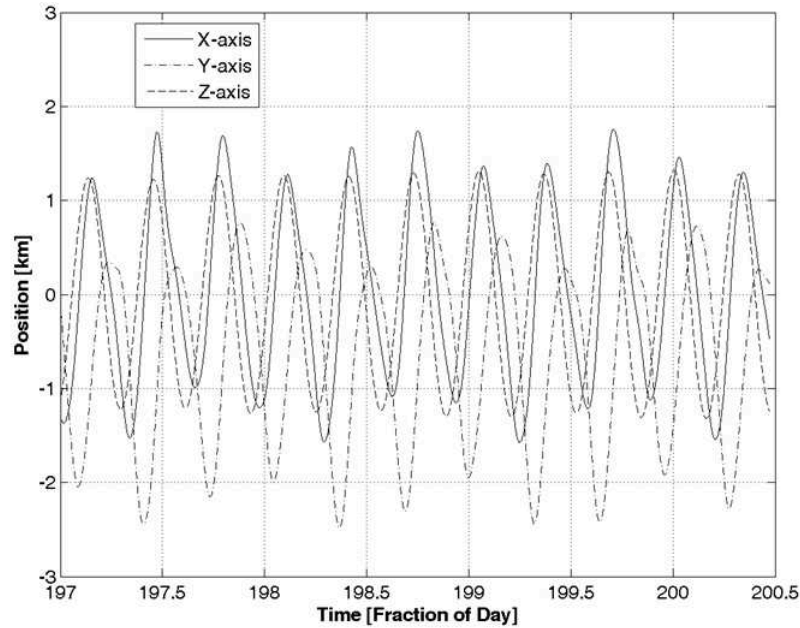


**Figure 4.4:** Comparison of Phobos ephemerides from Lainey et al. [2007] and Jacobson [2008] for a time period of 3.5 days around the flyby in July 2008.

#### 4.3.4 Spectral properties

Although there are numerous surface spectra of Phobos obtained from different spacecrafts and from ground based measurements with different wavelengths, it was not possible to draw a consistent picture of the surface composition. A summary of most spectral measurements of Phobos is given in Table 4.4. Early measurements from Mariner 9 (M9) and the Viking Lander 2 (VL2) compared the spectra with the C-type asteroids Ceres and Pallas but also with laboratory spectra of carbonaceous chondrites and basalts. Similarities between the spectra of carbonaceous chondrites and with the C-type asteroids were found. From this comparison it was concluded that Phobos is a captured C-type asteroid (Pang et al. [1978], Pollack et al. [1978]). But this measurements were limited by the spectral range and by incomplete coverage of the surface of Phobos.

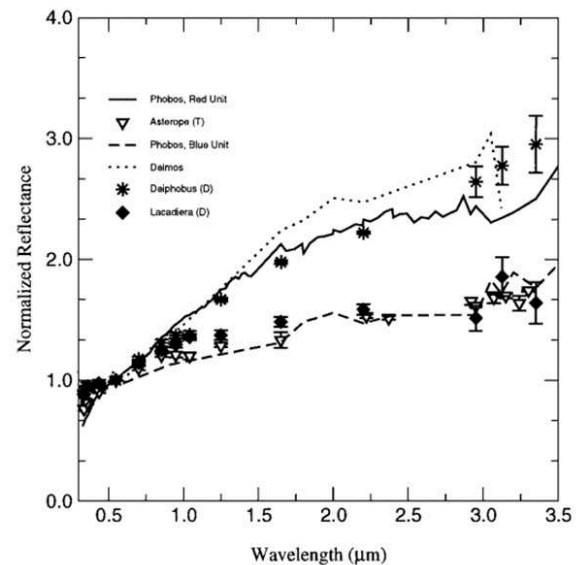


**Figure 4.5:** Comparison of the two spectral units of Phobos with the main belt asteroids 1867 Deiphobus and 336 Lacadera of type D and 233 Asterope of type T (Source: Rivkin et al. [2002])

From later ground based and spacecrafts measurements it was inferred that the surface of Phobos shows spectral heterogeneity, i.e. the surface of Phobos can be divided

into two fundamental spectral units. The Phobos bluer unit (PBU) (Fig. 4.5) which is associated with the Stickney crater corresponds roughly to the leading hemisphere (longitudes from  $0^\circ$  to  $180^\circ$ ) of Phobos with a typical visible-wavelength albedo of 6 - 7 %. The Phobos redder unit (PRU) (Fig. 4.5) corresponds mainly to the trailing hemisphere (longitudes from  $180^\circ$  to  $360^\circ$ ) and has also a low visible-wavelength albedo of 5 - 6 % (Murchie and Erard [1996]).

Later measurements show also that the spectra of Phobos can not be matched by C-type asteroids as it was suggested primarily. Both spectral units of Phobos are bracketed by D-type asteroids but the PBU provides also a good match with T-type asteroids (Rivkin *et al.* [2002]). The comparison with the main belt asteroids 1867 Deiphobus and 336 Lacadiera of type D and the 233 Asterope of type T with both spectral units can be seen in Figure 4.5. From this follows that Phobos originates from the outer part of the asteroid belt if it is a captured asteroid.

Asteroids are considered as parent bodies or the source of meteorites therefore meteorite analogues of asteroids can be used to identify some physical properties like grain size due to the availability of laboratory analysis of the according material. Comparison with meteorite analogues shows that the best match to the PBU seems to come from strongly heated carbonaceous chondrites. In Figure 4.6 the comparison of the PBU to a sample of a CM chondrite heated to 700 C is shown. But the good analogy can only be achieved for the PBU and is not true for the PRU (Rivkin *et al.* [2002]).

Carbonaceous meteorites can be classified into two main groups. Firstly the low grade chondrites, characterized by significant water content and low Fe and secondly the most dry high grade chondrites. The low grade chondrites consist of CI and CM chondrites having a visible wavelength albedo ranging from 3 - 5 % (Britt and Consolmagno [2000]). The high grade chondrites can additionally be distinguished by their Fe-content. CO, CV having low Fe-content and CR carbonaceous chondrites are Fe-rich (Britt *et al.* [2002]). High grade chondrites having a visible wavelength albedo of 8 - 20 % (Britt and Consolmagno [2000]). Usually CI chondrites have 10 - 20 % water and CM chondrites 5 - 10 % water and this results in 3  $\mu\text{m}$  band depths upward 50 % (Rivkin *et al.* [2002]). But in the spectra of Phobos only weak or no absorption due to  $\text{H}_2\text{O}$  at 3  $\mu\text{m}$  can be found. In addition only weak mafic mineral absorption was found which indicates low Fe-content (Table 4.4). The according bulk and grain density of the above carbonaceous chondrites are shown in Table 4.3.

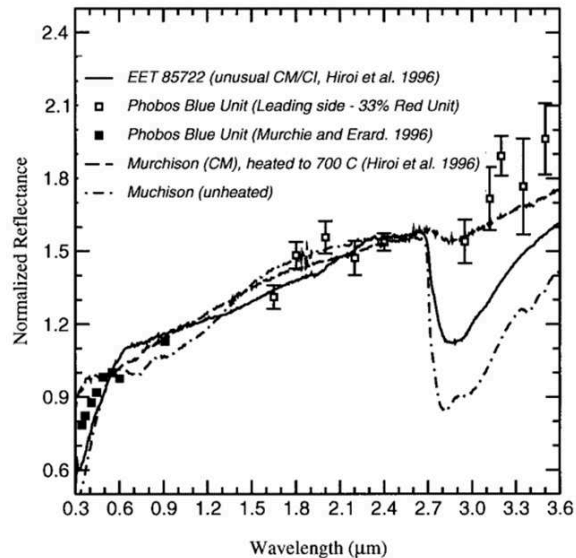


**Figure 4.6:** Comparison of the bluer unit of Phobos to thermally metamorphosed CM meteorites (Source: Rivkin *et al.* [2002])

There is only one meteorite as an analogue for D- and P-class asteroid, the Tagish Lake carbonaceous chondrite. As mentioned above the spectra of the PBU and PRU are bracket by D-class asteroids and the Tagish Lake carbonaceous chondrite representing these outer belt asteroids. Its bulk density is low compared to its grain density (Table 4.3) which suggests a porosity of 40 % (*Hildebrand et al.* [2006]).

Meteorite analogue	Bulk density [g/cm <sup>3</sup> ]	Grain density [g/cm <sup>3</sup> ]	Porosity [%]
CI (Ivuna group)	2.12	2.27	11
CM (Mighei group)	2.21	2.71	12
CO (Ornans group)	3.11	3.69	16
CR (Renazzo group)	3.15	3.11	6
CV (Vigarano group)	3.10	3.51	11
Tagish Lake	1.64 ± 0.02	2.72 <sup>+0.19</sup> <sub>-0.16</sub>	-

**Table 4.3:** Bulk density, grain density and average porosity of meteorite analogues (*Britt et al.* [2002], *Hildebrand et al.* [2006]). No value for the average porosity of the Tagish Lake meteorite is available.

Although no meteorite analogue can be found for Phobos which entirely fits the spectra of Phobos, due to the absence of the H<sub>2</sub>O absorption band at 3 μm and the weak mafic mineral absorption band Phobos seems to be a high grade CO or CV chondrite in sense of its meteorite analogues. But the visible wavelength albedo of Phobos and low grade chondrites are in agreement whereas the high grade chondrites having a significant higher albedo. Hence low grade chondrites seems to be better suited as a meteorite analogue of Phobos than high grade chondrites because changing the albedo is more difficult than surface dehydration by space weathering effects (*Moroz et al.* [2004]). In addition, the Tagish Lake carbonaceous chondrite can also be used as a meteorite analogue because it represents the outer belt D- and P-class asteroids. But its representation is limited by the fact that it is the only sample meteorite available so far for these asteroids.

Observation	Wavelength	Conclusions
M9 <sup>(1)</sup> VL2 <sup>(2)</sup>	0.255 - 345 μm 0.4 - 1.1 μm	• Spectra similar to C-type asteroids
Phobos 2 <sup>(3)</sup>	0.716 - 3.14 μm	• Spectral heterogeneity at km scale and a weak hydration signature
HST <sup>(4)</sup> <sup>(5)</sup>	0.21 - 0.80 μm	• Spectra similar to D-type asteroids
Phobos 2 <sup>(6)</sup>	0.33 - 3.16 μm	• Spectral heterogeneity with two fundamental units (the Phobos bluer unit (PBU) and the Phobos redder unit (PRU)) • Little or no absorption due to H <sub>2</sub> O at 3 μm and weak mafic mineral absorption at 1 μm • Surface material may be rich in mafic

continued on next page

Observation	Wavelength	Conclusions
		minerals and affected to different degrees by space weathering or surface could consist of a mixture of mafic-poor material (possibly resembling D-type asteroids) and mafic-rich material
IMP <sup>(7)</sup>	0.2 - 1.0 $\mu\text{m}$	<ul style="list-style-type: none"> <li>• Possible broad, shallow absorption-like 0.7 <math>\mu\text{m}</math> feature</li> <li>• Comparable red to D-type asteroids</li> <li>• Comparable to lowest albedo space-weathered mafic assemblages, such as some lunar mare soils</li> </ul>
IRTF <sup>(8)</sup>	1.65 - 3.5 $\mu\text{m}$	<ul style="list-style-type: none"> <li>• Two different spectral units</li> <li>• No evidence for hydration band at 3 <math>\mu\text{m}</math> within 5-8%</li> <li>• No evidence for 2 <math>\mu\text{m}</math> pyroxene within 4-5%</li> <li>• D-type asteroids span the range of spectra from the PBU to the PRU</li> <li>• T-type asteroids provide a good match for the PBU</li> <li>• Strongly heated carbonaceous chondrites provide the best match for the PBU</li> </ul>
Phobos 2 <sup>(9)</sup>	0.33 - 3.16 $\mu\text{m}$	<ul style="list-style-type: none"> <li>• Two bands in lower albedo areas at 1.04 <math>\mu\text{m}</math> and 1.9 <math>\mu\text{m}</math> detected</li> <li>• Both features could correspond to a mixture of olivine (1.04 <math>\mu\text{m}</math>) and low-calcium pyroxene (1.9 <math>\mu\text{m}</math>)</li> <li>• Possible shallow hydration band in small areas with a depth of about 10%</li> </ul>
CRISM <sup>(10)</sup> onboard MRO	0.362 - 3.92 $\mu\text{m}$	<ul style="list-style-type: none"> <li>• No evidence for 1 <math>\mu\text{m}</math> or 2 <math>\mu\text{m}</math> mafic mineral absorptions</li> <li>• No evidence for 3 <math>\mu\text{m}</math> absorption due to bound water due to organics</li> </ul>
OMEGA <sup>(11)</sup> onboard MEX	0.35 - 5.10 $\mu\text{m}$	<ul style="list-style-type: none"> <li>• No evidence for hydration band or of organic material</li> </ul>

**Table 4.4:** Summary of results from spectral measurements of Phobos. The according references are indicated by footnotes <sup>(1)</sup>Pollack et al. [1978], <sup>(2)</sup>Pang et al. [1978], <sup>(3)</sup>Bibring et al. [1989], <sup>(4)</sup>Zellner and Wells [1994], <sup>(5)</sup>Murchie and Zellner [1994], <sup>(6)</sup>Murchie and Erard [1996], <sup>(7)</sup>Murchie [1999], <sup>(8)</sup>Rivkin et al. [2002], <sup>(9)</sup>Gendrin et al. [2005], <sup>(10)</sup>Murchie et al. [2008] and <sup>(11)</sup>Gondet et al. [2008])

### 4.3.5 Origin

The origin of both Martian moons presents an inconsistency which is not solved so far. Explanations for the origin of Phobos seems to be connected with the origin of Deimos. Therefore, the origin of both moons are discussed here. There exist two main theories, one that argues for accretion in orbit and the other that the Martian moons were formed in the outer part of the asteroid belt and captured later by Mars. Both main theories are explained in the following.

#### 4.3.5.1 Capturing

- Separately capturing: Based on the spectral similarities of Phobos (see section 4.3.4) it was suggested that Phobos could be formed in the outer part of the asteroid belt and then captured by the gravitational attraction of Mars. But this suggestion raises some problems. Assuming Phobos is a captured asteroid the hyperbolic orbit of an asteroid must be transformed into a bound planetocentric orbit. This process must compensate the energy dissipation necessary for this orbit change somehow. But the energy dissipation can not be raised only by tidal friction.

One explanation accounting for the necessary energy dissipation could be aerodynamic drag. The drag usually take place in a nebula surrounding Mars shortly after its formation. But the capturing process at many planetary radii requires a fairly substantial nebula and in this nebula the rapid evolution would cause the captured body to fall quickly to the surface of Mars (*Burns* [1992]). At large distances the orbit would not evolve rapidly but it is unlikely that the body to be captured can be decelerated enough to go into a bound orbit around Mars.

Another energy dissipation mechanism could be the collision between the asteroid to be captured and another small body already orbiting Mars in between its Hill sphere or from the collision of two unbound small bodies leaving one with significant energy loss to be captured (*Peale* [2007], *Jewitt and Haghighipour* [2007]).

But captured bodies usually have non-circular orbits not aligning with the orbital plane of the central body, i.e. having significant eccentricity and inclination as it is the case like for the irregular satellites of Saturn (*Gladman et al.* [2001]), but the orbit of Phobos and Deimos are nearly circular and close to the equatorial plane of Mars.

In addition, *Szeto* [1983] raised problems besides the unexplained energy dissipation needed in the capturing processes. Collision probabilities between Phobos and Deimos based on orbital evolution models show that Phobos and Deimos would most probably have collided at some stage of their evolution if they are captured asteroids.

- Capturing of a large body: Another suggestion is that Phobos and Deimos could also be formed from one single large body which is also captured. Capturing of a large body is dynamically easier due to the larger tidal friction which is able to

account for parts of the energy dissipation needed to change from hyperbolic orbit to circular orbit (*Burns [1992], Singer [2007]*). But if Phobos and Deimos originate from the same parent body both should have the same spectral properties but Deimos is spectral homogeneously in contrast to the heterogeneously spectra of Phobos (see section 4.3.4).

The capturing theory raises problems which are not solved so far despite which capturing scenario is selected. Therefore it seems unlikely but not impossible that Phobos is a captured asteroid.

#### 4.3.5.2 Accretion in orbit

- Originating in the vicinity of Mars: Another possible explanation for the origin of Phobos and Deimos is that they are build from a debris disk remaining from the formation process of Mars. This forming process is the usual one observed for the regular satellites of the giant planets (*Peale [2007]*) and the process responsible for the agglomeration of the Martian moons might be similar to it, although in the first one gas-dominated accretion was more probable. Phobos and Deimos satisfy the orbital criteria for regular satellites by their nearly coplanar, circular orbit (see section 4.3.3). But Phobos and Deimos should also be composed of similar material like Mars if they were final remnants of the nebula from which Mars itself grew. But this is not the case which can be seen by comparing the spectra of Phobos with locations on Mars (*Bibring et al. [1989]*). Mars has also a significant higher mean bulk density of  $3.9335 \pm 0.0004 \text{ g/cm}^3$  (*Kieffer et al. [1992]*) than Phobos and Deimos.

A possibility to solve this inconsistency can be that a body formed in the debris disk remaining from the formation process of Mars could be collided with a planetesimal formed in the asteroid belt region and a new debris disk was formed from the shattering of this bodies. But in order to build a debris disk the remaining pieces of the collision should be very small and of large number (*Peale [2007]*).

- Debris disc remaining from a collision: Alternatively, Phobos and Deimos could be formed from a debris disk remaining from the collision of a larger body with a diameter of about 1800 km with Mars itself (*Craddock [1994]*). The impact of this large body could account for the relative high rotation rate of Mars which is difficult to explain without an impact. A possible impact location could be the 7700 km Borealis basin but the are existing other impact basin on Mars from which enough debris could have been placed into the orbit around Mars. If the impacting body would consist of carbonaceous chondrite some of the orbiting material could also be of this type (*Craddock [1994], Peale [2007]*).

Both theories seems to be possible, but the spectral difference between Mars and its both moons can not be explained entirely with both theories.

---

## Results

---

### 5.1 Phobos

Mars Express (MEX) has performed two close flybys at the Mars moon Phobos in March 2006 and July 2008. In the following the flyby parameter of each flyby and the resulting mass estimate is shown. Based on the mass estimate the origin of Phobos is discussed.

#### 5.1.1 Results from close flybys

MEX is in a nearly polar orbit about Mars and Phobos in a nearly equatorial orbit (see section 4.3.3). The configuration for a close flyby is that MEX is approaching Phobos from the North pole direction, entering the equator of Mars where the closest distance between MEX and Phobos is achieved and leaving Phobos in the direction toward the South pole (figure 5.1).

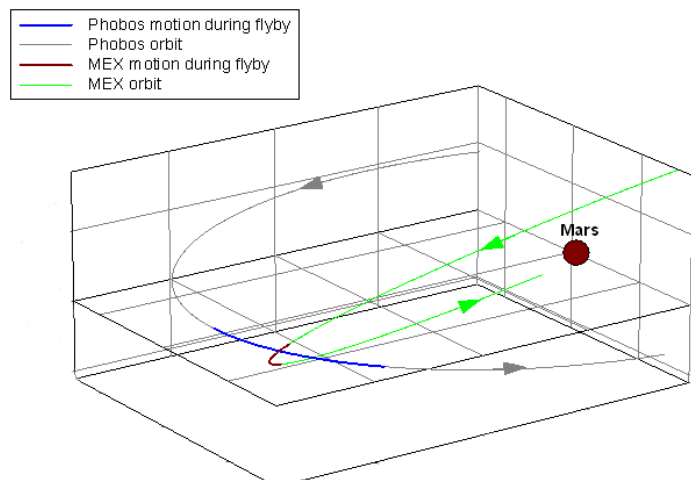


**Figure 5.1:** Usual geometry for flybys of MEX at Phobos.

### 5.1.1.1 The flyby on 23 March 2006

MEX performed one close flyby at Phobos at a distance of 459 km on 23 March 2006. The data were recorded at the 70 m ground station of the Deep Space Network (DSN) near Madrid (DSS-63). The relative flyby velocity between MEX and Phobos was 2.8 km/s and the angle between the Line of Sight (LOS) and the velocity component of MEX relative to Phobos increased from  $96^\circ$  (1 h before Closest Approach) to  $105^\circ$  at CA and decreased again after CA.

In figure 5.4 the frequency residuals  $f_{res}$  according to equation (3.1) indicated by the gray line, i.e. the frequency recorded at ground station after subtracting the predicted frequency  $f_{pre}$  and the contribution of the Earth's atmosphere  $f_{atm}$  is shown. The residuals are referred to an uplink frequency of 7.167317664 GHz.

The noise of the frequency residuals is reduced by applying consecutively a kaiser window filter and a moving average filter (see section 2.9). The appropriate parameter of both filters, the cut-off frequency  $f_c$  of 57 mHz and the sample time  $\Delta t$  of 40 seconds, are estimated using a lower and upper limit of the  $GM$  of Phobos. As it can be seen from Table 4.2 in section 4.3.2 the  $GM$  of Phobos from the past measurements lies well within  $0.70$  and  $0.73 \times 10^{-3} \text{ km}^3/\text{s}^2$  which is used for estimating the above mentioned filter parameter in figure 5.2 and 5.3. The resulting filtered data are indicated in figure 5.4 with the red line.

If the amplitude of the frequency residuals changes for this flyby by 0.1 mHz, the  $GM$  would change by  $0.01 \cdot 10^{-3} \text{ km}^3/\text{s}^2$ . However, the selected upper limit of 0.1 mHz for the change of the frequency residuals by the applied filter can not be achieved due to the selected cut-off frequency and time interval. Therefore, the effect of the applied

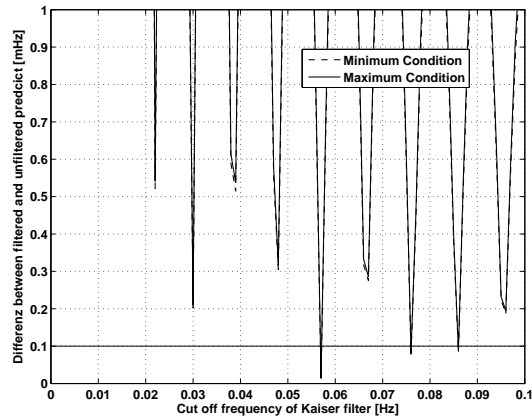


**Figure 5.2:** Difference between the frequency change of the filtered and unfiltered measurement data for the minimum ( $0.70 \times 10^{-3} \text{ km}^3/\text{s}^2$ ) and maximum condition ( $0.73 \times 10^{-3} \text{ km}^3/\text{s}^2$ ) for different cut of frequencies  $f_c$  of the Kaiser filter for the Phobos flyby in 2006.

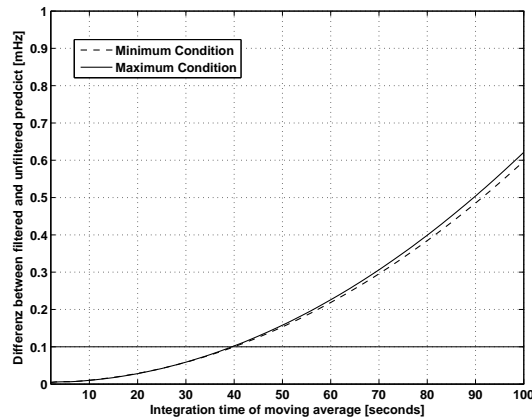


**Figure 5.3:** Difference between the frequency change of the filtered and unfiltered model data for the minimum ( $0.70 \times 10^{-3} \text{ km}^3/\text{s}^2$ ) and maximum condition ( $0.73 \times 10^{-3} \text{ km}^3/\text{s}^2$ ) or different sample times  $\Delta t_{mov}$  of the moving average filter for the Phobos flyby in 2006.

filter on the  $GM$  estimate of Phobos is lower than  $0.01 \cdot 10^{-3} \text{ km}^3/\text{s}^2$ . This value is based on the sensitivity of  $1.02 \cdot 10^{-4} \text{ km}^3/\text{s}^2 \text{ mHz}$ . It is deduced from two frequency shift estimates with different  $GM$  values and the resulting maximum in amplitude difference. In conclusion, the applied filters reduce the standard deviation of the frequency residuals by more than a factor of three from 6.56 mHz to 1.71 mHz.

A problem in fitting the model data indicated in figure 5.4 by the blue line to the filtered measurement bears the late start of the recording which started approximately 15 minutes before CA. It seems that the contribution from the gravitational attraction of Phobos was large enough for being visible in the recorded data. No more data before CA are available which can be used for estimating initial parameter like the state vector independently from the  $GM$  estimate.

In the fitting process the initial velocity  $\mathbf{v}_{ini}$  of the spacecraft, the scale factor  $k$  for the solar radiation pressure and the  $GM$  of Phobos are simultaneously estimated from the filtered frequency residuals. A constant offset  $f_o$  aligning the model data with the frequency shift is estimated separately. The difference between the model data and the frequency residuals is minimal after a few iterations. The parameters are estimated to

$$\begin{aligned} v_{x\ ini} &= -8269538.012 \pm 0.049 \text{ mm/s} \\ v_{y\ ini} &= 2525415.091 \pm 0.008 \text{ mm/s} \\ v_{z\ ini} &= -2546616.020 \pm 0.005 \text{ mm/s} \\ GM &= 0.7120 \pm 0.011 \cdot 10^{-3} \text{ km}^3/\text{s}^2 \\ k &= 1.300 \pm 0.137 \\ f_o &= -12.01 \pm 0.04 \text{ mHz} \end{aligned}$$

The initial velocity differs in the  $x$ ,  $y$ , and  $z$  direction from the orbit provided by ESOC by -0.032 mm/s, 0.025 mm/s and -0.025 mm/s, respectively. These differences are in the range of the orbit error from ESOC (*del Rio* [2006]).

Taking into account the uncertainty of the  $GM$  estimate due to the uncertainty of the constant offset  $f_o$  of 0.04 mHz  $\equiv 0.45 \cdot 10^{-5} \text{ km}^3/\text{s}^2$  the final result from the flyby in 2006 of the  $GM$  estimate reads

$$GM = 0.7120 \pm 0.012 \times 10^{-3} \text{ km}^3/\text{s}^2.$$

Obviously the error of the estimate is driven by the short recording phase before CA at Phobos and the large flyby distance.

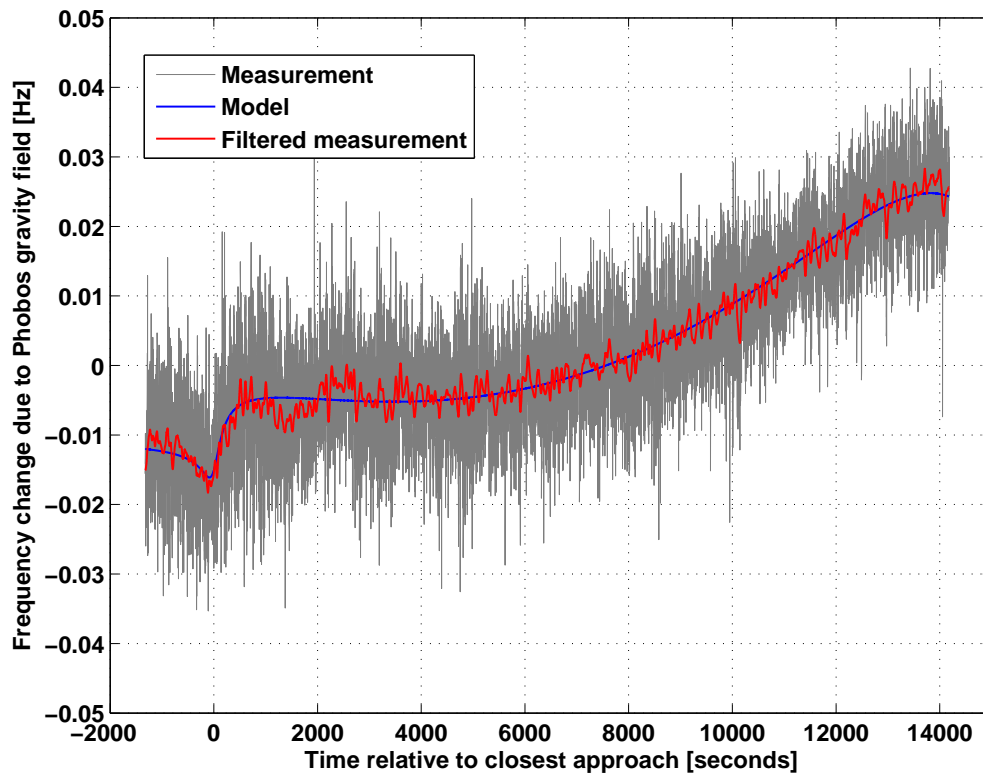


*Figure 5.4:* Measured, filtered and modeled frequency residuals caused by the gravitational attraction of Phobos from the Phobos flyby in 2006.

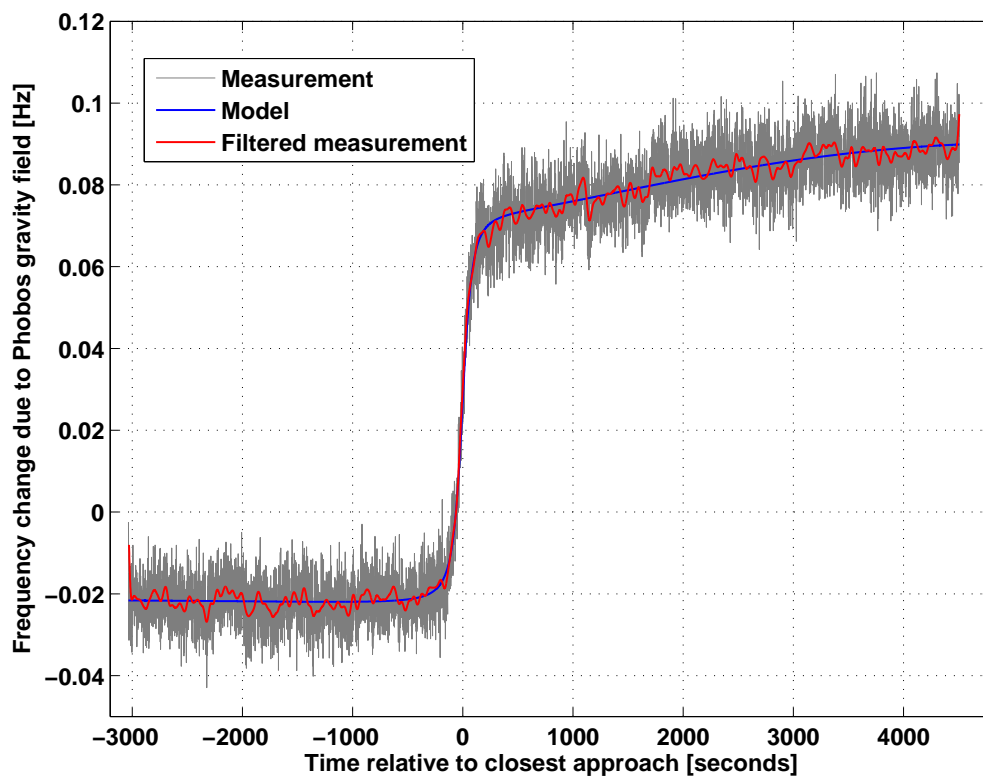


*Figure 5.5:* Measured, filtered and modeled frequency residuals caused by the gravitational attraction of Phobos from the Phobos flyby in 2008.

### 5.1.1.2 The flyby on 17 July 2008

In July 2008 MEX performed three consecutive flybys at Phobos. The flyby at a distance of about 275 km on 17 July 2008 was used by MaRS for a precise mass estimate. The data were recorded at the NASA 34 m tracking station near Madrid (DSS-65). The relative flyby velocity between MEX and Phobos was 3.0 km/s and the angle between the Line of Sight (LOS) and the velocity component of MEX seen from Phobos increased from  $38^\circ$  (1 h before Closest Approach) to  $88^\circ$  at CA and decreased after CA.

The parameters for this flyby are optimal compared to the flyby in 2006 (Figure 5.5). The maximum frequency shift caused by the gravitational attraction of Phobos is 110 mHz, the recorded frequency referring to an uplink frequency of 7.167131904 GHz.

The same procedure for estimating the appropriate filter settings is applied as described above for the flyby in 2006 with the same lower and upper limit for the  $GM$  of Phobos. The resulting filter parameter  $f_c$  and  $\Delta t_{mov}$  are 30 mHz and 15 seconds, respectively (see figure 5.6 and 5.7). The applied filter reduce the standard deviation of the measurement from 7.32 mHz to 1.97 mHz by a factor of about four. A sensitivity value of  $6.55 \cdot 10^{-6} \text{ km}^3/\text{s}^2 \text{ mHz}^2$  is also obtained for this flyby as described above. With this, the effect of the applied filter on the  $GM$  estimate is lower than  $6.55 \cdot 10^{-7} \text{ km}^3/\text{s}^2$ , i.e. if the filter reduces the amplitude of the frequency change, the resulting  $GM$  estimate would not differ more than  $6.55 \cdot 10^{-7} \text{ km}^3/\text{s}^2$  from the value without filtering, but the noise is perceptible reduced.

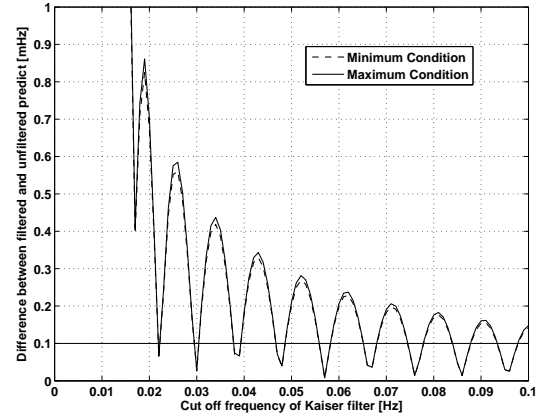


**Figure 5.6:** Difference between the frequency change of the filtered and unfiltered measurement data for the minimum ( $0.70 \times 10^{-3} \text{ km}^3/\text{s}^2$ ) and maximum condition ( $0.73 \times 10^{-3} \text{ km}^3/\text{s}^2$ ) for different cut-off frequencies  $f_c$  of the Kaiser filter for the Phobos flyby in 2008.

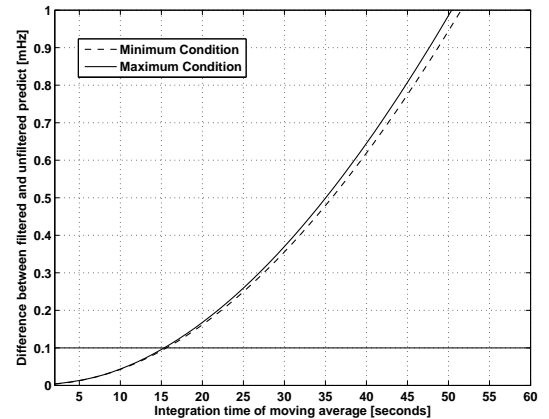


**Figure 5.7:** Difference between the frequency change of the filtered and unfiltered model data for the minimum ( $0.70 \times 10^{-3} \text{ km}^3/\text{s}^2$ ) and maximum condition ( $0.73 \times 10^{-3} \text{ km}^3/\text{s}^2$ ) or different sample times  $\Delta t_{mov}$  of the moving average filter for the Phobos flyby in 2008.

The recording started for this flyby early enough for obtaining data well before CA, where the gravitational attraction of Phobos is irrelevant. The initial velocity  $\mathbf{v}_{ini}$ , the scale factor  $k$  and the  $GM$  of Phobos are simultaneously and the constant offset  $f_o$  is separately estimated. The parameters and the according errors read

$$\begin{aligned}
 v_{x\ ini} &= 2718592.010 \pm 0.028 \text{ mm/s} \\
 v_{y\ ini} &= -0989394.654 \pm 0.070 \text{ mm/s} \\
 v_{z\ ini} &= -2268721.321 \pm 0.041 \text{ mm/s} \\
 GM &= 0.7127 \pm 0.0020 \cdot 10^{-3} \text{ km}^3/\text{s}^2 \\
 k &= 1.443 \pm 0.142 \\
 f_o &= -21.62 \pm 0.07 \text{ mHz}
 \end{aligned}$$

The initial velocity differs in the  $x$ ,  $y$ , and  $z$  direction from the ESOC orbit by -0.2590 mm/s, -0.641 mm/s and 0.016 mm/s, respectively. Taking into account the error due to  $f_o$  then the resulting estimate is

$$GM = 0.7127 \pm 0.0021 \times 10^{-3} \text{ km}^3/\text{s}^2.$$

This measurement provides a mass estimate with a very small error of 0.3 % (one standard deviation), compared to previous mass estimates based on close flybys and/or distant encounters (Figure 5.8). The error of the estimate is mainly driven by the noise of the recorded data.

The mass estimates from *Yuan et al.* [2001], *Konopliv et al.* [2006] and *Rosenblatt et al.* [2008] are based on several years of tracking data (Fig. 5.8). The large number of tracking data reduces the statistical error of the estimate from long term observations, i.e. the error caused by the noise of the data is compensated by the large number of data. However, not all tracking data used have to be relevant for changes in the frequency induced by the gravitational attraction of Phobos on the spacecraft. The difference between the results from the long term observations from *Yuan et al.* [2001], *Konopliv et al.* [2006] and *Rosenblatt et al.* [2008] can be caused by systematic error. They have a strong impact on the resulting mass estimate because of the small changes of the frequency observed at long term observations and the small statistical error caused by the large number of data sets.

Figure 5.8 shows a comparison of results for the mass of Phobos derived from this thesis and from previous works. The blue line indicates the result from the flyby in 2008. It is obviously that the results from the close flybys in 2006 and 2008 are enclosed by the estimates from the long term observations from *Yuan et al.* [2001], *Konopliv et al.* [2006] and *Rosenblatt et al.* [2008], i.e. the results of this thesis seems to be mean values with reasonable error bars of that estimates with the long term solutions spread around the close flyby solutions from this thesis. This endorses the reliability of the results from the MEX close flybys at Phobos.

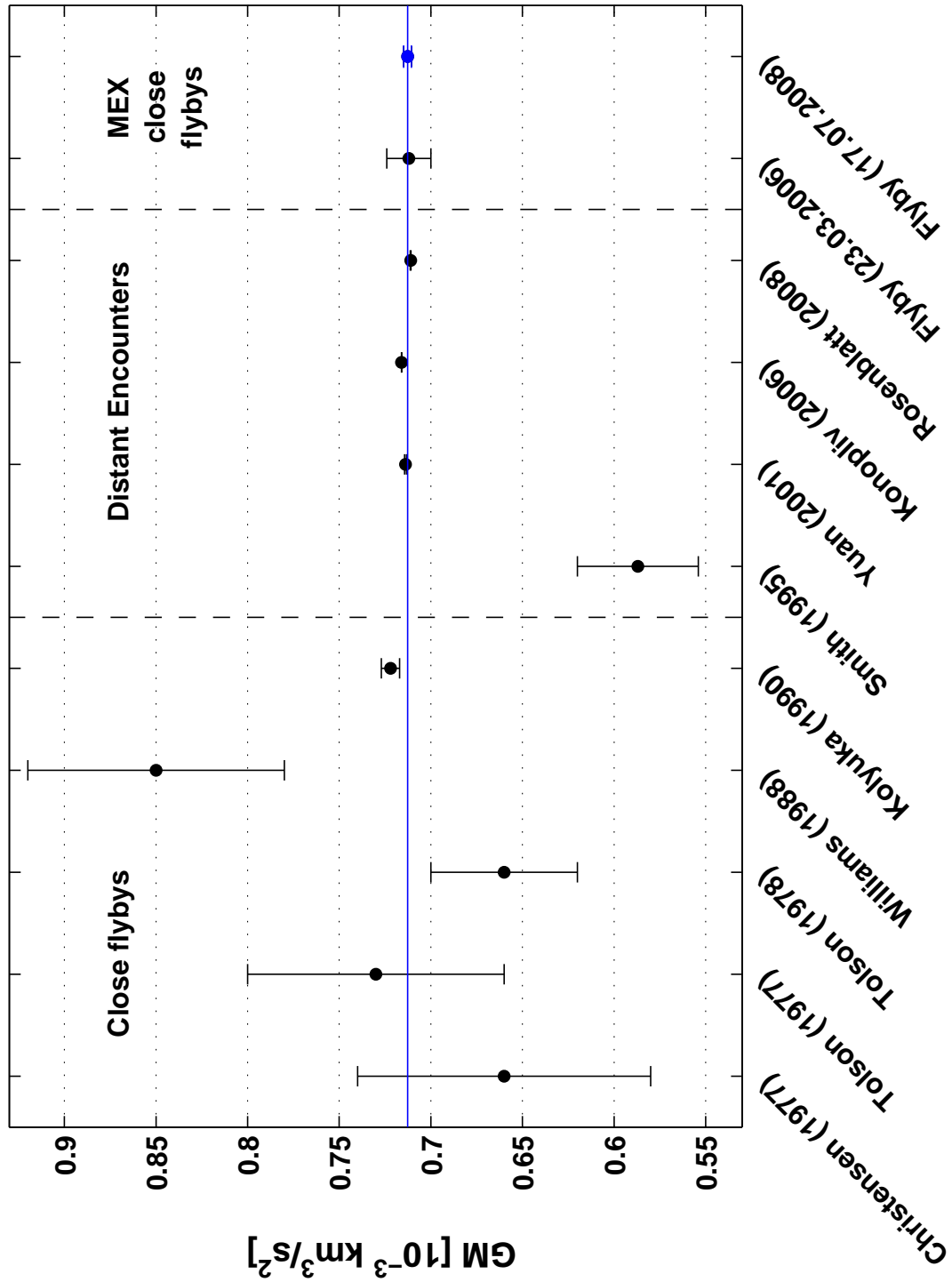


**Figure 5.8:** Comparison of past mass estimates of Phobos with the results from the flyby in 2006 and in 2008. The blue line indicates the result from the flyby in 2008 with  $GM = 0.7127 \pm 0.0021 \times 10^{-3} \text{ km}^3/\text{s}^2$ .

## 5.1.2 Interpretation of the results

### • Density

From the above derived precise mass estimate and using the volume estimate from *Willner et al.* [2009] (see section 4.3) the density of Phobos is computed to

$$\rho = 1.88 \pm 0.02 \text{ g/cm}^3.$$

It is obvious, that the error of the density is driven by the error of the volume estimate.

It was suggested from the first spectral measurements that Phobos is a captured carbonaceous chondrite asteroid. The bulk density of Phobos is higher than that of most carbonaceous chondrite, C-type, asteroids, e.g., 253 Mathilde, with a density of  $1.34 \pm 0.20 \text{ g/m}^3$ . The bulk densities of silicate-rich, S-type, asteroids such as 433 Eros with  $2.67 \pm 0.03 \text{ g/m}^3$ , are much larger (Fig. 5.9). Bulk densities of other asteroidal types vary over wide ranges. For these reasons it is difficult to conclude on possible connections between the origin of Phobos and asteroidal types on the basis of the bulk density only.

Comparing the bulk density with different meteorites analogues (Fig. 5.9) which are suggested to be appropriate candidates for Phobos based on spectral measurements shows that Phobos density is lower than that of low grade carbonaceous chondrites (CI and CM chondrites) and much lower than that of high grade carbonaceous chondrites (CO and CV chondrites). But it is higher than the bulk density of the Tagish Lake meteorite. The densities of the meteorite analogues and the Tagish Lake meteorite are shown in Table 4.3.

Phobos bulk density is significant lower than the bulk density of the Martian crust ( $\rho_{crust} = 2.9 \pm 0.2 \text{ g/cm}^3$ , *Wieczorek and Zuber* [2004]), (Fig. 5.9).

### • Internal structure

The porosity  $\eta_p$  of an object is defined as the ratio of its bulk density  $\rho_b$  (the mass of an object divided by its volume) to its grain density  $\rho_g$  (the mass of an object divided by the volume filled only by mineral grains), i.e.

$$\eta_p = \left(1 - \frac{\rho_b}{\rho_g}\right) 100. \quad (5.1)$$

It is the percentage of the object which is occupied by empty space. Figure 5.10 shows the porosity of Phobos for different possible material analogues. It was concluded from the spectral properties of Phobos that it can be composed of material analog to a dehydrated CM chondrite or to the Tagish Lake meteorite. The grain density is always equal or larger than the bulk density of the body. With this a lower limit of the grain density of the Martian crust is given by its bulk density which is used for the porosity value of Phobos. It is obvious that Phobos has a large porosity ranging from 32 % - 36 % regardless which analog material is used (Fig. 5.10).

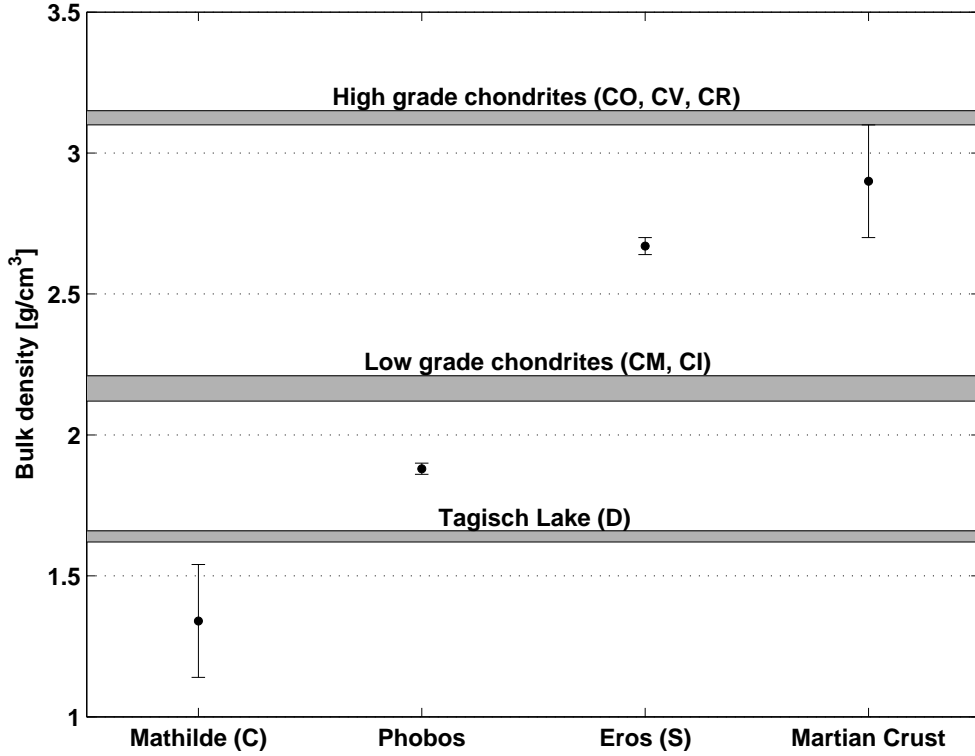


**Figure 5.9:** Comparison of Phobos bulk density (blue line, the gray dashed lines indicating the uncertainty) with the bulk density of meteorite analogues, selected asteroids and the Martian crust.

The macroporosity  $\eta_m$  of an asteroid is defined as the difference between the bulk porosity and the mean meteorite analog porosity (*Britt et al.* [2002]), i.e.

$$\eta_m = \left(1 - \frac{\rho_b}{\rho_g}\right) 100 - \bar{\eta}_p = \eta_p - \bar{\eta}_p. \quad (5.2)$$

Asteroids can be divided according to *Britt et al.* [2002] by their macroporosities into three main groups (Fig. 5.11): asteroids which are mainly solid objects, asteroids with macroporosities of about 20 % which are probably heavily fractured and asteroids with macroporosities  $> 30$  %, so called rubble piles. Figure 5.11 shows the macroporosity of  $18.6 \pm 0.7$  % Phobos using CM chondrite (Table 4.3) as a possible meteorite analogue compared with the macroporosity of other asteroids. If Phobos is a captured asteroid its macroporosity value suggests that it is a heavily fractured asteroid close to the transition zone to loosely consolidated asteroids.

The surface of Phobos is heavily cratered, with Stickney as the largest example. The approximately 10 km diameter of Stickney is in the order of Phobos' radius. Craters of large relative sizes can only form in bodies which are able to absorb the collision energy near the impact site. A solid body would be destroyed by correspondingly high collision energies (*Richardson et al.* [2002]). The existence of the Stickney crater, therefore, also supports the conclusion that Phobos contains large voids throughout its interior.

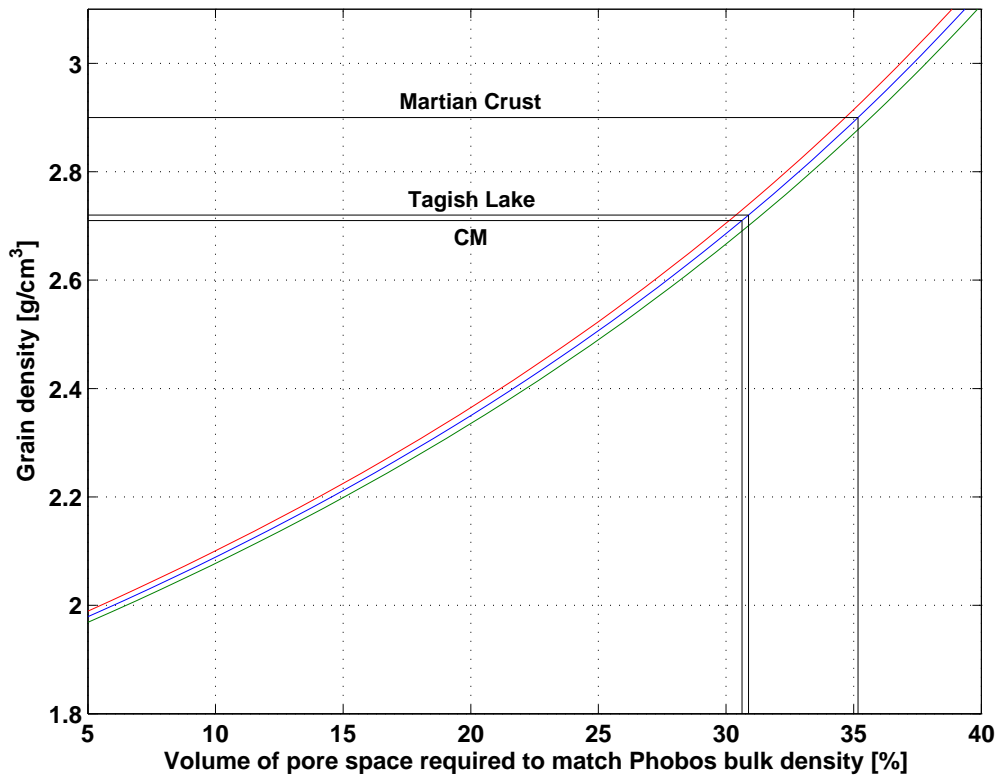


**Figure 5.10:** Porosity of Phobos (blue line, the gray dashed lines indicating the uncertainty) versus grain density with the grain density of possible material analogues.

- **The origin of Phobos**

The fact that Phobos contains large voids inside leads to the conclusion that re-accretion is the preferable formation mechanism of Phobos. Besides the problem of energy loss required in the capturing process (see section 4.3.5) a highly porous body is expected to be much less resistant to large external gravitational gradients than a solid body (*Richardson et al.* [2002]). It follows that an object with the porosity of Phobos would have been destroyed by the gravitational forces required for orbit capture. It seems to be unlikely from Phobos high porosity that it is a asteroid captured as whole.

Another hypothesis is that Phobos and Deimos are remnants of an early, larger body that has been destroyed into two or more pieces by gravitational gradient forces exerted by Mars during capture (*Singer* [2007]). Self gravity forces acting before break up would eliminate the voids a priori. This scenario can be true if the large body would have been destroyed and the small peaces would build an debris disc from which Phobos could be build by re-accretion.

Phobos also could have formed by re-accretion of impact debris lifted into Mars' orbit (*Craddock* [1994]). Large blocks may have been re-accreted first due to their larger gravitational attraction, thus forming a core of boulders with voids in between. Smaller debris re-accreted later, but owing to low self-gravity forces did not fill the voids left by the large pieces (*Richardson et al.* [2002]). The debris disc should be composed of crust material and also of material of the impactor with crust material being the majority as it is for the Earth moon. But the spectra

of the Martian crust and of Phobos does not match very well. This inconsistency could be solved by the collision of a body formed from the debris disc remaining from the formation process of Mars and a body formed in the asteroid belt region. This scenario is consistent with a high porosity of Phobos from re-accretion and also the spectral properties of Phobos could be explained.

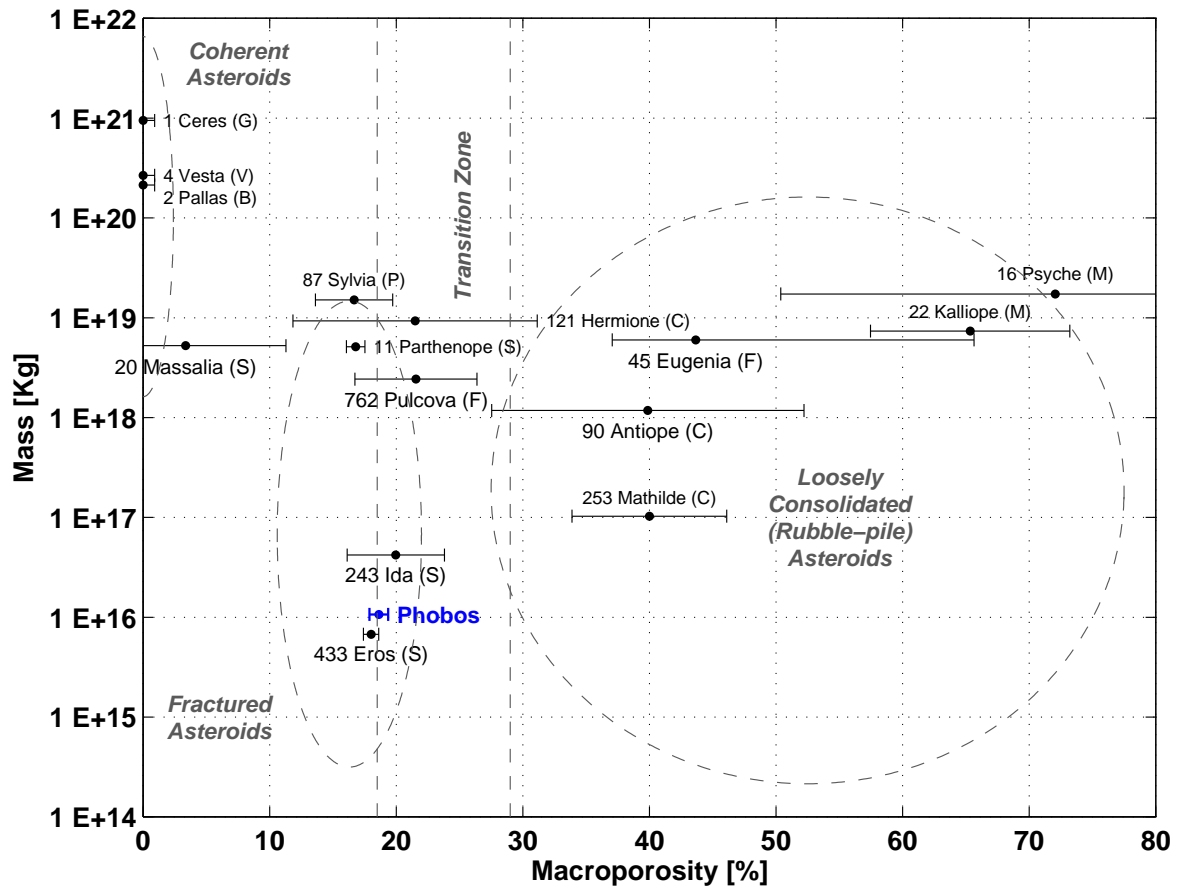


**Figure 5.11:** Comparison of the macroporosity of asteroids (values taken from Britt et al. [2002] or from JPL [2009])



### 5.1.3 Future flybys in 2010

The Mars Express spacecraft will perform an orbit change in February 2010 into an interim orbit which will allow three consecutive flybys at Phobos in March 2010. Closest flyby distances will be 62 km on 3 March, 2010, 120 km on 07 March, 2010 and 488 km on 13 March, 2010. All flybys were analyzed by their feasibility for Radio Science measurements with the method developed in this thesis. Based on this analysis the first flyby at a distance of 62 km was assigned to the Radio Science experiment. In the following this unique scientific opportunity is described in detail.

Figure 5.12 shows the visibility of the four main ground station complexes for the flyby at 62 km. The ground station in Madrid (DSS-63) will be fully visible during the entire flyby. The contribution on the radio signal by the Earth atmosphere will be small due to the large elevation angle. MEX will disappear 1 hour and 20 minutes before closest approach behind Mars for 36 minutes seen from the ground station.

This flyby will be due to the small distance of 62 km an unique opportunity for measuring the low order coefficient  $C_{2,0}$  of Phobos. Assuming a constant density distribution and an ellipsoid shape ( $a = 13.4$  km,  $b = 11.2$  km,  $c = 9.2$  km) the gravity coefficients of Phobos read

$$C_{2,0} = -0.0756$$

$$C_{2,2} = -0.0151$$

with a reference radius  $\bar{R} = 13.4$  km.

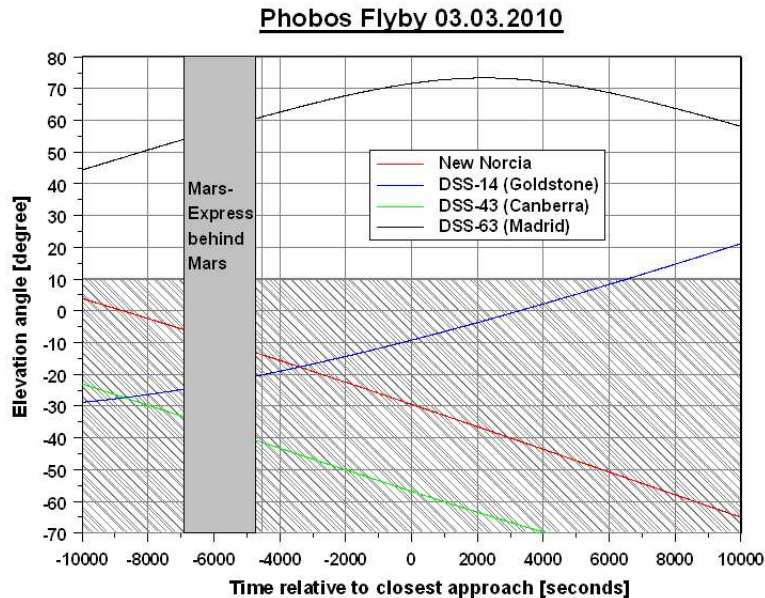


**Figure 5.12:** Ground station visibility during the Phobos flyby in March 2010 for the four main ground station complexes. An elevation angle of more than  $10^\circ$  indicates full visibility of the spacecraft from the ground station. Zero time corresponds to 21:02:00 (UTC, SC).

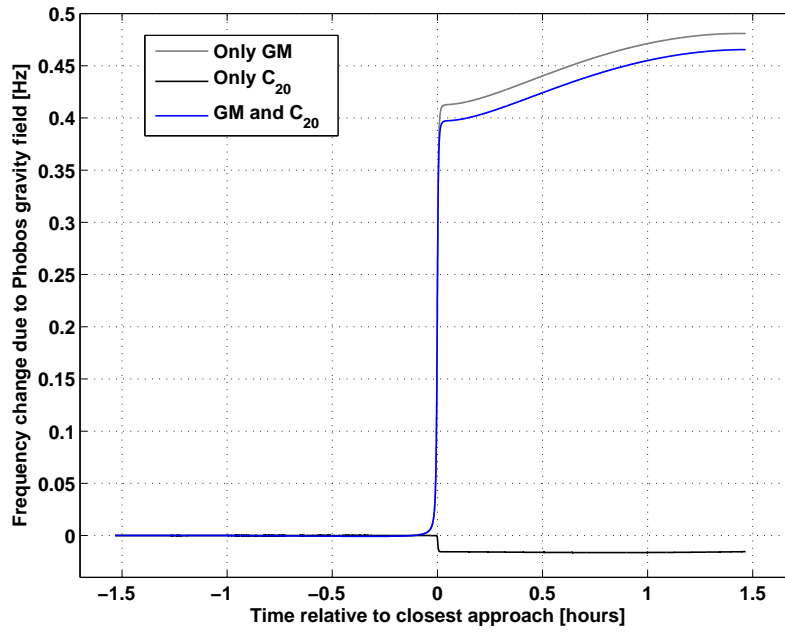


**Figure 5.13:** Estimated frequency change at the close flyby at Phobos in March 2010 ( $GM = 0.7127 \times 10^{-3} \text{ km}^3/\text{s}^2$  and  $C_{2,0} = -0.0756$ ). Frequency change corresponds to the uplink frequency of 7167317664 Hz.

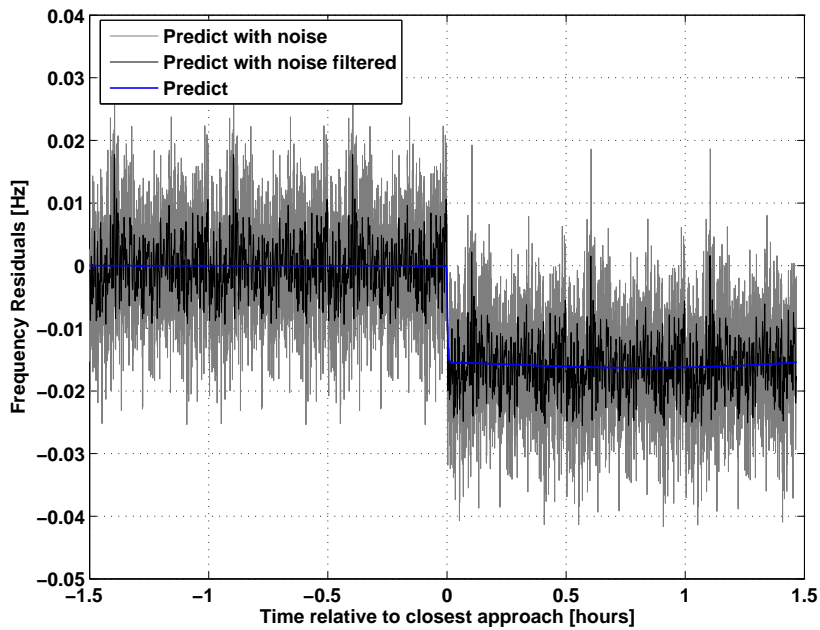


**Figure 5.14:** The estimated predict for the frequency change due to  $C_{2,0} = -0.0756$  with and without noise from a Radio Science measurement on July, 18 in 2006 and the filtered noisy frequency change.

Figure 5.13 shows the estimated frequency change  $\pm 1.5$  h around the closest approach for the flyby at a distance of 62 km. The entire frequency change is 0.46 Hz including the frequency change due to  $GM$  of 0.48 Hz and due to  $C_{2,0}$  of -0.018 Hz.  $C_{2,2}$  causes a frequency change which is smaller than 1 mHz and will not be detectable.

Noise from a Radio Science measurement on July, 18 in 2006 with standard deviation  $\sigma = 7.7$  mHz was added to the predicted frequency change in order to perform a feasibility study for estimating  $C_{2,0}$ . A least square fit was performed assuming  $C_{2,0}$  as the only fitting parameter. The resulting  $C_{2,0}$  is

$$C_{2,0} = -0.0801 \pm 0.0033.$$

The resulting  $C_{2,0}$  estimate has an error of 4.1 % corresponding to one standard deviation.

Applying consecutively a kaiser window filter and a moving average filter with a cut-off frequency  $f_c$  of 77 mHz and the sample time  $\Delta t$  of 2 seconds reduces the standard deviation  $\sigma = 4.1$  mHz of the noise by a factor of two. The cut-off frequency and the sample time are computed with the lower and upper limit with the same method as described in the last section. The lower and upper limit are defined to be  $\pm 50$  % of the nominal value ( $C_{2,0} = -0.0756$ ). Filter leads to a new value

$$C_{2,0} = -0.0758 \pm 0.0005$$

with a reduced error of 0.7 % which corresponds to one standard deviation. It will be possible to measure the  $C_{2,0}$  coefficient with an accuracy which was never obtained from a close flyby assuming that  $C_{2,0}$  is the only fitting parameter.

If Phobos has a non-uniform density distribution the value of  $C_{2,0}$  differs from the above value. Assuming a two layer model with a core density  $\rho_c = 2.30$  g/cm<sup>3</sup> occupying half of the ellipsoid ( $a = 6.7$  km,  $b = 5.6$  km,  $c = 4.6$  km) and a surface density  $\rho_s = 1.77$  g/cm<sup>3</sup>  $C_{2,0} = -0.0736$ . The difference of 2.6 % between this two values, i.e. between a two layer model and a model with uniform density distribution, can be detected with the flyby in March 2010.

The value of  $C_{2,0}$  depends on the shape model. *Andert* [2004] used different shape models for Phobos and computed the gravitational coefficients from it. The values of  $C_{2,0}$  differ by more than 10 %. This requires due to the high precision with which the value of  $C_{2,0}$  can be estimated with the Radio Science technique precise shape models for the interpretation of the results from the upcoming flyby in March 2010.

It is desirable to carry out measurements before MEX is occulted by Mars also with the Madrid (DSS-63) ground station. This measurements would enable the determination of parameter like the initial velocity, the scaling factor of the solar radiation pressure and a constant offset independently from the  $C_{2,0}$ . This would guarantee the small uncertainty in the  $C_{2,0}$  estimate.



## 5.2 Steins

On September 5, 2008 the Rosetta (ROS) spacecraft flew by at asteroid Steins (see section 5.2). The closest distance between ROS and Steins was 803 km at 18:38:20 (UTC). At the time of the Closest Approach (CA) the angle between the velocity component of ROS seen from Steins and the position vector from ROS (at transmitting time) to the ESA ground stations New Norcia and Cebreros (at receiving time) seen from barycenter of solar system was  $164^\circ$  and the relative flyby velocity between ROS and the asteroid Steins was about 8.6 km/s. These parameters are not optimal for a precise mass estimate. The small size of Steins with a mean radius of  $2.7 \pm 0.3$  km leads to  $GM = 1.5614 \times 10^{-5} \text{ km}^3/\text{s}^2$  (see section 5.2). Assuming a high density of  $3.0 \text{ g/cm}^3$ , a mass estimate is very unrealistic for Steins at this distance to ROS. In addition, no continuous recording was performed around CA and different ground stations were used. Recordings are available for the following time periods:

1. September 4, 2008 from 02:55:11.5 to 05:56:42.5 (GSRT) recorded at the 35 m ground station in New Norcia, Australia. One WoL manoeuvre was performed during this recording at 05:05:09.167 (SCEVT UTC), but also between this and the next recording at 07:27:00.0 (SCEVT UTC). It makes the use of this data set difficult, because both WoL manoeuvres have to be fitted to the data and recorded data are available only for one event. This is an additional source of uncertainty. Therefore this recording is not considered for analysis.
2. September 4, 2008 from 10:03:29.5 to 14:01:33.5 (GSRT) recorded also at New Norcia with a standard deviation  $\sigma = 10.7$  mHz.
3. September 5, 2008 from 02:52:48.5 to 11:54:02.5 (GSRT) recorded also at New Norcia with  $\sigma = 10.1$  mHz.
4. September 5, 2008 from 12:59:47.5 to 18:14:03.5 (GSRT) recorded at the 35 m ground station Cebreros in Avila, Spain with  $\sigma = 13.0$  mHz.
5. September 6, 2008 from 02:50:24.5 to 13:55:03.5 (GSRT) recorded again at New Norcia with  $\sigma = 10.1$  mHz.

Between the second and third measurement there is a gap of approximately 66 minutes and between the third and last measurement there is a gap of approximately 396 minutes. The second measurement terminates approximately 44 minutes before closest approach (Figure 5.16). The sky frequency was predicted using the initial state vector from the according SPICE kernel (see section A.1.4 in appendix) and the force model for ROS described in section 2.5. It remains a constant offset for each of the four used recordings of -24.94 mHz, -24.83 mHz, -26.66 mHz and -29.12 mHz, respectively.

The largest change in frequency due to the gravity field of Steins (see Figure 5.15) occurs at the time of the CA. No recording is available at this time. The change with a high density of  $3.0 \text{ g/cm}^3$  is computed to be approximately 0.16 mHz. The post-encounter frequency change  $f_\infty$  long after the CA is about 0.07 mHz. The noise of the

recorded data is for all recordings larger than 10 mHz. These are two orders larger than the expected frequency shift. It is obvious that it is impossible to resolve the mass of Steins from the recordings.

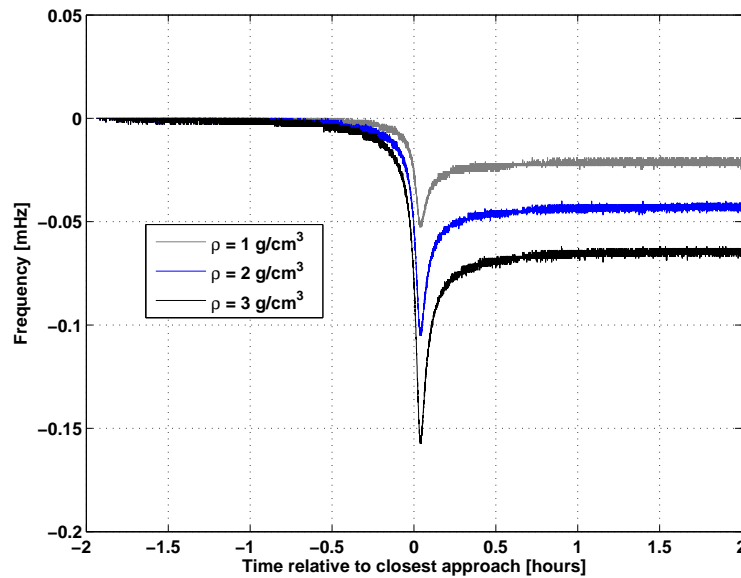


**Figure 5.15:** Frequency change caused by the gravitational attraction of asteroid Steins for three different bulk density assumptions  $\pm 2$  hours around CA. The frequency change corresponds to the uplink frequency of 7168640599.997583 Hz from the recording at Cebberos. The noise on the predicted changes is numerical. The predict is barely above the limit of numerical resolution.

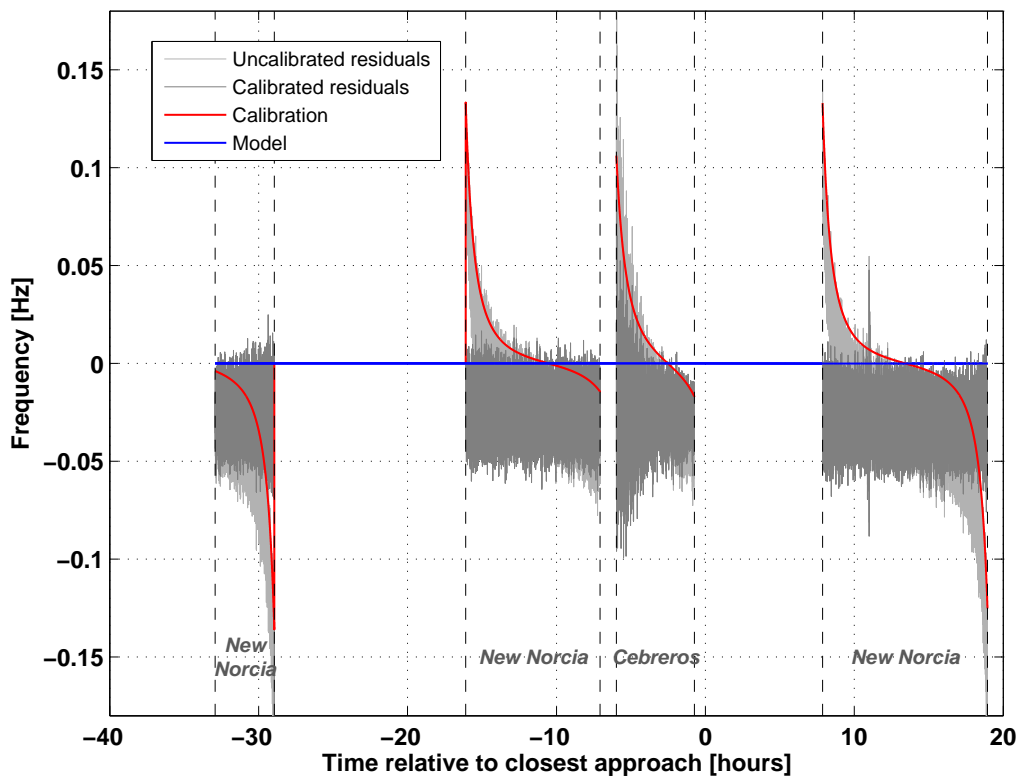


**Figure 5.16:** Frequency residuals of the recordings before and after the flyby at the Asteroid Steins.

## 5.3 Lutetia

On July 10 in 2010 the Rosetta (ROS) spacecraft will flyby at the asteroid Lutetia (see section 4.2 for physical properties of Lutetia). Due to constraints given by the flight dynamic section of ESOC, no continuous measurement covering the CA will be possible. High Gain Antenna (HGA) tracking will terminate minutes before CA and will resume about one hour after CA. This gap will limit the accuracy of the mass estimate of Lutetia in addition to other factors like flyby geometry and noise of the data. Simulations are carried out with different ranges of the gap in order to find the best configuration for the flyby and a prediction of the accuracy which can be obtained from the close flyby. The following flyby parameter are given by the flyby geometry:

- time of CA is 15:49:53 (UTC, Spacecraft event time),
- closest distance is 3055 km,
- angle between velocity component of ROS seen from Lutetia and position vector from ROS (at transmitting time) to ground station DSS-63 (at receiving time) seen from barycenter of solar system is  $171^\circ$ , and
- relative flyby velocity of ROS seen from Lutetia is about 15.0 km/s.

The entire range of the measurement is limited by the availability of continuous tracking of one ground station. Every ground station offers different bias sources of the measurement, for example ground station location uncertainty, but also thermal noise. If more than one ground station is used for the measurement the bias of each ground station has to be considered separately. This must be done carefully. It is difficult to avoid additional contributions on the measurement which would affect the estimation of the mass of Lutetia. It is of advantage to use only one ground station for the entire measurement around CA. In Figure 5.17 the elevation angle between the ground station and ROS for four ground station complexes is shown. Full visibility between ground station and spacecraft is given at an elevation angle larger than  $10^\circ$  above the horizon. This is the case for DSS-63 for about  $\pm 4$  h around Closest Approach (CA) which defines the time range for the following simulations.

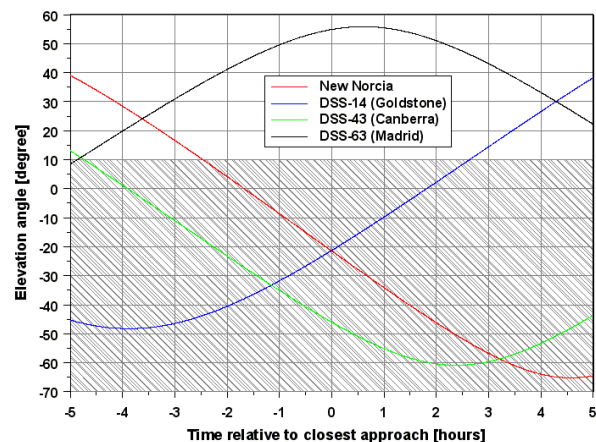


**Figure 5.17:** Ground station visibility during the time of the Lutetia flyby for the four main ground station complexes. An elevation angle of more than  $10^\circ$  indicates full visibility of the spacecraft from the ground station

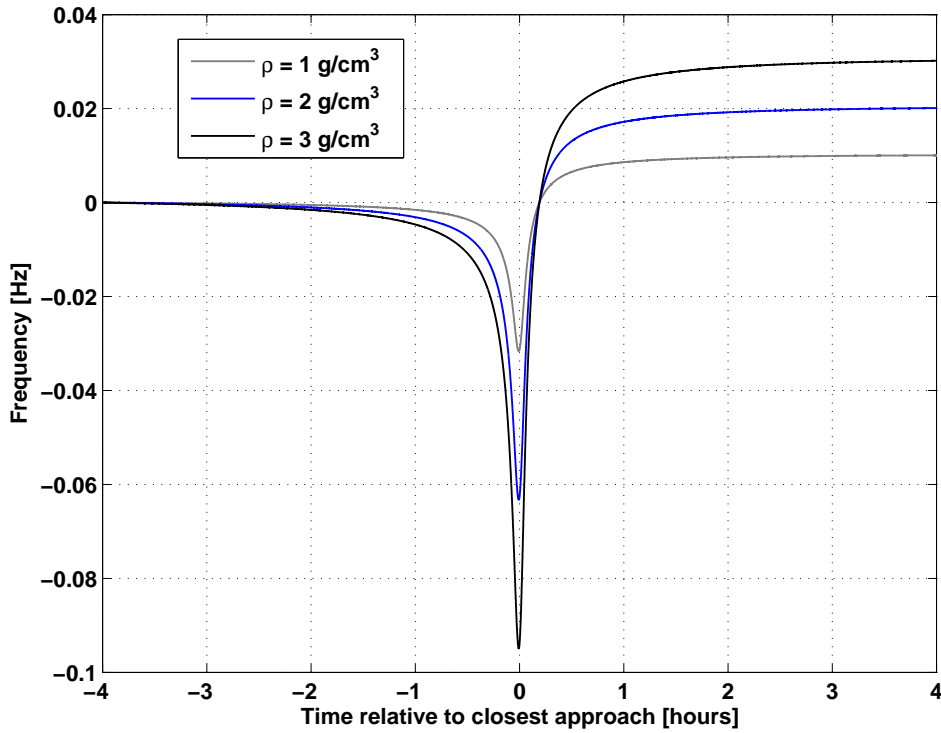


**Figure 5.18:** Frequency change caused by the gravitational attraction of asteroid Lutetia for three different bulk density assumptions. Frequency change corresponds to the uplink frequency of 7168398469.009392 Hz

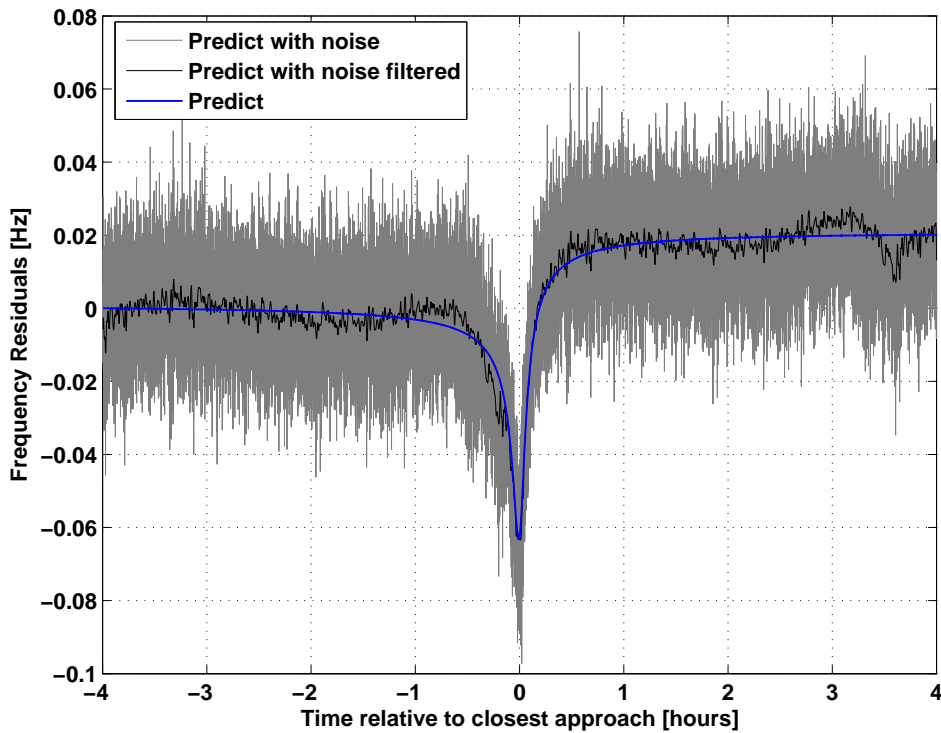


**Figure 5.19:** Frequency change caused by the gravitational attraction of asteroid Lutetia with bulk density of  $2 \text{ g/cm}^3$ . The noise is added from the TWO-WAY measurement of Doy 309, 2008. The frequency change corresponds to an uplink frequency of 7168398469.009392 Hz

The initial state vectors for the simulations are taken from SPICE-kernels (see section A.1.4) provided by ESOC. Those are containing the predicted position and velocity values for ROS. The density of Lutetia is not known. Densities ranging from 1 - 3 g/cm<sup>3</sup> are presumably possible. In Figure 5.18 the frequency change corresponding to an uplink frequency of 7168398469.009392 Hz is shown for this bulk density values. The maximum of the frequency change at CA ranges from -32 mHz to -95 mHz and the post-encounter frequency change ranges from 10 mHz to 30 mHz for 1 and 3 g/cm<sup>3</sup>, respectively.

The above mentioned uplink frequency is selected in order to add "real" noise to the simulated data in Figure 5.18 from a conducted measurement of ROS. The noise was extracted from the TWO-WAY measurement of Doy 309, 2008 (2008-11-04T07:22:10.5 - 2008-11-04T12:09:02.5). The standard deviation of the noise is  $\sigma = 0.0124$  Hz and has a mean value of zero.

The simulations are computed with a bulk density of  $\rho_s = 2$  g/cm<sup>3</sup>, the expected density of an asteroid of this type. Using a diameter of  $95.5 \pm 4.1$  km for Lutetia yields  $GM_L = 6.086 \times 10^{-2}$  km<sup>3</sup>/s<sup>2</sup> (product of the mass of Lutetia and the gravitational constant), which is supposed to be the only parameter in the fitting process. In Figure 5.19 the simulated frequency change with the added noise is shown.

The initial value for fitting  $GM$  of Lutetia was selected to be  $0.5 GM_L$ . In order to test if the results depend on the initial value, simulations have been done with randomized initial values. All produced the same result. Therefore the resulting value of  $GM$  is independent of the initial value.

The results from the simulations are summarized in Table 5.1. If no measurements after CA are available, the error in the  $GM$  estimate increases rapidly with increasing time between the end of the measurement and the time of CA. The error given for each simulation corresponds to one standard deviation based on the noise of the data and is computed via the covariance matrix (see section 2.8). Depending on the length of the measurement gap, the resulting  $GM$  value of Lutetia is highly overestimated or underestimated. Therefore a flyby scenario with measurements before CA only yields no reasonable estimate for  $GM$  and shows large errors due to the noise of the data.

Other flyby scenarios using measurements before and after CA lead to results for the  $GM$  value close to  $GM_L$ . The uncertainty of the estimate depends crucially on the measurement time available before CA. The difference between the  $GM$  value of Lutetia used for generating the simulated data and the estimated value is within one standard deviation caused by the noise of the data. It is obvious that the scenarios with the shortest gap around CA lead to the best estimate of the mass of Lutetia.

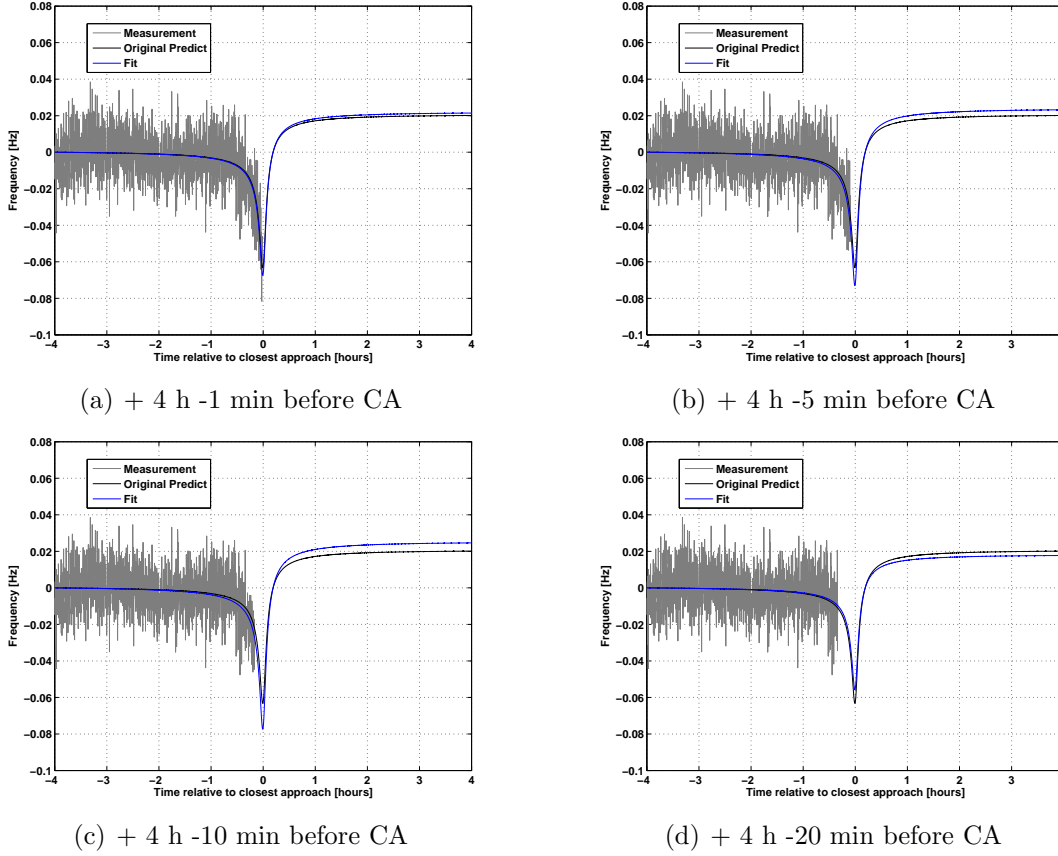


**Figure 5.20:** Different scenarios for the Lutetia flyby where "measurement" is the modeled frequency change with added realistic noise, "original predict" is the modeled frequency change without noise and "fit" is the fit on the noisy frequency resulting in the GM value for Lutetia.

The uncertainty of the mass estimate can be reduced by appropriate filter techniques (see section 2.9). Filters shall be applied carefully in order to reduce only the noise and not the information about the mass of Lutetia contained in the data. Therefore, different settings of the filters are tested. In order to find reliable values for the filter settings the model data of the minimum condition ( $\rho_s = 1 \text{ g/cm}^3$ ) and maximum condition ( $\rho_s = 3 \text{ g/cm}^3$ ) of the frequency change (see Figure 5.18) was filtered and compared with the unfiltered model data. The maximum limit of difference between filtered and unfiltered model data was defined to be 0.1 mHz.

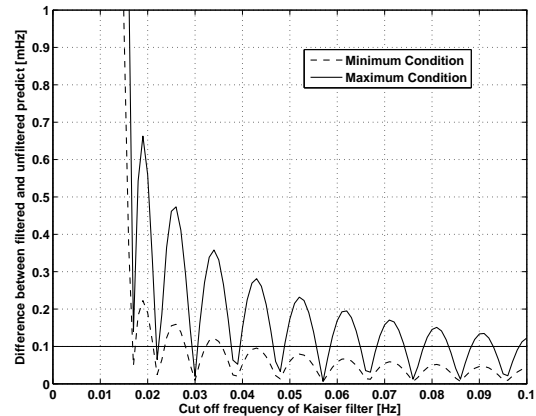


**Figure 5.21:** Difference between the frequency change of the filtered and unfiltered model data for the minimum ( $\rho_s = 1 \frac{\text{g}}{\text{cm}^3}$ ) and maximum condition ( $\rho_s = 3 \frac{\text{g}}{\text{cm}^3}$ ) for different cut-off frequencies  $f_c$  of the Kaiser filter.

Scenario	GM [ $\frac{10^{-2}\text{km}^3}{\text{s}^2}$ ]	Figure
$\pm 4$ h around CA, no gap	$6.120 \pm 0.180$ (2.9%)	5.19
$\pm 4$ h around CA filtered, no gap	$6.161 \pm 0.048$ (0.8%)	5.19
+ 4 h -1 min before CA, no post-encounter obs.	$6.488 \pm 0.433$ (6.7%)	5.20(a)
+ 4 h -5 min before CA, no post-encounter obs.	$7.026 \pm 0.643$ (9.1%)	5.20(b)
+ 4 h -10 min before CA, no post-encounter obs.	$7.448 \pm 0.909$ (12.2%)	5.20(c)
+ 4 h -20 min before CA, no post-encounter obs.	$5.364 \pm 1.415$ (26.4%)	5.20(d)
+ 4 h -1 min before and 1 h gap after CA	$6.029 \pm 0.203$ (3.4%)	5.23(a)
+ 4 h -5 min before and 1 h gap after CA	$6.027 \pm 0.216$ (3.6%)	5.23(b)
+ 4 h -10 min before and 1 h gap after CA	$5.992 \pm 0.222$ (3.8%)	5.23(c)
+ 4 h -10 min before and 30 min gap after CA	$6.077 \pm 0.212$ (3.5%)	5.23(e)
+ 4 h -10 min before and 2 h gap after CA	$6.239 \pm 0.265$ (4.2%)	5.23(f)
+ 4 h -20 min before and 1 h gap after CA	$5.887 \pm 0.226$ (3.9%)	5.23(d)
gap of $\pm 1.5$ h around CA	$5.911 \pm 0.247$ (4.2%)	5.23(g)
gap of $\pm 1$ h around CA	$5.911 \pm 0.227$ (3.8%)	5.23(h)

**Table 5.1:** Different flyby scenarios for ROS at asteroid Lutetia. Total simulation time is  $\pm 4$  hours (h) around Closest Approach (CA) with sample interval  $\Delta t = 10$  seconds. The simulated data are based on  $GM_L = 6.086 \times 10^{-2} \text{ km}^3/\text{s}^2$ . The error corresponds to one standard deviation.

In Figure 5.21 the maximum difference for different cut-off frequencies  $f_c$  of the Kaiser filter and in Figure 5.22 for different sample times  $\Delta t_{mov}$  of the moving average filter are shown. The resulting settings are  $f_c = 0.022$  and  $\Delta t_{mov} = 20$  s, which ensures that no information is deleted by filtering the data.

Applying both filters consecutively reduces the standard deviation of the noise from  $\sigma = 12.4$  mHz to  $\sigma_{filt} = 0.3$  mHz, which is a factor of 40. Based on the filtered data, the  $GM$  of Lutetia is  $6.161 \pm 0.048 \times 10^{-2} \text{ km}^3/\text{s}^2$ , which represents an error of 0.8% corresponding to one standard deviation. The small difference to the  $GM$  value of Lutetia used for generating the model data can be explained by the fluctuation of the signal caused by the noise. The amplitude of the model data is very well retraced by the filtered data, but the signal shows also fluctuations before and after CA which leads to the difference between the fitted  $GM$  and  $GM_L$  used for generating the simulated data.

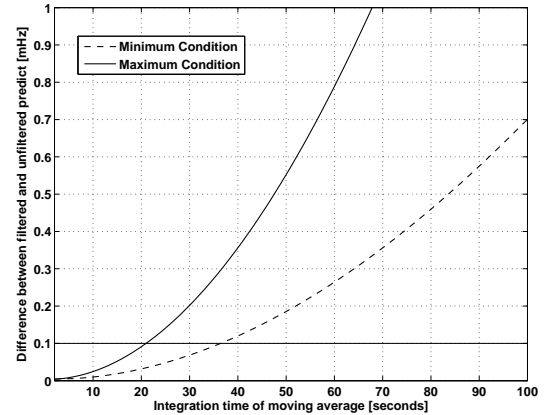
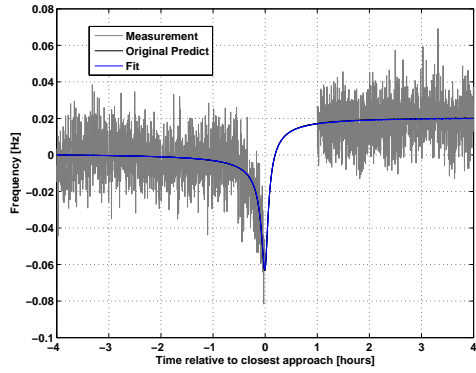
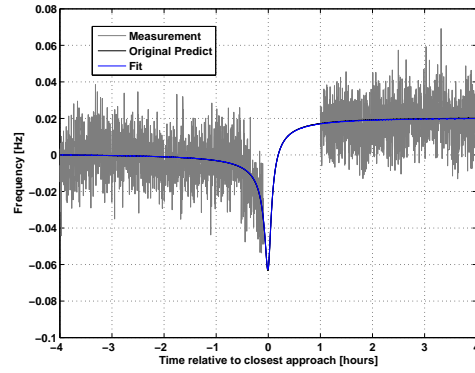


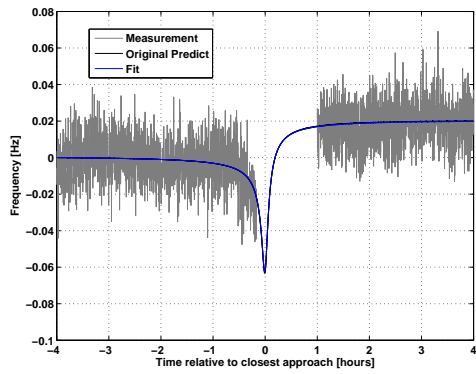
**Figure 5.22:** Difference between the frequency change of the filtered and unfiltered model data for the minimum ( $\rho_s = 1 \text{ g/cm}^3$ ) and maximum condition ( $\rho_s = 3 \text{ g/cm}^3$ ) for different sample times  $\Delta t_{mov}$  of the moving average filter.



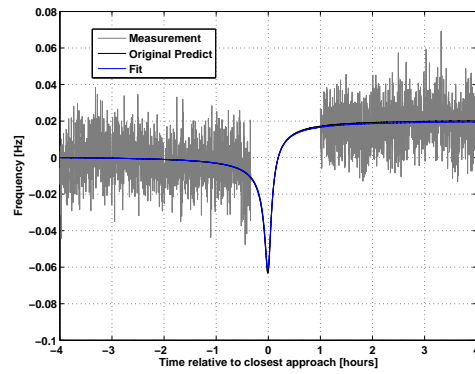
(a) gap of 1 min before and 1 h after CA



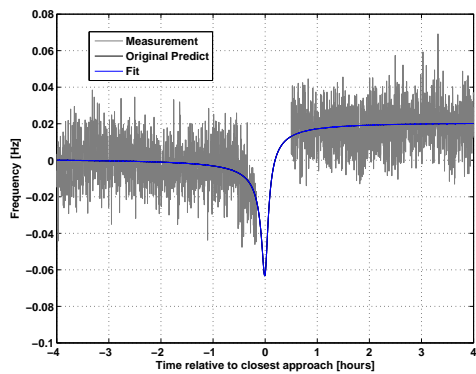
(b) gap of 5 min before and 1 h after CA



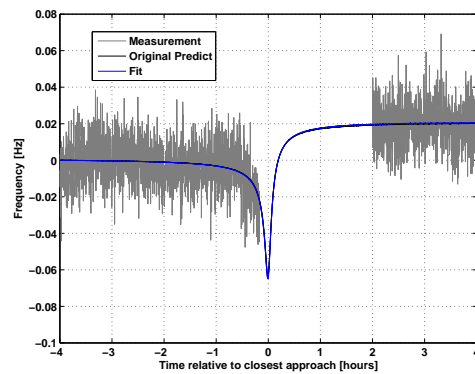
(c) gap of 10 min before and 1 h after CA



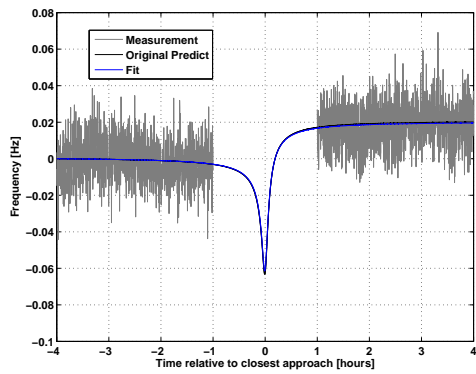
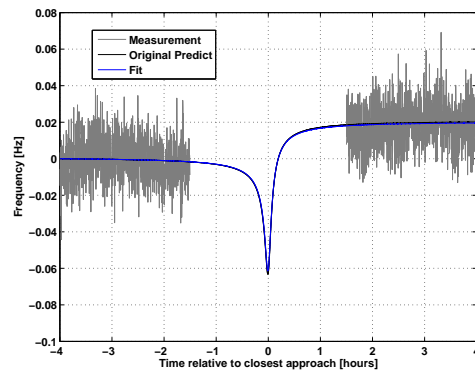
(d) gap of 20 min before and 1 h after CA



(e) gap of 10 min before and 0.5 h after CA



(f) gap of 10 min before and 2 h after CA

(g) gap of  $\pm 1$  h around CA(h) gap of  $\pm 1.5$  h around CA

**Figure 5.23:** Different scenarios of the Lutetia flyby with measurements before and after CA. "Measurement" is the modeled frequency change with added noise, "original predict" the modeled frequency change without noise and "fit" is the fit on the noisy frequency resulting in the GM value for Lutetia.

---

## Discussion and summary

---

The motivation for this PhD-thesis was to use the Radio Science technique during close flybys of Mars Express (MEX) at the Martian moon Phobos and of Rosetta (ROS) at the asteroid Steins and the future flyby at the asteroid Lutetia. The goal was to develop a strategy and tools for the determination of gravitational parameter of the bodies from planetary flybys using short-term observations.

A very precise and complex numerical model was developed based on an accurate force model for both the Mars Express and Rosetta spacecraft. The computed orbit was compared to very accurate orbit determinations provided by the flight control team at European Space Operation Center (ESOC) for both spacecrafts. It follows from the comparison that the accuracy of the computed orbit in this thesis is below 0.02 mm/s. This is very small compared to the Doppler velocity error of 0.26 mm/s in X-band (8.4 GHz) from the thermal noise of the ground station and the transponder phase noise.

Accurate models for extracting contributions from the Earth atmosphere on the radio signal were applied to the measured data. This contributions are ranging from 150 mHz at low elevation angles to 20 mHz at large elevation angles at X-band. With this calibration, the difference of the predicted frequency based on the relativistic Doppler to second order with the measured data is in the order of a few tenth of mHz typically between 10 mHz and 20 mHz at X-band. The ground station position was computed for this based on accurate models at centimeter level. The difference between model and observation is in the order of the total Doppler velocity error from the thermal noise and the transponder noise.

The signal-to-noise ratio of the data was improved by the applied filtering techniques by a factor of at least three. The uncertainty in the solution of mass estimates decreased with this filtering technique significantly.

A numerical stable least square techniques was used to fit not only gravitational parameter on the frequency residuals, but also the initial velocity of the spacecraft, the scaling factor of the solar radiation pressure and a constant offset. The latter parameter ensures that the remaining frequency shift is solely caused by the gravitational attraction of the perturbing body. It was shown that the models are sufficiently precise to analyze Radio Science measurements of close flybys. It was also shown that the method provides very small uncertainties in the mass estimates.

It was not possible to estimate the mass of the asteroid Steins from the flyby in 2008 from Rosetta. This was due to the small mass of Steins combined with a large flyby distance and non continuous tracking during the flyby. For these reasons other methods or more accurate models would also fail in estimating the mass of Steins.

The mass of Phobos was estimated from the first close flybys since twenty years at an accuracy not obtained from close flybys ever. The resulting mass is

$$GM = 0.7127 \pm 0.0021 \times 10^{-3} \text{ km}^3/\text{s}^2.$$

The small error of 0.3 % is a consequence of the high radio carrier frequency but also of the filtering technique and high numerical accuracy of the used models and software. The mass value is in agreement with solutions from long term observations using several years of tracking data. Its uncertainty is also comparable to that of long term solutions. The small error of long term observations is a consequence of the large number of data arcs included, but the error obtained in this thesis reflects the uncertainty due to the signal-to-noise ratio of the measurement.

In addition, the mass estimate of Phobos from the close flyby in 2008 improves the knowledge of the physical structure of Phobos. The bulk density  $\rho = 1.88 \pm 0.02 \text{ g/cm}^3$  was determined based on a volume estimate. Regardless which origin scenario is selected, i.e. which analogue material is used, Phobos shows a high porosity between 32 % and 36 % for CM chondrite and Martian crust as analogue material, respectively. This indicates re-accretion as a favorable formation process. Phobos macroporosity of  $18.6 \pm 0.7 \%$  is consistent with a fractured asteroid. An asteroid with this high porosity and macroporosity would have been destroyed during the capturing process by gravitational gradients. It appears though highly unlikely that Phobos is a captured asteroid. It follows from the results of the close flyby at Phobos that it is very likely that Phobos is formed from the collision of a body remaining from the formation process of Mars and a body formed in the asteroid belt. This scenario is consistent with the high porosity of Phobos and with its spectral properties.

The Mars Express spacecraft will perform an orbit change manoeuvre in February 2010. This will allow three consecutive flybys at Phobos. It was found that the closest flyby of the three on 3 March, 2010 at a distance of 62 km will be a unique scientific opportunity for estimating the  $C_{2,0}$  term of the gravity field of Phobos. This flyby was assigned to the Mars Express Radio Science Experiment based on the feasibility study carried out with the developed method.

In order to determine the uncertainty in the  $C_{2,0}$  estimate, noise from a real measurement was added to the predicted frequency change. These data were treated as a "real" observation. Filter were applied in order to reduce the signal-to-noise ratio. From the least square fit an uncertainty smaller than 1 % was obtained. With this small error it is possible to find out if Phobos has a layered structure or a uniform density distribution.

The flyby of Rosetta at the asteroid Lutetia which will be performed in 2010 was simulated in order to state the feasibility of the flyby for Radio Science measurements. It is likely to determine the mass of Lutetia from the flyby with an error smaller than 1%. From spectral measurements Lutetia is classified as a C-type or M-type asteroid. An accurate mass estimate as it was done for Phobos would help to distinguish between both asteroid types: C-type asteroids have small bulk densities like 253 Mathilde of  $1.34 \pm 0.2 \text{ g/cm}^3$ , whereas M-type asteroids like 16 Psyche of  $6.98 \pm 0.58 \text{ g/cm}^3$  have large bulk densities. Thus, the bulk density based on the mass estimate and a volume estimate from the camera onboard Rosetta would help to define the asteroid type of Lutetia.

The software package developed in this thesis is able to analyze Radio Science data obtained from short-term observations and estimate gravitational parameters of the perturbing body very precisely. It is also possible to predict the frequency changes of planned close flybys and perform feasibility studies serving as a basis of decision at future observations. The accuracy of the numerical models are accurate enough for analyzing and predicting Radio Science measurements with a precision close to the resolution of Radio Science experiments.



---

**Appendix**

---

**A.1 Used parameter****A.1.1 Masses of solar system bodies**

<b>Body / System</b>	<b>GM [<math>\frac{\text{km}^3}{\text{s}^2}</math>]</b>
Sun	132712440040.944000
Mercury	22032.090000
Venus	324858.592000
Earth	398600.436233
Earth-Moon	403503.236310
Moon	4902.800076
Mars	42828.375214
Jupiter	126712764.800000
Saturn	37940585.200000
Uranus	5794548.600000
Neptune	6836535.000000
Pluto	977.000000
Deimos	$0.98 \times 10^{-4}$

**Table A.1:** *Masses of Solar System Bodies from Folkner et al. [2008] and of Deimos from Jacobson [2008]*

### A.1.2 MEX

The optical parameter of MEX are listed in the following table based on information from *Morley* [2004], whereby *ABSC* is the absorption coefficient, *DIFR* the ratio diffusive/(diffusive + specular) with (diffusive + specular) = 1 - *ABSC* and the reflection coefficient  $\varepsilon$ .

Surface	$\alpha$	$\delta$	$\varepsilon$	Area [m <sup>2</sup> ]
+ X	0.474	0.504	0.022	2.686
- X	0.602	0.383	0.015	2.686
+ Y	0.621	0.371	0.008	2.686
- Y	0.712	0.282	0.006	2.686
+ Z	0.829	0.171	0.000	2.890
- Z	0.566	0.311	0.123	2.890
solar array	0.677	0.130	0.194	6.109

**Table A.2:** *Optical properties of MEX from Morley [2004]*

### A.1.3 ROS

The optical parameter of ROS are listed in the following table based on information from *Morley* [2008], whereby *ABSC* is the absorption coefficient, *DIFR* the ratio diffusive/(diffusive + specular) with (diffusive + specular) = 1 - *ABSC* and the reflection coefficient  $\varepsilon$ .

Surface	$\alpha$	$\delta$	$\varepsilon$	Area [m <sup>2</sup> ]
+ X	0.909	0.091	0.000	5.150
- X	0.853	0.136	0.011	5.150
+ Y	0.795	0.205	0.000	5.408
- Y	0.750	0.250	0.000	5.408
+ Z	0.916	0.084	0.000	4.200
- Z	0.889	0.080	0.031	4.200
HGA	0.930	0.070	0.000	3.800
solar array	0.840	0.313	0.110	32.310

**Table A.3:** *Optical properties of the ROS spacecraft from Morley [2008]*

## A.1.4 Used SPICE-kernels

### A.1.4.1 General kernels

- `NAIF0009.TLS`  
File storing the occurrences of leapseconds
- `de421.bsp`  
Contains ephemeris data for planet barycenters, and for the sun, earth and moon mass centers (see *Folkner et al.* [2008] for more information).
- `EARTHSTNS_ITRF93_050714.BSP`  
Contains ephemeris data for NASA DSN stations relative to the terrestrial reference frame label 'ITR93'.
- `EARTH_TOPO_050714.TF`  
Frame kernel for the topocentric reference frames for the Deep Space Network (DSN) stations.
- `NEW_NORCIA.BSP`  
Contains ephemeris data for the ESA New Norcia station.
- `NEW_NORCIA_TOPO.TF`  
Frame kernel for the topocentric reference frame for the ESA 35m tracking antenna at New Norcia.
- `EARTHFIXEDIAU.TF`  
This kernel makes the `IAU_EARTH` frame coincide with the earth fixed reference frame.
- `EARTHFIXEDITRF93.TF`  
This kernel makes the `ITRF93` frame coincide with the earth fixed reference frame.
- `PCK00008.TPC`  
PCK file containing the size, shape, radii and orientation constants for planets, satellites, Sun and some asteroids.
- `EARTH_000101_081229_081008.BPC`  
PCK file containing the orientation of the Earth as a function of time for the from 01 January 2000 until 29 December 2008. From 29 December 2008 the information contained in the file corresponds to predicted data. The rotational effects included are precession, nutation, rotation through true sidereal time, polar motion and nutation corrections.

#### A.1.4.2 MEX specific kernels

- `MAR080S.BSP`  
Contains the ephemeris data from JPL, for Phobos and Deimos (see *Jacobson* [2008] for more information).
- `MEX_V10.TF`  
Frame kernel containing the complete set of frame definitions for MEX and Beagle-2 Lander (BEAGLE2) including definitions for the MEX fixed and MEX science instrument frames and BEAGLE2 fixed, and landing site local frames. This kernel also contains NAIF ID/name mapping for the MEX and BEAGLE2 instruments.
- `ORMM__080701000000_00514.BSP`  
Contains MEX reconstructed ephemeris for entire July 2008.
- `ORMC__2010_nigth_side_00001.BSP`  
Contains MEX spacecraft long term operational Mars centric ephemeris optimized for Phobos flybys in 2010.
- `ATNM_PTR00261_050212_001.BC`  
`ATNM_PTR00271_050311_001.BC`  
`ATNM_PTR00381_060115_001.BC`  
`ATNM_PTR00401_060312_001.BC`  
`ATNM_PTR00744_080630_003.BC`  
`ATNM_PTR00756_080727_001.BC`  
Contains Mars Express predicted attitude information.

#### A.1.4.3 ROS specific kernels

- `ORHR_____00077.BSP`  
Contains Rosetta spacecraft predicted and reconstructed cruise ephemeris. Spans the cruise phase, from launch to comet rendezvous maneuver.
- `ORHS_____00074.BSP`  
Contains ephemeris for the asteroid Lutetia
- `earth_070425_370426_predict.bpc`  
PCK file containing the orientation of the Earth from 25 April 2007 to 17 July 2037 as predicted data. The rotational effects included are precession, nutation, rotation through true sidereal time, polar motion and nutation corrections.
- `ATPR_P080902000000_00067.BC`  
Contains Rosetta predicted attitude information.

## A.2 Tectonic plate motion

Plate Name	$\Omega_x$ [rad/My.]	$\Omega_y$ [rad/My.]	$\Omega_z$ [rad/My.]
Pacific	-0.001510	0.004840	-0.009970
Cocos	-0.010425	-0.021605	0.010925
Nazca	-0.001532	-0.008577	0.009609
Caribbean	-0.000178	-0.003385	0.001581
South America	-0.001038	-0.001515	-0.000870
Antarctica	-0.000821	-0.001701	0.003706
India	0.006670	0.000040	0.006790
Australia	0.007839	0.005124	0.006282
Africa	0.000891	-0.003099	0.003922
Arabia	0.006685	-0.000521	0.006760
Eurasia	-0.000981	-0.002395	0.003153
North America	0.000258	-0.003599	-0.000153
Juan de Fuca	0.005200	0.008610	-0.005820
Philippine	0.010090	-0.007160	-0.009670
Rivera	-0.009390	-0.030960	0.012050
Scotia	-0.000410	-0.002660	-0.001270

**Table A.4:** Cartesian rotation vector for each plate using the NNR-NUVEL1A kinematic plate model (no net rotation) (IERS [2009])

## A.3 Coefficient tableau of integration method

0	0	0	0	0	0	0	0
$\frac{1}{5}$	$\frac{1}{5}$	0	0	0	0	0	0
$\frac{3}{10}$	$\frac{3}{40}$	$\frac{9}{40}$	0	0	0	0	0
$\frac{4}{5}$	$\frac{44}{45}$	$-\frac{56}{15}$	$\frac{32}{9}$	0	0	0	0
$\frac{8}{9}$	$\frac{19372}{6561}$	$-\frac{25360}{2187}$	$\frac{64448}{6561}$	$-\frac{212}{729}$	0	0	0
1	$\frac{9017}{3168}$	$-\frac{355}{33}$	$\frac{46732}{5247}$	$\frac{49}{176}$	$-\frac{5103}{18656}$	0	0
1	$\frac{35}{384}$	0	$\frac{500}{1113}$	$\frac{125}{192}$	$-\frac{2187}{6784}$	$\frac{11}{84}$	0
0	$\frac{5179}{57600}$	0	$\frac{7571}{16695}$	$\frac{393}{640}$	$-\frac{92097}{339200}$	$\frac{187}{2100}$	$\frac{1}{40}$
0	$\frac{35}{384}$	0	$\frac{500}{1113}$	$\frac{125}{192}$	$-\frac{2187}{6784}$	$\frac{11}{84}$	0

**Table A.5:** The coefficient tableau of the RK5(4) integration method

## A.4 Acceleration from unnormalized gravity coefficients

In the following the equations in order to compute the acceleration caused by the gravity potential of body using unnormalized gravity coefficients  $C_{n,m}$  and  $S_{n,m}$  according to *Montenbruck and Gill* [2000] are shown.

### A.4.1 Recursions

The unnormalized recurrence coefficients  $V_{n,m}$  and  $W_{n,m}$  can be computed according to *Montenbruck and Gill* [2000]

$$V_{m,m} = \frac{\bar{R}}{r^2} \cdot (2m - 1) (x \cdot V_{m-1,m-1} - y \cdot W_{m-1,m-1}) \quad (\text{A.1a})$$

$$W_{m,m} = \frac{\bar{R}}{r^2} \cdot (2m - 1) (x \cdot W_{m-1,m-1} + y \cdot V_{m-1,m-1}) \quad (\text{A.1b})$$

$$V_{n,m} = \frac{\bar{R}}{r^2} \cdot \frac{1}{n-m} ((2n-1) \cdot z \cdot V_{n-1,m} - (n+m-1) \cdot \bar{R} \cdot V_{n-2,m}) \quad (\text{A.1c})$$

$$W_{n,m} = \frac{\bar{R}}{r^2} \cdot \frac{1}{n-m} ((2n-1) \cdot z \cdot W_{n-1,m} - (n+m-1) \cdot \bar{R} \cdot W_{n-2,m}) \quad (\text{A.1d})$$

with the initial conditions

$$V_{0,0} = \frac{\bar{R}}{r} \quad \text{and} \quad W_{0,0} = 0 \quad (\text{A.2})$$

In order to compute the all  $V_{n,m}$  and  $W_{n,m}$  the zonal terms have to be computed first and all further computations should be done according to the scheme shown in figure A.1.

### A.4.2 Acceleration

With the above shown unnormalized recurrence coefficients the resulting acceleration can be computed via the following equation using unnormalized gravity coefficients  $C_{n,m}$  and  $S_{n,m}$ .

$$\ddot{x} = \sum_{n=0}^{\infty} \sum_{m=0}^n \ddot{x}_{n,m}, \quad \ddot{y} = \sum_{n=0}^{\infty} \sum_{m=0}^n \ddot{y}_{n,m}, \quad \ddot{z} = \sum_{n=0}^{\infty} \sum_{m=0}^n \ddot{z}_{n,m} \quad (\text{A.3})$$

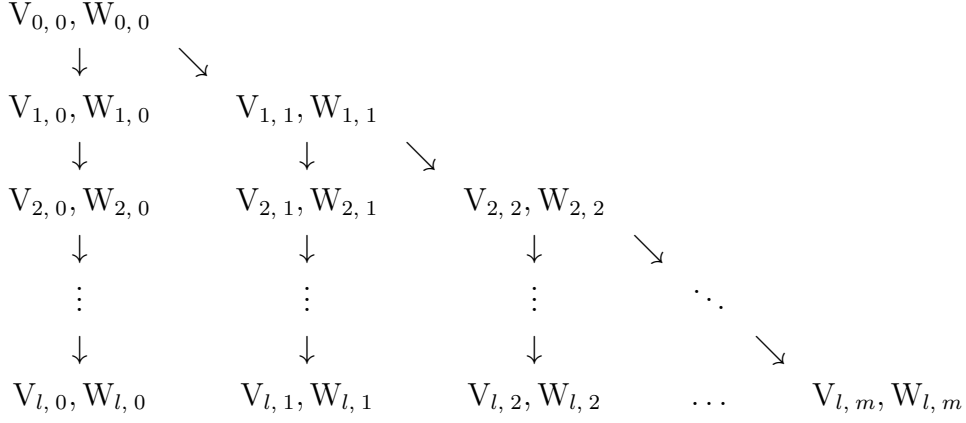


**Figure A.1:** Execution scheme for recurrence coefficients computation.

The parital accelerations are (see *Montenbruck and Gill* [2000])

$$\ddot{x}_{n,m} = -\frac{GM}{R^2} \cdot C_{n,0} \cdot V_{n+1,1} \quad (\text{A.4})$$

$$\begin{aligned} \ddot{x}_{n,m} \stackrel{m \geq 0}{=} & -\frac{1}{2} \frac{GM}{R^2} \left( C_{n,m} \cdot V_{n+1,m+1} + S_{n,m} \cdot W_{n+1,m+1} \right. \\ & \left. - (n-m+2)(n-m+1) \left( C_{n,m} \cdot V_{n+1,m-1} + \right. \right. \\ & \left. \left. + S_{n,m} \cdot W_{n+1,m-1} \right) \right) \end{aligned} \quad (\text{A.5})$$

$$\ddot{y}_{n,m} = -\frac{GM}{R^2} \cdot C_{n,0} \cdot W_{n+1,1} \quad (\text{A.6})$$

$$\begin{aligned} \ddot{y}_{n,m} \stackrel{m \geq 0}{=} & -\frac{1}{2} \frac{GM}{R^2} \left( C_{n,m} \cdot W_{n+1,m+1} - S_{n,m} \cdot V_{n+1,m+1} \right. \\ & \left. + (n-m+2)(n-m+1) \left( C_{n,m} \cdot W_{n+1,m-1} - \right. \right. \\ & \left. \left. - S_{n,m} \cdot V_{n+1,m-1} \right) \right) \end{aligned} \quad (\text{A.7})$$

$$\ddot{z}_{n,0} = -\frac{GM}{R^2} (n+1) \cdot C_{n,0} \cdot V_{n+1,0} \quad (\text{A.8})$$

$$\ddot{z}_{n,m} \stackrel{m \geq 0}{=} -\frac{GM}{R^2} (n-m+1) \cdot (C_{n,m} \cdot V_{n+1,m} + S_{n,m} \cdot W_{n+1,m}). \quad (\text{A.9})$$

## A.5 Media correction

### A.5.1 Ionospheric media correction terms

With the following equations the corrected frequency residuals from the ionospheric correction can be computed for different down- and uplink configurations (*Morabito and Asmar [1995]*):

- One-way S-band downlink (2.3 GHz):

$$\Delta f_c^S(t_j) = \Delta f^S(t_j) - f_{ion}^S(t_j) \quad (\text{A.10})$$

- One-way S-band downlink (2.3 GHz):

$$\Delta f_c^X(t_j) = \Delta f^X(t_j) - \frac{3}{11} f_{ion}^S(t_j) \quad (\text{A.11})$$

- Two-way X-band uplink and X-band downlink:

$$\Delta f_c^X(t_j) = \Delta f^X(t_j) - \frac{3}{11} \left( f_{ion}^S(t_j) - \frac{840}{749} f_{ion}^S(t_j - t_r) \right) \quad (\text{A.12})$$

- Two-way X-band uplink and S-band downlink:

$$\Delta f_c^X(t_j) = \Delta f^X(t_j) - f_{ion}^S(t_j) - \frac{3}{11} \frac{840}{749} f_{ion}^S(t_j - t_r) \quad (\text{A.13})$$

Here  $t_r$  is the two-way light time. In the equations for the two-way correction the first term accounts for the downlink and the second one accounts for the uplink and the effect of the uplink onto the downlink signal.

### A.5.2 Ionospheric correction using the differential Doppler

The correction of the contribution by the ionosphere of the Earth and the interplanetary plasma can also be computed via the differential Doppler defined as follows:

$$\delta f = f_S - \frac{3}{11} f_X. \quad (\text{A.14})$$

The differential Doppler is also

$$\delta f = -\frac{1}{2c} \frac{1}{4\pi^2} \frac{e^2}{m_e \epsilon_0} \left( \frac{1}{f_S^2} - \frac{1}{f_X^2} \right) f_S \frac{dI}{dt} \quad (\text{A.15})$$

and therefore the temporal change of the electron content is

$$\frac{dI}{dt} = -\left( \frac{1}{2c} \frac{1}{4\pi^2} \frac{e^2}{m_e \epsilon_0} \right)^{-1} \frac{\delta f}{f_S} \left( \frac{1}{f_S^2} - \frac{1}{f_X^2} \right)^{-1} \quad (\text{A.16})$$

The plasma correction for S-band and X-band are then according to *Pätzold* [2004]:

$$f_{S,calib} = f_S + \frac{1}{2c} \frac{1}{4\pi^2} \frac{e^2}{m_e \epsilon_0} \frac{1}{f_S} \frac{dI}{dt} \quad (\text{A.17})$$

$$f_{X,calib} = f_X + \frac{1}{2c} \frac{1}{4\pi^2} \frac{e^2}{m_e \epsilon_0} \frac{1}{f_X} \frac{dI}{dt} \quad (\text{A.18})$$

Using equation A.16 and the general relation

$$\frac{f_S}{f_X} = \frac{3}{11} \quad (\text{A.19})$$

the calibration can now be written as

$$\Delta f_{X, Plasma} = -\delta f \frac{33}{112} \quad (\text{A.20})$$

$$\Delta f_{S, Plasma} = -\delta f \frac{121}{112}. \quad (\text{A.21})$$



---

## Bibliography

---

- Abramowitz, M. and I. Stegun**, *Handbook of Mathematical Functions*, Dover Publ., 1970.
- Agnew, D. C.**, Earth tides, in *Geodesy*, edited by T. Herring, vol 3 of *Treatise on Geophysics*, 163–195, Elsevier, Amsterdam, 2007.
- Andert, T. P.**, Das Schwerfeld des Marsmondes Phobos und die Wirkung des Schwerfeldes bei nahen Vorbeiflügen von Mars Express, Diplomarbeit am Institut für Geophysik und Meteorologie an der Universität zu Köln, 2004.
- Ashby, N.**, Relativity in the Global Positioning System, *Living Reviews in Relativity*, 2003.
- Aster, R. C., B. Borchers and C. Thurber**, *Parameter Estimation and Inverse Problems*, Elsevier Academic Press, 2005.
- Barucci, M. A. et al.**, Asteroid target selection for the new Rosetta mission baseline, 21 Lutetia and 2867 Steins, *Astron. Astrophys.*, 430, 313–317, 2005.
- Battin, R. H.**, *An Introduction to the Mathematics and Methods of Astrodynamics*, American Institute of Aeronautics and Astronautics, Inc., 3. Auflage, 1987.
- Besse, S., O. Groussin, L. Jorda, P. Lamy, M. Kaasalainen, G. Gesquiere, E. Remy and Osiris Team**, 3-Dimensional Reconstruction of Asteroid 2867 Steins, in *Lunar and Planetary Institute Science Conference Abstracts*, vol 40 of *Lunar and Planetary Institute Science Conference Abstracts*, 1545, 2009.
- Bibring, J.-P., Y. Langevin, A. Soufflot, C. Combes and C. Cara**, Results from the ISM experiment, *Nature*, 341, 591–593, 1989.
- Birlan, M. et al.**, Near-IR spectroscopy of asteroids 21 Lutetia, 89 Julia, 140 Siwa, 2181 Fogelin, and 5480 (1989YK8), potential targets for the Rosetta mission, remote observations campaign on IRTF, *New Astronomy*, 9, 343, 2004.

- Brandt, S.**, *Data Analysis*, Springer-Verlag, New York, Berlin, Heidelberg, 3. Auflage, 1998.
- Britt, D. T. and G. J. Consolmagno**, The Porosity of Dark Meteorites and the Structure of Low-Albedo Asteroids, *Icarus*, 146, 213–219, 2000.
- Britt, D. T. et al.**, Asteroid Density, Porosity and Structure, in *Asteroids III*, edited by W. F. Bottke JR. and others, 485–500, Univ. of Ariz. Press, 2002.
- Burchell, M. J. and J. Leliwa-Kopystynski**, The Large Crater on Asteroid Steins: Is it Abnormally Large?, in *Lunar and Planetary Institute Science Conference Abstracts*, vol 40 of *Lunar and Planetary Institute Science Conference Abstracts*, 1525, 2009.
- Burns, J. A.**, Contradictory Clues as to the Origin of the Martian Moons, in *Mars*, edited by H. Kiefer et al., 1283–1301, Univ. of Ariz. Press, 1992.
- Buttkus, B.**, *Spectral analysis and filter theory in applied geophysics*, Springer Verlag, Berlin, Heidelberg, 1. Auflage, 2000.
- Chao, C. C.**, A Model for Tropospheric Calibration from Daily Surface and Radiosonde Balloon Measurements, *Technical Memorandum 391-350*, 1972.
- Chicarro, A., P. Martin and R. Trautner**, The Mars Express Mission: An Overview, in *Mars Express The Scientific Payload*, edited by A. W. E. P. Division, 3–16, ESA, ESA Publ. Division, 2004.
- Christensen, E. J., G. H. Born, C. E. Hildebrand and B. G. Williams**, The mass of Phobos from Viking flybys, *J. Geophys. Res.*, 4, 555–557, 1977.
- Craddock, R. A.**, The Origin of PHOBOS and Deimos, in *Lunar and Planetary Institute Science Conference Abstracts*, vol 25 of *Lunar and Planetary Inst. Technical Report*, 293, 1994.
- Cunningham, L. E.**, On the Computation of the Spherical Harmonic Terms Needed during the Numerical Integration of the Orbital Motion of an Artificial Satellite, *Celestial Mechanics*, 2, 207–216, 1970.
- Dehant, V. and P. M. Mathews**, Earth rotation variations, in *Geodesy*, edited by T. Herring, vol 3 of *Treatise on Geophysics*, 295–349, Elsevier, Amsterdam, 2007.
- del Rio, J. D.**, *Mars Express, Auxiliary Data Conversion into SPICE Kernels and Distribution*, ESA, issue 1, revision 9 Auflage, 2006.
- Dorfmueller, T. et al.**, *Lehrbuch der Experimentalphysik, Band 1, Mechanik, Relativität, Wärme*, Walter de Gruyter, Berlin, New York, 11. Auflage, 1998.
- Dormand, J. R. and P. J. Prince**, A Family of Embedded Runge-Kutta Formulae, *Journal of computational and applied mathematics*, 6, 19–26, 1980.

- Dormand, J. R. and P. J. Prince**, High Order Embedded Runge-Kutta Formulae, *Journal of computational and applied mathematics*, 7, 67–75, 1981.
- Dotto, E., D. Perna, S. Fornasier, I. N. Belskaya, M. A. Barucci, V. G. Shevchenko, Y. N. Krugly, N. M. Gaftonyuk, I. A. Tereschenko, F. Scipioni and F. de Luise**, Photometric and spectroscopic investigation of 2867 Steins, target of the Rosetta mission. Ground-based results prior to the Rosetta fly-by, *A&A*, 494, L29–L32, 2009.
- Duxbury, T. C.**, The figure of Phobos, *Icarus*, 78, 169–180, 1989.
- Duxbury, T. C.**, An Analytic Model for the Phobos Surface, *Planet. Space Sci.*, 39, 355–376, 1991.
- Duxbury, T. C. and J. D. Callahan**, Phobos and Deimos Control Networks, *Icarus*, 77, 275–286, 1989.
- ESA**, Mars Express, [http://www.esa.int/SPECIALS/Mars\\_Express/index.html](http://www.esa.int/SPECIALS/Mars_Express/index.html), 2009a.
- ESA**, Rosetta, <http://www.esa.int/esaMI/Rosetta/index.html>, 2009b.
- Folkner, W. M., J. G. Williams and D. H. Boggs**, The planetary and Lunar Ephemeris DE 421, *JPL IOM*, 343R-08-003, 2008.
- Gander, W.**, *Computermathematik*, Birkhäuser Verlag, Basel, 1985.
- Gehrke, W.**, *Fortran 90 Referenzhandbuch*, Carl Hanser Verlag, München, Wien, 1. Auflage, 1991.
- Gendrin, A., Y. Langevin and S. Erard**, ISM observation of Phobos reinvestigated: Identification of a mixture of olivine and low-calcium pyroxene, *Journal of Geophysical Research (Planets)*, 110, 4014, 2005.
- Gladman, B., J. J. Kavelaars, M. Holman, P. D. Nicholson, J. A. Burns, C. W. Hergenrother, J.-M. Petit, B. G. Marsden, R. Jacobson, W. Gray and T. Grav**, Discovery of 12 satellites of Saturn exhibiting orbital clustering, *Nature*, 412, 163–166, 2001.
- Gondet, B., J.-P. Bibring, Y. Langevin, F. Poulet and S. L. Murchie**, Phobos Observations by the OMEGA/Mars Express Hyperspectral Imager, in *Lunar and Planetary Institute Conference Abstracts*, vol 39 of *Lunar and Planetary Institute Conference Abstracts*, 1832, 2008.
- Guthmann, A.**, *Einführung in die Himmelsmechanik und Ephemeridenrechnung*, BI-Wiss.-Verlag, 1994.
- Häusler, B.**, Radio Science Messungen im Sonnensystem mit einer Einführung in die Theorie der Gravitation, *Forschungsbericht, LRT-WE-9-FB-2*, 2002.
- Häusler, B.**, Dynamik und Regelung von Satelliten, *Lecture Notes*, 2008a.

- Häusler, B.**, Satellitensysteme, *Lecture Notes*, 2008b.
- Häusler, B.**, Weltraumphysik, *Lecture Notes*, 2008c.
- Häusler, B. et al.**, Venus Express Radio Science Experiment VeRa: Reference Systems and Techniques Used for the Simulation and Prediction of Atmospheric and Ionospheric Sounding Measurements at Planet Venus, *Forschungsbericht, LRT-WE-9-FB-4*, 2003.
- Hennig, T.**, Präzise Positionsbestimmung der Bodenstationen des DSN und der ESA, Diplomarbeit am Institut für Raumfahrttechnik an der Universität der Bundeswehr, München, 2008.
- Hildebrand, A. R., P. J. A. McCausland, P. G. Brown, F. J. Longstaffe, S. D. J. Russell, E. Tagliaferri, J. F. Wacker and M. J. Mazur**, The fall and recovery of the Tagish Lake meteorite, *Meteoritics and Planetary Science*, *41*, 407–431, 2006.
- Hull, T. E., W. H. Enright, B. M. Fellen and A. E. Sedgwick**, Comparing Numerical Methods for Ordinary Differential Equations, *SIAM J. Numer. Anal.*, *9*, 603–637, 1972.
- IERS**, International Earth Rotation and Reference Systems Service, <http://itrf.ensg.ign.fr>, 2009.
- Ifadis, I.**, The Atmospheric Delay of Radio Waves: Modeling the Elevation Dependence on a Global Scale, *Technical Report no. 38L*, 1986.
- Jacobson, R. A.**, The Orbits of the Martian Satellites, in *Division for Planetary Sciences Abstracts*, Division for Planetary Sciences Abstracts, 2008.
- Janes, H. W., R. B. Langley and S. P. Newby**, Analysis of tropospheric delay prediction models - Comparisons with ray-tracing and implications for GPS relative positioning, *Bulletin Geodesique*, *65*, 151–161, 1991.
- Jewitt, D. and N. Haghighipour**, Irregular Satellites of the Planets: Products of Capture in the Early Solar System, *ARA&A*, *45*, 261–295, 2007.
- JPL**, JPL Small-Body Database Browser, <http://ssd.jpl.nasa.gov/sbdb.cgi>, 2009.
- Juup, D. L. B. and K. Vozoff**, Stable Iterative Methods for the Inversion of Geophysical Data, *J. Geophys. Res.*, *42*, 957–976, 1975.
- Kautzleben, H.**, Kugelfunktionen, in *Geomagnetismus und Aeronomie*, edited by G. Fanselau, B. G. Teubner, Leipzig, 1965.
- Kertz, W.**, *Einführung in die Geophysik*, vol I und II, Spektrum Akademischer Verlag, Heidelberg, Berlin, Oxford, 1995.

- Kieffer, H. H., B. M. Jakosky and C. W. Snyder**, The Planet Mars: From Antiquity To The Present, in *Mars*, edited by H. Kieffer et al., 1–34, Univ. of Ariz. Press, 1992.
- Klobuchar, J. A.**, A First Order, Worldwide, Ionospheric, Time-Delay Algorithm, *Air Force Surveys in Geophysics*, 324, 1975.
- Kolyuka, Y. F., A. E. Ephimov, S. M. Kudryavtsev, O. K. Margorin, V. P. Tarasov and V. F. Tikhonov**, Improved determination of the gravitational constant of PHOBOS on the basis of Phobos-2 trajectory tracking, *Pisma Astronomicheskii Zhurnal*, 16, 396–400, 1990.
- Konopliv, A. S., C. F. Yoder, E. M. Standish, D.-N. Yuan and W. L. Sjogren**, A global solution for the Mars static and seasonal gravity, Mars orientation, Phobos and Deimos masses, and Mars ephemeris, *Icarus*, 182, 23–50, 2006.
- Kopka, H.**, *Latex, Einführung*, Addison-Wesley Verlag, München, 2000.
- Lainey, V., V. Dehant and M. Pätzold**, First numerical ephemerides of the Martian moons, *Astron. Astrophys.*, 465, 1075–1084, 2007.
- Lamy, P. L., M. Kaasalainen, S. Lowry, P. Weissman, M. A. Barucci, J. Carvano, Y.-J. Choi, F. Colas, G. Faury, S. Fornasier, O. Groussin, M. D. Hicks, L. Jorda, A. Kryszczyńska, S. Larson, I. Toth and B. Warner**, Asteroid 2867 Steins. II. Multi-telescope visible observations, shape reconstruction, and rotational state, *A&A*, 487, 1179–1185, 2008.
- Lipschutz, S.**, *Lineare Algebra*, McGraw-Hill Company Europe, London, 4. Auflage, 1990.
- Marty, J., G. Balmino, J. Duron, P. Rosenblatt, R. Biancale and V. Dehant**, Precise orbit determination and planetary gravity field determination using GINS software, in *FIRST EUROPEAN WORKSHOP ON SOLAR SYSTEM DYNAMICS AND EPHEMERIDES*, Dezember 2007.
- McCarthy, D. D. and G. Petit**, IERS Conventions (2003), *International Earth Rotation and Reference System Service (IERS), IERS Technical Note; NO. 32*, 2003.
- Mendes, V. B. and R. B. Langely**, A Comprehensive Analysis of Mapping Functions Used in Modeling Tropospheric Propagation Delay in Space Geodetic Data, in *International Symposium on Kinematic Systems in Geodesy, Geomatics and Navigation*, 1994.
- Mendes, V. B. and R. B. Langely**, Tropospheric Zenith Delay Prediction Accuracy for Airborne GPS High-Precision Positioning, in *Proceedings of The Institute of Navigation 54th Annual Meeting*, 337–347, Juni 1998.
- Milani, A., A. Nobili and P. Farinella**, *Non-gravitational perturbations and satellite geodesy*, IOP Publishing Ltd, Bristol, 1. Auflage, 1987.

- Montenbruck, O. and E. Gill**, *Satellite Orbits*, Springer, New York, Berlin, 2000.
- Morabito, D. D. and S. W. Asmar**, Radio-Science Performance Analysis Software, *TDA Progress Report, 42-120*, 1995.
- Morley, T.**, Optical properties of the Mars Express spacecraft, Personal Communication, 2004.
- Morley, T.**, Optical properties of the Rosetta spacecraft, Personal Communication, 2008.
- Moroz, L. V., T. Hiroi, T. V. Shingareva, A. T. Basilevsky, A. V. Fisenko, L. F. Semjonova and C. M. Pieters**, Reflectance Spectra of CM2 Chondrite Mighei Irradiated with Pulsed Laser and Implications for Low-Albedo Asteroids and Martian Moons, in *Lunar and Planetary Institute Science Conference Abstracts*, edited by S. Mackwell & E. Stansbery, vol 35 of *Lunar and Planetary Inst. Technical Report*, 1279, 2004.
- Müller, M. et al.**, The size and albedo of Rosetta fly-by target 21 Lutetia from new IRTF measurements and thermal modeling, *Astron. Astrophys.*, *447*, 1153–1158, 2006.
- Murchie, S.**, Mars pathfinder spectral measurements of Phobos and Deimos: Comparison with previous data, *J. Geophys. Res.*, *104*, 9069–9080, 1999.
- Murchie, S. and S. Erard**, Spectral Properties and Heterogeneity of PHOBOS from Measurements by PHOBOS 2, *Icarus*, *123*, 63–86, 1996.
- Murchie, S. and B. Zellner**, The HST Spectrum of Phobos: Comparison with Mariner 9, Viking, and PHOBOS 2 Results and with Meteorite Analogs, in *Lunar and Planetary Institute Conference Abstracts*, vol 25 of *Lunar and Planetary Institute Conference Abstracts*, 957, 1994.
- Murchie, S. L., T. Choo, D. Humm, A. S. Rivkin, J.-P. Bibring, Y. Langevin, B. Gondet, T. L. Roush, T. Duxbury and Crism Team**, MRO/CRISM Observations of Phobos and Deimos, in *Lunar and Planetary Institute Conference Abstracts*, vol 39 of *Lunar and Planetary Institute Conference Abstracts*, 1434, 2008.
- Murray, J. B., J. C. Iliffe, J.-P. A. L. Muller, G. Neukum, S. Werner and M. R. Balme**, New Evidence on the Origin of Phobos' Parallel Grooves from HRSC Mars Express, in *37th Annual Lunar and Planetary Science Conference*, edited by S. Mackwell and E. Stansbery, vol 37 of *Lunar and Planetary Inst. Technical Report*, 2195, 2006.
- NAIF**, The NASA Planetary Science Division's Ancillary Information System SPICE, <http://naif.jpl.nasa.gov/naif/>, 2009.
- Oberst, J., K. D. Matz, T. Roatsch, B. Giese, H. Hoffmann, T. Duxbury and G. Neukum**, Astrometric observations of Phobos and Deimos with the SRC on Mars Express, *A&A*, *447*, 1145–1151, 2006.

- Pang, K. D., J. B. Pollack, J. Veverka, A. L. Lane and J. M. Ajello**, The composition of PHOBOS - Evidence for carbonaceous chondrite surface from spectral analysis, *Science*, 199, 64–66, 1978.
- Parkinson, B. W. and H. J. Spilker**, *Global Positioning System: Theory and Applications*, vol I, American Institute of Aeronautics and Astronautics, 2. Auflage, 1996.
- Pätzold, M.**, Mars Express Orbiter Radio Science MaRS: Flight Operations Manual - Experiment User Manual, MEX-MRS-IGM-MA-3008, Issue 2, Revision 1, 2003.
- Pätzold, M.**, IFMS Doppler Processing Software: Level 1a to Level 2 Software Design Specifications, MEX-MRS-IGM-DS-3035, Issue 2, Revision 4, 2004.
- Pätzold, M.**, Rosetta Radio Science Investigations Experiment User Manual, RO-RSI-IGM-MA-3081, Issue 4, Revision draft, 2006.
- Pätzold, M. et al.**, Mass and density determinations of 140 Siwa and 4979 Otawara as expected from the Rosetta flybys, *Astron. Astrophys.*, 370, 1122–12227, 2001.
- Pätzold, M., F. M. Neubauer et al.**, MaRS: Mars Express Orbiter Radio Science, in *Mars Express, The Scientific Payload*, edited by A. W. E. P. Division, 141–164, ESA, ESA Publ. Division, 2004.
- Peale, S. J.**, The origin of the natural satellites, in *Planets and Moons*, edited by T. Spohn, vol 10 of *Treatise on Geophysics*, 471–473, Elsevier, Amsterdam, 2007.
- Pollack, J. B., J. Veverka, K. D. Pang, D. S. Colburn, A. L. Lane and J. M. Ajello**, Multicolor observations of phobos with the viking lander cameras - evidence for a carbonaceous chondritic composition, *Science*, 199, 66–69, 1978.
- Press, W. H., S. A. Teukolsky, W. T. Vetterling and B. P. Flannery**, *Numerical Recipes in Fortran*, Cambridge Univ. Press, Cambridge, 2. Auflage, 1986.
- Remus, S., B. Häusler, M. Pätzold and A. Wennmacher**, Ergebnisse der Radio Science Testmessungen an den ESA-Satelliten Rosetta und Mars Express, *DGLR Jahrestagung Hamburg*, 2001.
- Richardson, D. C. et al.**, Gravitational Aggregates: Evidence and Evolution, in *Asteroids III*, edited by W. F. Bottke JR. and others, 501–515, Univ. of Ariz. Press, 2002.
- Rivkin, A. S., R. H. Brown, D. E. Trilling, J. F. Bell and J. H. Plassmann**, Near-Infrared Spectrophotometry of Phobos and Deimos, *Icarus*, 156, 64–75, 2002.
- Rosenblatt, P., V. Lainey, S. Le Maistre, J. C. Marty, V. Dehant, M. Pätzold, T. van Hoolst and B. Häusler**, Accurate Mars Express orbits to improve the determination of the mass and ephemeris of the Martian moons, *Planetary and Space Science*, 56, 1043–1053, 2008.

- Saastamoinen, J.**, Atmospheric Correction for the Troposphere and Stratosphere in Radio Ranging Satellites, in *The Use of Artificial Satellites for Geodesy*, edited by S. W. Henriksen and others, 247–252, American Geophysical Union, Washington D. C., 1972.
- Schaer S.**, How to use CODE's Global Ionosphere Maps, <ftp://ftp.unibe.ch/aiub/ionosphere/doc/>, 1997.
- Schneider, M.**, *Satellitengeodäsie*, BI-Wissenschafts-Verlag, Mannheim, Wien, Zürich, 1988.
- Schwinger, J.**, Simulation von Umlaufbahnen um einen Kometenkern, Diplomarbeit am Institut für Geophysik und Meteorologie an der Universität zu Köln, 2001.
- Seidelmann, P. K. and T. Fukushima**, Why new time scales, *Astron. Astrophys.*, *265*, 833 – 838, 1992.
- Seidelmann, P. K. et al.**, Report of the IAU/IAG Working Group on Cartographic Coordinates and Rotational Elements of the Planets and Satellites:2000, *Cel. Mech. and Dynam. Astron.*, *82*, 83–110, 2001.
- Selle, J.**, Planung und Simulation von Radio-Science-Experimenten interplanetarer Raumfahrt-Missionen, Dissertation am Institut für Raumfahrttechnik an der Universität der Bundeswehr, München, 2005.
- Singer, S. F.**, Origin of the Martian Satellites Phobos and Deimos, in *Exploration of Phobos and Deimos*, 36, 2007.
- Smith, S. W.**, *The Scientist Engineer's Guide to Digital Signal Processing*, California Technical Pub, 1998.
- Smith, D. E., F. G. Lemoine and M. T. Zuber**, Simultaneous estimation of the masses of Mars, Phobos, and Deimos using spacecraft distant encounters, *Geophys. Res. Lett.*, *22*, 2171–2174, 1995.
- Soffel, M. H.**, *Relativity in Astrometry, Celestial Mechanics and Geodesy*, Springer-Verlag, Berlin, Heidelberg, 1989.
- Stiffel, A. K.**, Untersuchung verschiedener numerischer Filterverfahren zur Verbesserung des Signal- zu Rauschverhältnis bei Schwerefeldmessung von Mars Express, Studienarbeit II am Institut für Raumfahrttechnik an der Universität der Bundeswehr, München, 2008.
- Szeto, A. M. K.**, Orbital evolution and origin of the Martian satellites, *Icarus*, *55*, 133–168, 1983.
- Thomas, P.**, Gravity, Tides, and Topography on Small Satellites and Asteroids: Application to Surface Features of the Martian Satellites, *Icarus*, *105*, 326–344, 1993.
- Thomas, P. et al.**, Satellites of Mars: Geologic History, in *Mars*, edited by H. Kiefer et al., 1257–1282, Univ. of Ariz. Press, 1992.

- Tolson, R. H., W. T. Blackshear, M. L. Mason and G. M. Kelly**, The mass of PHOBOS, *Geophys. Res. Lett.*, *4*, 551–554, 1977.
- Tolson, R. H., T. C. Duxbury, G. H. Born, E. J. Christensen, R. E. Diehl, D. Farless, C. E. Hildebrand, R. T. Mitchell, P. M. Molko, L. A. Morabito, F. D. Palluconi, R. J. Reichert, H. Taraji, J. Veverka, G. Neugebauer and J. T. Findlay**, Viking first encounter of PHOBOS - Preliminary results, *Science*, *199*, 61–64, 1978.
- Vallado, D. A.**, *Fundamentals of Astrodynamics and Applications*, Space Technology Library, Dordrecht, Boston, London, 2001.
- Veverka, J. and J. A. Burns**, The moons of Mars, *Annual Review of Earth and Planetary Sciences*, *8*, 527–558, 1980.
- Wieczorek, M. A. and M. T. Zuber**, Thickness of the Martian crust: Improved constraints from geoid-to-topography ratios, *Journal of Geophysical Research (Planets)*, *109*, 1009, 2004.
- Williams, B. G., T. C. Duxbury and C. E. Hildebrand**, Improved Determination of PHOBOS and Deimos Masses from Viking Fly-Bys, in *Lunar and Planetary Institute Conference Abstracts*, vol 19 of *Lunar and Planetary Inst. Technical Report*, 1274, 1988.
- Willner, K., J. Oberst, M. Wählisch, K.-D. Matz, H. Hoffmann, T. Roatsch, R. Jaumann and V. Mertens**, New astrometric observations of Phobos with the SRC on Mars Express, *A&A*, *488*, 361–364, 2008.
- Willner, K., J. Oberst, H. Hussmann, B. Giese, H. Hoffmann, K. Matz, T. Roatsch and T. Duxbury**, Phobos control point network, rotation, and shape, *Earth and Planetary Science Letters*, 2009.
- Yuan, D.-N., W. L. Sjogren, A. S. Konopliv and A. B. Kucinskis**, Gravity field of Mars: A 75th Degree and Order Model, *J. Geophys. Res.*, *106*, 23377–23402, 2001.
- Yuen, J. H.**, *Deep Space Telecommunications System Engineering*, Plenum Press, New York and London, 1983.
- Zellner, B. and E. N. Wells**, Spectrophotometry of Martian Satellites with the Hubble Space Telescope, in *Lunar and Planetary Institute Conference Abstracts*, vol 25 of *Lunar and Planetary Institute Conference Abstracts*, 1541, 1994.

---

# Erklärung

---

Ich versichere, dass ich die von mir vorgelegte Dissertation selbständig angefertigt, die benutzten Quellen und Hilfsmittel vollständig angegeben und die Stellen der Arbeit - einschließlich Tabellen, Karten und Abbildungen -, die anderen Werken im Wortlaut oder dem Sinn nach entnommen sind, in jedem Einzelfall als Entlehnung kenntlich gemacht habe; dass diese Dissertation noch keiner anderen Fakultät oder Universität zur Prüfung vorgelegen hat; dass sie - abgesehen von unten angegebenen Teilpublikationen - noch nicht veröffentlicht worden ist sowie, dass ich eine solche Veröffentlichung vor Abschluss des Promotionsverfahrens nicht vornehmen werde. Die Bestimmungen der Promotionsordnung sind mir bekannt. Die von mir vorgelegte Dissertation ist von Priv. Doz. Dr. Martin Pätzold betreut worden.

München, den 15.03.2010

.....

T. Andert

---

# Acknowledgements

---

The successful completion of this work would not have been possible without the advice and support of many institutions and single persons.

The support and commitment of my supervisors Priv. Doz. Dr. Martin Pätzold and Prof. Dr. Bernd Häusler is gratefully acknowledged.

Special thanks are devoted to the entire Radio Science team of Mars Express, Venus Express and Rosetta for the fruitful discussions at our team meetings.

I kindly thank Prof. Dr. Andreas Eckart and Prof. Dr. Joachim Saur for joining the doctoral committee.

I extend many thanks to Dr. Jörg Schwinger and Dr. Thomas Epping for the essential meliorations of this manuscript by their proof-reading.

The invaluable help of my colleagues at the Department for Geophysics and Meteorology at the University of Cologne, the Department of Space Technology at the University of the German Armed Forces in Munich and the Division of Planetary Science at the RIU in Cologne is highly appreciated.

Finally, I sincerely thank my wife Şerife for her great support and her patience, my son Johan for letting the Sun always shine and my parents for their neverending support.

The Mars Express Radio Science Experiment MaRS and the Rosetta Radio Science Investigations Experiment RSI is funded by DLR Bonn under grants 50QP9909 and 50QM0701.